

DETERMINATION OF THE POLARIZATION OBSERVABLES C_x , C_z , AND P_y FOR
FINAL-STATE INTERACTIONS IN THE REACTION $\vec{\gamma}d \rightarrow K^+ \vec{\Lambda}n$

by

Tongtong Cao

Bachelor of Science
University of Science and Technology of China 2006
Master of Science
University of Science and Technology of China 2010

Submitted in Partial Fulfillment of the Requirements
for the Degree of Doctor of Philosophy in
Physics
College of Arts and Sciences
University of South Carolina
2016

Accepted by:

Yordanka Ilieva, Major Professor
Fanglin Chen, Committee Member
Ralf Gothe, Committee Member
Matthias Schindler, Committee Member
Lacy Ford, Vice Provost and Dean of Graduate Studies

© Copyright by Tongtong Cao, 2016
All Rights Reserved.

DEDICATION

To this Universe

ACKNOWLEDGMENTS

On the completion of my thesis, I would like to express my deepest gratitude to all those whose kindness and advice have made this work possible ¹.

The biggest thank goes to my thesis advisor, Yordanka Ilieva, who gave me valuable and patient instructions on my journey of getting a Ph.D. Her effective advice and shrewd comments have kept my thesis in the right direction. The door to her office was always open whenever I ran into trouble or had a question about my research or my life. This work would not have been possible without her contribution.

I would like to thank you all my group mates in the University of South Carolina. I will forever remember our weekly group meetings, in which every process of the procedure of my thesis study was discussed in time, and I learned a lot from your constructive suggestions. Many times, when I fell into struggles on my research, Dr. Steffen Strauch always shared good ideas and opened new windows for me. Dr. Nicholas Zachariou provided me endless assistance on data analysis. He was always there for me and his help and friendship were invaluable. Hao Jiang and I entered USC at the same time, and helped each other in our research ways. Colin Gleason and Aneta Netz offered me a lot of aid to improve my English language. Also thank you, the rest of my group members, Lin Li and Nicolas Recalde.

I would like to thank my collaborators in Hall B of JLab, Pawel Nadel-Turonski, Phil Cole, Edwin Munevar, Daria Sokhan, Paul Mattione, Charles Taylor, Derek Glazier, Olga Cortes and Nick Compton, for their support, guidance and advice. Many thanks go to my committee members, Dr. Ralf Gothe, Dr. Matthias Schindler,

¹Thanks to the U.S. NSF for funding this work under grant PHY-125782.

and Dr. Fanglin Chen, for encouraging words, thoughtful criticism, and time they dedicated to better my work. I also want to thank the teachers I had at USC, Dr. Richard J. Creswick, Dr. Milind Purohit, Dr. Yaroslav Bazaliy, Dr. Pawel O. Mazur, and Dr. Vladimir Gudkov, who put bricks down and lighted up the road.

Most importantly I would like to thank my parents and parents in-law for their incredible support and encouragement and for all they have done to make my life happier. My deepest gratitude goes to my dear wife, who contributes all of her efforts to maintain our family, and stands by my side to help me overcome any obstacles that come my way. Finally, I would like to thank my daughters, who are the best gifts from God, for bringing endless power to my life.

ABSTRACT

The hyperon-nucleon (YN) interaction plays a key role in hypernuclei and strange nuclear matter and is an important part of the baryon-baryon interaction. While considerable progress has been made in the understanding of the nucleon-nucleon (NN) interaction, the YN interaction is less known. Some parameters of the YN potential can be obtained from the NN potential by using SU(3) symmetry. However, due to broken SU(3) there are parameters, which must be obtained from fits to experimental data. High-statistics data on exclusive Λ photoproduction off the deuteron initiated with highly-polarized photons offer a unique opportunity to extract a large sample of polarization observables for final-state interaction events, which can be used to constrain hyperon-nucleon potentials. In this work, we determine the polarization transfers to the Λ , C_x and C_z , from circularly polarized photons, and the hyperon recoil polarization, P_y , for final-state interactions (FSI) in the reaction $\vec{\gamma}d \rightarrow K^+ \vec{\Lambda} n$ using data taken with the CLAS detector at the Jefferson laboratory in the E06-103 experiment. Meanwhile, C_x , C_z , and P_y for $K^+\Lambda$ photoproduction off the bound proton were extracted for systematic studies and compared to published CLAS results from $K^+\Lambda$ photoproduction off a free proton. Our results cover photon energies from 0.9 GeV to 2.6 GeV, a kaon momentum range up to 2 GeV/ c , a kaon polar-angle range in laboratory system from 14° to 70° , a Λ polar-angle range (relative to the three-momentum transfer to the Λn system) from 0° to 60° , and a Λn invariant-mass range from 2 GeV/ c^2 to 2.5 GeV/ c^2 . The FSI results are the first ever obtained for C_x , C_z , and P_y and will be used to constrain the theoretical free parameters of the models of the YN potential.

TABLE OF CONTENTS

DEDICATION	iii
ACKNOWLEDGMENTS	iv
ABSTRACT	vi
LIST OF TABLES	x
LIST OF FIGURES	xi
CHAPTER 1 INTRODUCTION	1
1.1 The Strong Interaction	1
1.2 Historical Overview	2
1.3 Hyperon-nucleon Potential	7
1.4 The reaction $\vec{\gamma}d \rightarrow K^+ \vec{\Lambda}n$	12
CHAPTER 2 EXPERIMENTAL FACILITY	23
2.1 The Continuous Electron Beam Accelerator Facility	23
2.2 Hall B and the CLAS Detector	25
2.3 The E06-103 Experiment	32
CHAPTER 3 HELICITY AND POLARIZATION OF THE PHOTON BEAM	37
3.1 Photon-Beam Helicity	37
3.2 Electron Beam Polarization	38

3.3	Photon Beam Polarization	39
CHAPTER 4 DATA ANALYSIS		42
4.1	Particle Identification (PID)	42
4.2	Photon Selection	45
4.3	Additional Selection Cuts	50
4.4	Background Subtraction	54
CHAPTER 5 DETERMINATION OF C_x , C_z , AND P_y		63
5.1	Observable-Extraction Methods	63
5.2	Statistical Uncertainties of C_x , C_z , and P_y	73
5.3	Determination of C_x , C_z , and P_y for the Quasi-Free Mechanism	79
5.4	Determination of C_x , C_z , and P_y for Final-State Interactions	89
CHAPTER 6 SYSTEMATIC UNCERTAINTIES		103
6.1	Acceptance	104
6.2	Fiducial Cuts	105
6.3	Particle Identification	107
6.4	Vertex Cut	108
6.5	Photon Selection	108
6.6	Invariant Mass Cut	110
6.7	Missing Momentum Cut	110
6.8	Missing Mass Cut	111
6.9	Summary of Systematic Uncertainties	112

CHAPTER 7	DISCUSSION	113
7.1	Comparison to Published Results	113
7.2	Comparison between FSI and QF observables	115
7.3	Dependence of QF Observables on Missing Momentum	116
7.4	Comparison of FSI Observables to Theoretical Calculations	118
7.5	Physics Studies of the Reaction $\vec{\gamma}d \rightarrow K^+\vec{\Lambda}n$	119
CHAPTER 8	SUMMARY	127
BIBLIOGRAPHY	130

LIST OF TABLES

Table 1.1	Properties of light quarks.	7
Table 1.2	Free Parameters in NSC89 and the NSC97(a-f) models.	10
Table 1.3	Free parameters of the YN contact terms for various cut-off masses.	11
Table 1.4	Values of the isospin-singlet and isospin-triplet Λn scattering lengths.	20
Table 1.5	Published results of C_x , C_z , and P_y from different experiments.	20
Table 2.1	A list of the data acquired in the g13a experiment.	33
Table 3.1	Electron-beam polarization values obtained by averaging the set of Møller measurements taken throughout g13a.	40
Table 4.1	Reaction channels implemented in our realistic event generator.	56
Table 5.1	Means and standard deviations of the means of distributions over the differences between C_x and C_z values extracted by the different fitting methods and the true values of C_x and C_z	72
Table 6.1	Summary of the systematic uncertainties for C_x , C_z , and P_y	112

LIST OF FIGURES

Figure 1.1	Running coupling constant of the strong interaction.	3
Figure 1.2	The first strange particles.	4
Figure 1.3	Discovery of K^+	5
Figure 1.4	The baryon octet and the meson octet.	6
Figure 1.5	One-boson-exchange diagrams for the YN potentials within the Nijmegen soft-core model.	9
Figure 1.6	One-pseudoscalar-meson-exchange diagrams for the hyperon-nucleon interaction in chiral EFT.	11
Figure 1.7	Lowest order contact terms for the hyperon-nucleon interaction in chiral EFT.	11
Figure 1.8	The four main mechanisms contributing to the reaction $\vec{\gamma}d \rightarrow K^+ \vec{\Lambda}n$	14
Figure 1.9	Axis convention for FSI Observables.	17
Figure 1.10	Unpolarized differential cross section and polarization observables for $\vec{\gamma}d \rightarrow K^+ \vec{\Lambda}n$ as a function of the hyperon polar angle θ'_Λ	18
Figure 1.11	Differential cross section as a function of $IM_{p\Lambda}$ for the reaction $pp \rightarrow K^+ \Lambda p$	19
Figure 1.12	P_y vs. W in bins of $\cos \theta_K^{c.m.}$ for different experiments.	21
Figure 1.13	C_x vs. W in bins of $\cos \theta_K^{c.m.}$ from the g1c experiment.	22
Figure 1.14	C_z vs. W in bins of $\cos \theta_K^{c.m.}$ from the g1c experiment.	22
Figure 2.1	CEBAF at the Thomas Jefferson Accelerator Facility (JLab).	24

Figure 2.2	Schematic diagram of the Hall-B beam line during real photo-production experiments.	26
Figure 2.3	Schematic diagram of the Hall-B tagging system.	27
Figure 2.4	Schematic diagram of the CLAS.	28
Figure 2.5	Geometry of the magnetic field produced by CLAS torus.	29
Figure 2.6	A 3-dimensional picture of the start counter.	30
Figure 2.7	Schematic diagram of a set of 56 scintillator paddles that comprise one sector of the time-of-light system.	32
Figure 2.8	Schematic diagram of a sector of the forward electromagnetic calorimeter.	33
Figure 2.9	Schematic diagram of the 40-cm long LD ₂ target cell used in the g13 experiment.	34
Figure 2.10	Timeline of the $K^+\Lambda n$ photon-flux-normalized yield.	36
Figure 2.11	Distributions of normalized $K^+\Lambda n$ yields.	36
Figure 3.1	Timeline of the slope of a linear fit to the distribution of helicity asymmetry vs $\cos\theta_z$	38
Figure 3.2	Helicity asymmetry vs. $\cos\theta_z$ for a bad-quality run.	39
Figure 3.3	Electron-beam polarization measurements taken during the 1.987-GeV and 2.649-GeV run periods in 2006 of the g13a experiment.	40
Figure 3.4	Ratio of P_γ to P_e as a function of ratio of E_γ to E_e	41
Figure 4.1	$\Delta\beta$ as a function of momentum for proton candidates.	43
Figure 4.2	$\Delta\beta$ as a function of momentum for K^+ candidates.	44
Figure 4.3	$\Delta\beta$ as a function of momentum for π^- candidates.	44
Figure 4.4	Schematic diagram visualizing the DOCA method to determine the vertex position.	46

Figure 4.5	Event distribution over the z -component of vertex distribution. . .	46
Figure 4.6	Vertex time difference distribution after PID and a narrow IM cut.	48
Figure 4.7	Fractions of events with different number of photons within our ± 1 -ns coincidence window (after PID, a narrow IM cut, and the Δt cut).	49
Figure 4.8	Missing-mass distributions of events with two photons yielding $ \Delta t < 1$ ns.	49
Figure 4.9	Invariant-mass distribution after PID, photon selection, and E_γ cuts.	52
Figure 4.10	Missing-momentum distribution after PID, photon selection, E_γ cut, invariant-mass cut.	53
Figure 4.11	E_γ vs. MM after PID, photon selection, E_γ cut, and IM cuts. . .	55
Figure 4.12	Flow chart of the comprehensive event generator used in the simulation of physics backgrounds to the reaction $\vec{\gamma}d \rightarrow K^+ \vec{\Lambda} n$.	57
Figure 4.13	An example of momentum correction function (red curve) for the simulated data.	59
Figure 4.14	Missing-mass distributions of accidental quasi-free (left) and final-state interaction (right) events.	60
Figure 4.15	An example of MM fitting for one kinematic bin.	61
Figure 4.16	Distribution over χ^2 per degree of freedom of the fits to MM histograms.	62
Figure 5.1	Information about the number of background events obtained from MM fitting is used to determine the weight w^i for the i^{th} event in a given kinematic bin.	65
Figure 5.2	Examples of distributions of $Asym$ vs. $\cos \theta_x$ (left column) and $\cos \theta_z$ (right column) from the results for quasi-free events in $\vec{\gamma}d \rightarrow K^+ \vec{\Lambda} n$	66
Figure 5.3	Differences between the extracted and true values.	72

Figure 5.4	Means of differences between 6000 extracted values and true values with and without consideration of the CLAS acceptance for C_x , C_z , and P_y	73
Figure 5.5	12 difference distributions between the values extracted by the maximum likelihood method and the true values for C_x	76
Figure 5.6	12 difference distributions between the values extracted by the maximum likelihood method and the true values for C_z	77
Figure 5.7	12 difference distributions between the values extracted by the maximum likelihood method and the true values for P_y	78
Figure 5.8	Dependence of the statistical uncertainty.	79
Figure 5.9	Relative differences between the estimated uncertainties and the standard uncertainties for C_x , C_z , and P_y , separately.	80
Figure 5.10	Definition of coordinate system for the determination of the observables C_x , C_z , and P_y for quasi-free $K^+\Lambda$ photoproduction off the bound proton.	81
Figure 5.11	Choice of kinematic binning for the extraction of C_x , C_z , and P_y for the quasi-free mechanism of the reaction $\vec{\gamma}d \rightarrow K^+\vec{\Lambda}n$	82
Figure 5.12	Choice of kinematic binning for the extraction of C_x , C_z , and P_y for the quasi-free mechanism of the reaction $\vec{\gamma}d \rightarrow K^+\vec{\Lambda}n$	83
Figure 5.13	C_x as a function of $\cos\theta_{KCM}$ at fixed E_γ for the quasi-free mechanism of the reaction $\vec{\gamma}d \rightarrow K^+\vec{\Lambda}n$	84
Figure 5.14	C_z as a function of $\cos\theta_{KCM}$ at fixed E_γ for the quasi-free mechanism of the reaction $\vec{\gamma}d \rightarrow K^+\vec{\Lambda}n$	85
Figure 5.15	P_y as a function of $\cos\theta_{KCM}$ in fixed E_γ for QF of $\vec{\gamma}d \rightarrow K^+\vec{\Lambda}n$	86
Figure 5.16	C_x as a function of E_γ at fixed $\cos\theta_{KCM}$ for the quasi-free mechanism of the reaction $\vec{\gamma}d \rightarrow K^+\vec{\Lambda}n$	88
Figure 5.17	C_z as a function of E_γ at fixed $\cos\theta_{KCM}$ for the quasi-free mechanism of the reaction $\vec{\gamma}d \rightarrow K^+\vec{\Lambda}n$	89

Figure 5.18	P_y as a function of E_γ at fixed $\cos\theta_{KCM}$ for the quasi-free mechanism of the reaction $\vec{\gamma}d \rightarrow K^+\vec{\Lambda}n$	90
Figure 5.19	R as a function of $\cos\theta_{KCM}$ at fixed E_γ for the quasi-free mechanism of the reaction $\vec{\gamma}d \rightarrow K^+\vec{\Lambda}n$	91
Figure 5.20	R as a function of E_γ at fixed $\cos\theta_{KCM}$ for the quasi-free mechanism of the reaction $\vec{\gamma}d \rightarrow K^+\vec{\Lambda}n$	92
Figure 5.21	Axis convention used in the extraction of polarization observables for final-state interactions in the reaction $\vec{\gamma}d \rightarrow K^+\vec{\Lambda}n$. . .	93
Figure 5.22	Event distributions and binning over E_γ (top left), θ'_Λ (top right), p_K (middle left), θ_K (middle right), and $IM_{\Lambda n}$ (bottom left) for the extraction of one-fold differential estimates of C_x , C_z , and P_y	95
Figure 5.23	C_x , C_z , and P_y as a function of E_γ , θ'_Λ , p_K , θ_K , and $IM_{\Lambda n}$ for FSI of the reaction $\vec{\gamma}d \rightarrow K^+\vec{\Lambda}n$	96
Figure 5.24	$IM_{\Lambda n}$ vs. MM for final-state interactions of the reaction $\vec{\gamma}d \rightarrow K^+\vec{\Lambda}n$	97
Figure 5.25	C_x , C_z , and P_y as a function of $IM_{\Lambda n}$ for final-state interactions of the reaction $\vec{\gamma}d \rightarrow K^+\vec{\Lambda}n$	97
Figure 5.26	Setup of kinematic bins in E_γ and θ'_Λ for the FSI data.	98
Figure 5.27	C_x , C_z , and P_y as a function of θ'_Λ for fixed E_γ	98
Figure 5.28	Setup of kinematic bins in p_K and θ'_Λ for the FSI data.	99
Figure 5.29	C_x , C_z , and P_y as a function of θ'_Λ for fixed p_K	99
Figure 5.30	Setup of kinematic bins in θ_K and θ'_Λ for the FSI data.	100
Figure 5.31	C_x , C_z , and P_y as a function of θ'_Λ for fixed θ_K	100
Figure 5.32	Setup of kinematic bins in $IM_{\Lambda n}$ and θ'_Λ for the FSI data.	101
Figure 5.33	C_x , C_z , and P_y as a function of θ'_Λ for fixed $IM_{\Lambda n}$	102

Figure 6.1	Distributions of relative difference $(Obs_{ext} - Obs_{true})/Obs_{true}$ for C_x , C_z , and P_y	105
Figure 6.2	Fiducial cuts for protons with momenta between 0.4 GeV/c and 0.8 GeV/c.	106
Figure 6.3	Distributions of the relative differences of observables estimated without (nominal values) and with applied fiducial cuts.	106
Figure 6.4	$\Delta\beta$ as a function of momentum with 3σ and 2σ cuts for proton PID.	107
Figure 6.5	Distributions of the relative differences of observables estimated with a broader PID selection cut (nominal values) and with a narrower PID selection cut.	108
Figure 6.6	Distributions of the relative differences of observables estimated with a broader vertex cut (nominal values) and with a narrower vertex cut.	109
Figure 6.7	Distributions of the relative differences of observables estimated with a broader photon selection cut (nominal values) and with a narrower photon selection cut.	109
Figure 6.8	Distributions of the relative differences of observables estimated with a broader IM selection cut (nominal values) and with a narrower IM selection cut.	110
Figure 6.9	Distributions of the relative differences of observables estimated with a broader MP selection cut (nominal values) and with a narrower MP selection cut.	111
Figure 6.10	Distributions of the relative differences of observables estimated with a broader MM selection cut (nominal values) and with a narrower MM selection cut.	112
Figure 7.1	Comparison of C_x between the g1c and g13 experiments.	114
Figure 7.2	Comparison of C_z between the g1c and g13 experiments.	114
Figure 7.3	Comparison of P_y between the g1c and g13 experiments.	115
Figure 7.4	C_x comparison between FSI and QF for one-fold differential estimates.	116

Figure 7.5	C_z comparison between FSI and QF for one-fold differential estimates.	117
Figure 7.6	P_y comparison between FSI and QF for one-fold differential estimates.	118
Figure 7.7	Comparison of C_x , C_z , and P_y for various missing momentum cut ranges.	119
Figure 7.8	Difference of C_x , C_z , and P_y between different missing momentum cut ranges.	119
Figure 7.9	Comparison to the Miyagawa's model.	120
Figure 7.10	Comparison of C_x , C_z , and P_y between clean and quasi-clean channels.	122
Figure 7.11	C_x comparison between FSI and QF for simulated data.	124
Figure 7.12	C_z comparison between FSI and QF for simulated data.	125
Figure 7.13	P_y comparison between FSI and QF for simulated data.	126

CHAPTER 1

INTRODUCTION

1.1 THE STRONG INTERACTION

The strong interaction, which is the mechanism responsible for the strong force between quarks and gluons, is one of the four fundamental interactions of nature and is a part of the Standard Model of particle physics. Six different types of quarks are the fundamental constituents of strongly interacting elementary particles called hadrons, while eight independent types of gluons mediate the strong interaction between quarks, antiquarks, and other gluons. Hadrons are classified as baryons (consisting of three quarks) and mesons (consisting of quark-antiquark pairs). In this work, particles of interest are nucleons and hyperons, which are composed of three light quarks (which give baryons their quantum numbers), plus a variable number of sea quark-antiquark pairs of any flavor, plus any number of gluons. Nucleons (proton and neutron), are composed of up and down quarks, while hyperons contain at least one strange quark.

Quantum Chromodynamics (QCD) is the generally accepted and the most successful theory of the strong interaction. QCD is a quantum-field theory, as is the theory of the electromagnetic interaction, Quantum Electrodynamics (QED). The QCD analog of the electric charge is the color charge (a quark's color can take one of three charges, red, green or blue), and gluons are the force carriers of QCD, like photons are for QED. The magnitude of the coupling in QCD is given by the running coupling constant, α_s , which depends on the separation distance between the inter-

acting particles, *i.e.* the squared four-momentum transfer (Q^2) of the interaction (see Fig. 1.1). At the relatively large distances that are characteristic of nuclear physics, α_s is large, while at very short distances (less than a tenth of the size of a proton) it becomes quite small [1]. The scale dependence of the strong coupling is limited by two fundamental properties of QCD, namely color confinement and asymptotic freedom. Color confinement means that color-charged particles (quarks and gluons) cannot be isolated, and therefore cannot be directly observed as the quark-quark interaction is extremely strong at large distances (*i.e.* small Q^2). Asymptotic freedom [2] means that quarks and gluons interact very weakly at short distances (*i.e.* at large Q^2). Thus, the study of QCD splits naturally into the high-energy, very-short-distance regime, where perturbative QCD is applicable and the low-energy regime of quark confinement in the bound states, the hadrons [3].

Although the fundamental degrees of freedom of QCD are quarks and gluons, and nucleons and hyperons are bound states of quarks and gluons, many low-energy phenomena, where nucleons and/or hyperons do not get excited, can be described in terms of NN, NY, or YY interactions considering the baryons to be elementary particles. If nucleons and/or hyperons are non-relativistic, their interactions are described by potentials. In the procedure to formulate the potentials, free parameters are introduced, which need to be obtained from fits to experimental data. In this work, we determine experimental scattering polarization observables that are to be used in fits by YN potentials to constrain the potential parameters.

1.2 HISTORICAL OVERVIEW

Discovery of Strange Particles

Willis Eugene Lamb began his Nobel Prize acceptance speech in 1955 with the words “When the Nobel Prizes were first awarded in 1901, physicists knew something of just

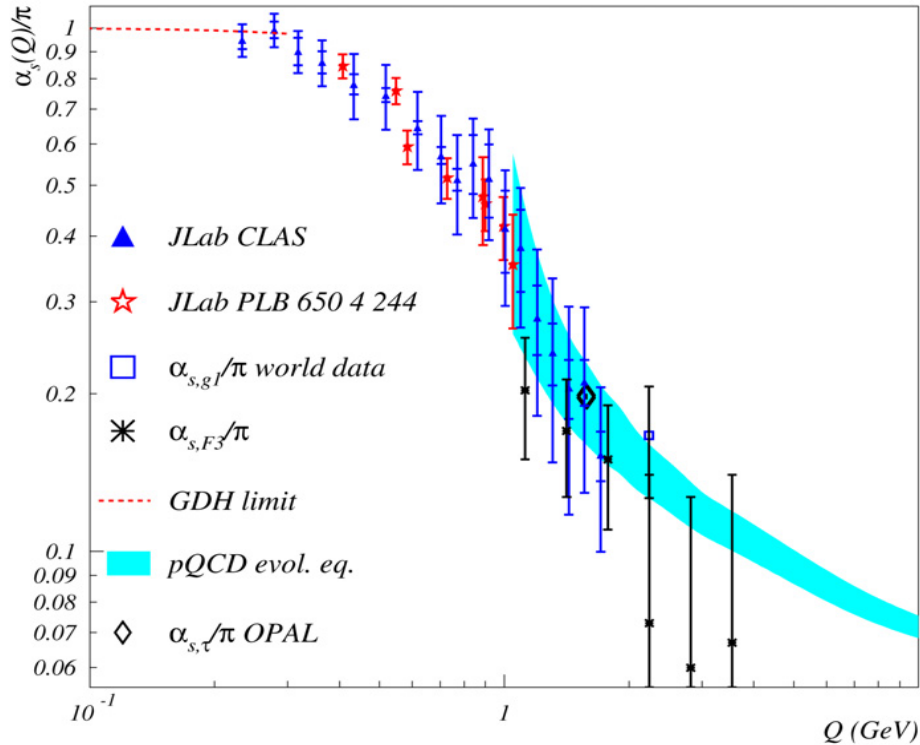


Figure 1.1: Running coupling constant of the strong interaction. $\alpha_s(Q)/\pi$ is obtained from JLab (triangles and open stars) and world (open squares) data on the Bjorken sum, OPAL data, the Gross-Llewellyn Smith sum results from the CCFR collaboration (stars), and the Bjorken (band) and Gerasimov-Drell-Hearn (dashed lines) sum rules. The figure is from [4].

two objects which are now called ‘elementary particles’: the electron and the proton. A deluge of other ‘elementary particles’ appeared after 1930; neutron, neutrino, μ meson, π meson, heavier mesons, and various hyperons.”

In a short period of the year 1947, physicists believed that they had solved the major problems of elementary particle physics: What particle mediates the strong interaction? Does a positively charged twin for the electron predicted by Dirac’s theory exist? What particle is emitted along with the electron in beta decay? Yukawa’s meson (the π) and Dirac’s positron had been finally found as well as Pauli’s neutrino. At that time, the muon was regarded as a meson instead of a lepton, and its role was not clearly understood in the whole scheme of things [1].

However, new problems came out very soon. A large number of heavier mesons and baryons were discovered. In December of 1947, Rochester and Butler published a cloud chamber photograph (see Fig. 1.2) showing the charged decay of a new electrically neutral particle, the K^0 :

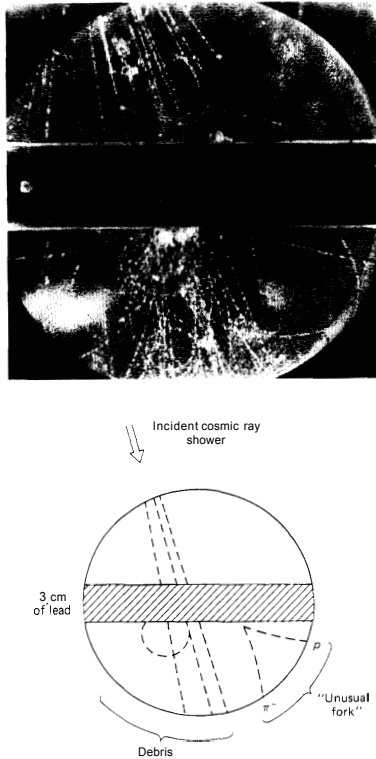
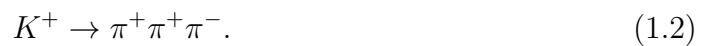


Figure 1.2: The first strange particles. Cosmic rays strike a lead plate, producing a K^0 , which subsequently decays into π^+ and π^- . The figure is from [1].



In 1949, Powell published a photograph (see Fig. 1.3) showing the charged decay of another new particle, the K^+ :



Subsequently, many more heavy mesons were discovered, including η , ϕ , ω , ρ , and so on.

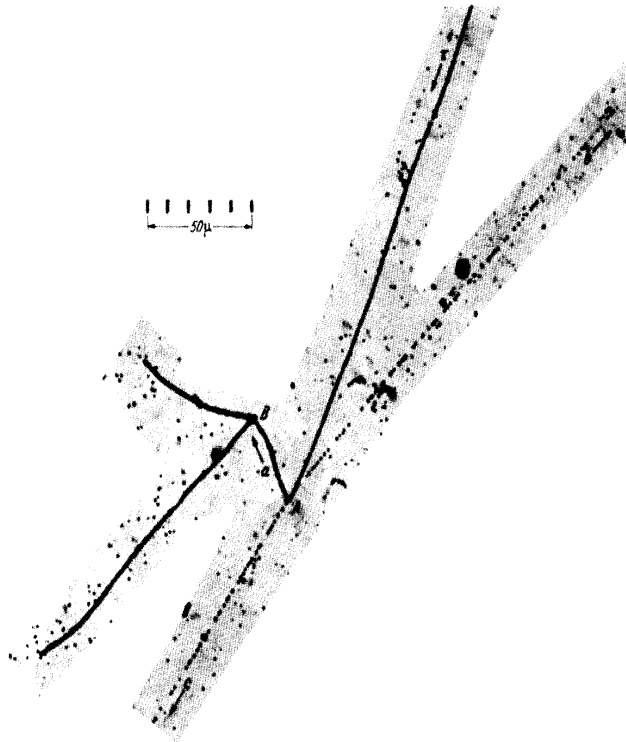


Figure 1.3: Discovery of K^+ . K^+ decays to double π^+ and π^- . The figure is from [1].

Meanwhile, the first strange baryon, the Lambda (Λ), was discovered by Anderson's group at CalTech in 1950. Over the next few years, many more heavy baryons were discovered, including Σs , Ξs , and so on.

These new particles were known collectively as “strange” particles. In 1952, the Brookhaven Cosmotron (the first of the modern particle accelerators) began operating, and soon it could produce strange particles in the laboratory. In the experiments, the behavior of these particles seemed “strange”. They were produced (about 10^{-23} s) much faster than they decayed (typically about 10^{-10} s). Nowadays, we know that the strange particles are produced by the strong interaction, and decay by the weak interaction. In 1953, a new property called “strangeness” was introduced for these strange particles by M. Gell-Mann and K. Nishijima. They postulated that the strangeness was conserved by the strong interaction, but not conserved by the weak

interaction [1].

The Eightfold Way

The Eightfold Way was introduced by Murray Gell-Mann in 1961 [5]. In this scheme, the baryons and the mesons are arranged into geometrical patterns according to their charge and strangeness. The eight lightest baryons and the eight lightest mesons are filled into two hexagonal arrays, separately. Figure 1.4 shows the baryon octet and the meson octet. The Eightfold Way not only organized discovered particles into proper pattern schemes (called multiplets), but also predicted new particles. These predicted particles were discovered successfully over the next ten years.

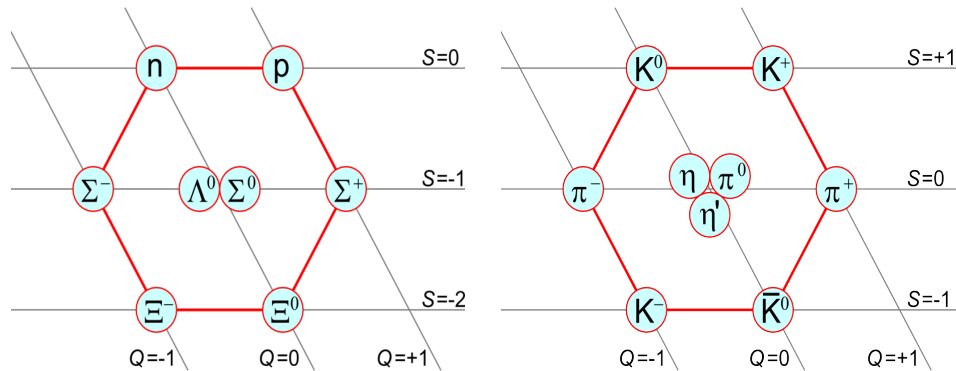


Figure 1.4: The baryon octet (left) and the meson octet (right). Particles with the same charge lie along the downward-sloping diagonal lines, while particles with the same strangeness lie along horizontal lines.

The Quark Model

The success of the Eightfold Way raised an important question: Why do the hadrons fit into these curious patterns? In 1964, Gell-Mann and Zweig independently proposed that all hadrons were composed of even more elementary constituents called quarks [1]. They suggested that every baryon was comprised of three quarks, and every meson was comprised of a quark and an antiquark. Nowadays, we know there

Table 1.1: Light-quark properties. J denotes total angular momentum, B denotes baryon number, Q denotes electronic charge, I_3 denotes the third component of isospin, and S denotes strangeness.

Name	Symbol	Mass (MeV/ c^2)	J	B	Q (e)	I_3	S
Up	u	$2.3 \pm 0.7 \pm 0.5$	$\frac{1}{2}$	$+\frac{1}{3}$	$+\frac{2}{3}$	$+\frac{1}{2}$	0
Down	d	$4.8 \pm 0.5 \pm 0.3$	$\frac{1}{2}$	$+\frac{1}{3}$	$-\frac{1}{3}$	$-\frac{1}{2}$	0
Strange	s	95 ± 5	$\frac{1}{2}$	$+\frac{1}{3}$	$-\frac{1}{3}$	0	-1

are six quark flavors rather than three. The three quarks in the Gell-Mann and Zweig quark model are the lightest quarks, the up, down, and strange quarks. Table 1.1 summarizes the key properties of the light quarks, which can explain the hadron multiplets (see Fig. 1.4). For instance, the quark-antiquark combinations yield nine mesons in the meson octet. In fact, the meson octet only included eight mesons when Gell-Mann introduced the Eightfold way, and the ninth particle with $Q = 0$ and $S = 0$, η' , was predicted by the quark model and then found experimentally.

1.3 HYPERON-NUCLEON POTENTIAL

The hyperon-nucleon (YN) interaction is the interaction between hyperons and nucleons. It obeys conservations of energy, momentum, angular momentum, charge, baryon number, lepton number, strangeness, isospin, parity, and charge conjugation. In the history, the SU(2) symmetry of isospin was successful to describe the nucleon-nucleon (NN) interaction. After the Eightfold Way was introduced by Gell-Mann, the flavor SU(3) symmetry, as the parent group of SU(2), was extended to describe the YN interaction. However, SU(3) is a broken symmetry, since mass splittings within the baryon octet are as large as 40%. In the Standard Model, the mass splittings originate with the quark masses [1]. The current masses of the up and the down quarks are very small, about 10 times the mass of the electron, while their effective masses are about $350 \text{ MeV}/c^2$ within the confines of a hadron. However, the current

mass of the strange quark is about $95 \text{ MeV}/c^2$, while its effective mass is about $500 \text{ MeV}/c^2$. The strong interaction treats all flavors equally except for the difference in quark masses.

In modern physics, the understanding of the YN interaction plays a key role in building a comprehensive picture of the strong interaction. It is known as the basic force that binds Λ and Σ hyperons in hypernuclei. It is crucial to understand the properties of neutron stars since reliable YN and hyperon-hyperon (YY) potentials are needed for realistic calculations of the hypernuclear structure and the hyperon matter. Even in a conventional nuclear system, it is important if one introduces the strangeness degrees of freedom in the nucleon-nucleon (NN) interaction to extend the baryon-baryon interaction to a more unified picture demanded by SU(3) symmetry [6].

In the course of understanding the baryon-baryon interaction, the first attempt was to describe the NN interaction, and then to extend NN potentials to YN potentials. To construct a YN potential, one cannot allow too many free parameters, 5 or 6 at most, if one wants to determine them reliably. Considerable theoretical and experimental input is therefore needed to construct a YN model. The strategy is to start with a NN model, and then apply SU(3) flavor symmetry to this model in order to obtain a YN model. Traditionally, meson-exchange models [7, 8, 9, 10, 11, 12] have been applied to describe the YN interaction. Recently, chiral Effective Field Theory (χ EFT) [13] and lattice QCD [14] have been used to derive the YN interaction.

The Nijmegen soft-core one-boson-exchange (OBE) model (NSC), which is derived from Regge-pole theory [15], is widely adopted and developed by a large number of theoretical groups. The NSC89 [10] and NSC97 [11] YN models are extensions of the NSC78 and NSC93 NN models, respectively. Compared to NSC89, NSC97 solved some deficiencies in the spin-spin interaction for the $\Lambda - N$ channel. There are 6 versions (a – f) of the NSC97 potential. They describe the scattering YN data equally well, but differ in their s -wave interaction. The NSC models include the following

meson exchanges:

- Pseudoscalar mesons ($J^{PC} = 0^{-+}$): π, η, η', K .
- Vector mesons ($J^{PC} = 1^{--}$): ρ, ω, ϕ, K^* .
- Scalar mesons ($J^{PC} = 0^{++}$): a_0, σ, f_0, κ .
- Pomeron and the tensor mesons ($J^{PC} = 2^{++}$): P, f_2, f_2', a_2 .

Meson-exchange diagrams for YN potentials within the NSC models are shown in Fig. 1.5. Hypercharge (H) is equal to 0 for the direct diagram, while H is not equal to 0 for the exchange diagram, which can only occur when the exchanged boson is a strange boson. The flavor SU(3) symmetry is used to obtain the YN coupling constants from NN couplings, whereas SU(3) is broken by several factors like the baryon and meson masses, meson-mixings within the meson-nonet, and the charge-symmetry breaking (CSB) due to $\Lambda - \Sigma^0$ mixing. In the NSC YN models, some parameters are fixed by theory, other parameters are obtained from fits to experimental NN data, while several other parameters have to be determined by fits to experimental YN data.

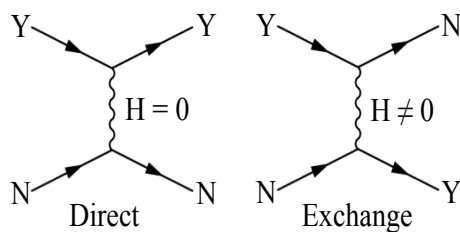


Figure 1.5: One-boson-exchange diagrams for the YN potentials within the Nijmegen soft-core model. The left figure shows the direct diagram, and the right figure shows the exchange diagram.

Table 1.2 lists the values of several free parameters, such as the magnetic vector-meson $F/(F+D)$ ¹ ratio, α_v^m , the scalar $F/(F+D)$ ratio, α_s , and scalar-meson mixing

¹In potential models, antisymmetric couplings are called F-type couplings, while symmetric couplings are called D-type couplings. F and D denote coupling constants of F-type and D-type couplings, respectively.

Table 1.2: Examples of free parameters of the NSC89 and the NSC97(a–f) models. α_v^m denotes the magnetic vector-meson F/(F+D) ratio, α_s denotes the scalar F/(F+D) ratio, and θ_s is the scalar-meson mixing angle.

Model	α_v^m	α_s	θ_s
NSC89	0.275	1.286	40.90°
NSC97a	0.4447	1.086	37.07°
NSC97b	0.4247	1.091	37.32°
NSC97c	0.4047	1.096	37.57°
NSC97d	0.3847	1.111	38.31°
NSC97e	0.3747	1.123	38.88°
NSC97f	0.3647	1.138	39.65°

angle, θ_s , obtained by fitting the NSC89 [10] and the NSC97(a–f) [11] models to 35 low-energy YN scattering data.

Another method to construct baryon-baryon potentials is provided by chiral EFT. The pioneering work in this field was done by Weinberg [16, 17]. His formulation was based on the underlying principle that if one starts from the most general Lagrangian consistent with all symmetries of the underlying interaction, one will get the most general S-matrix consistent with these symmetries, together with a power counting scheme that specifies which terms are required for a desired accuracy [18]. A recent chiral YN potential [13] was constructed using a modified Weinberg power counting of nuclear forces, while assuming that the YN interaction is related to the NN interaction via the flavor SU(3) symmetry. At leading order, the potential is entirely given by two types of contributions: longer-range one-pseudoscalar-meson exchanges and shorter-range four-baryon contact interactions. The one-pseudosclar-meson-exchange and the four-baryon-contact-term diagrams are show in Figs. 1.6 and 1.7, respectively. The s -wave four-baryon contact interactions contain 5 free parameters, which have been determined from fits to the 35 YN data points. Table 1.3 lists values of the free parameters for various cut-off masses. They can be used to obtain the YN partial wave potentials derived from chiral EFT.

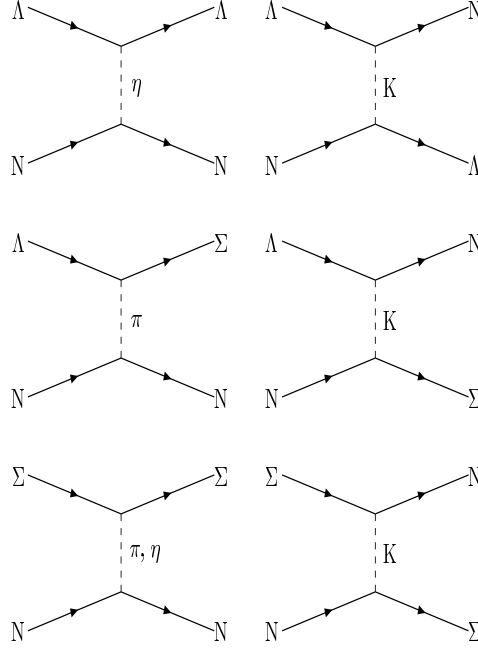


Figure 1.6: One-pseudoscalar-meson-exchange diagrams for the hyperon-nucleon interaction used in the chiral EFT of [13].

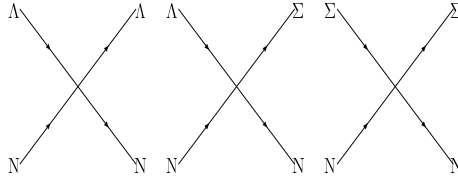


Figure 1.7: Lowest order contact terms for the hyperon-nucleon interaction used in the chiral EFT of [13].

Table 1.3: Free parameters of the YN contact terms for various cut-off masses. The parameters can be used to obtain the YN partial wave potentials derived from chiral EFT.

Cut-off Mass (MeV)	550	600	650	700
$C_{1S0}^{\Lambda\Lambda}$	-0.0467	-0.0536	-0.0520	-0.0516
$C_{3S1}^{\Lambda\Lambda}$	-0.0214	-0.0162	-0.0097	-0.0024
$C_{1S0}^{\Sigma\Sigma}$	-0.0797	-0.0734	-0.0738	-0.0730
$C_{3S1}^{\Sigma\Sigma}$	0.0398	0.2486	0.1232	0.1235
$C_{3S1}^{\Lambda\Sigma}$	0.0035	-0.0063	-0.0048	-0.0025

Since the fundamental theory of the interactions between the baryons is QCD, one should be able to describe the YN interaction in terms of the underlying degrees of freedom of QCD, the quarks and the gluons. This is a very complex problem that is difficult to solve. Lattice QCD is the only choice to carry out a first-principles QCD derivation of the YN interaction. A first fully-dynamical calculation was attempted by [14]. This study provided rigorous theoretical constraints on effective field theory and potential model constructions of YN interactions.

1.4 THE REACTION $\vec{\gamma}d \rightarrow K^+ \vec{\Lambda}n$

Experimental Motivation

In the past decades, a large number of NN and YN scattering experiments were performed to develop proper baryon-baryon potentials and to constrain the values of their parameters. A very comprehensive NN scattering data, both polarized and unpolarized, have led to a substantial progress in the understanding of the NN interaction. However, limited YN scattering data lead to significant uncertainties in modern YN potentials, which restricts the comprehension of the YN interaction. While performing elastic YN scattering experiments is difficult due to the short lifetime of hyperons, alternative approaches, such as hypernuclear spectroscopy [19] or studies of re-scattering in hyperon production experiments, were proposed to investigate the available YN potential models. In particular, exclusive hyperon photoproduction off deuteron is an attractive choice due to the simplicity of the target, and the ability to select kinematics where final-state interactions between the hyperon and the spectator nucleon are enhanced [6]. Additionally, experiments with electromagnetic probes have the advantage that the electromagnetic interaction in the initial state is well understood.

Main Mechanisms

The suitability of the $\gamma d \rightarrow K\Lambda N$ reactions to differentiate among different YN potential models and to constrain the YN low-energy scattering parameters has been studied in a large number of publications [6, 20, 21, 22, 23, 24, 25, 26, 27]. In these reactions the strange particles are produced in a first step on one of the nucleons in the deuteron and then the hyperon scatters quasi-elastically off the other nucleon in a second step. Access to the YN interaction is provided in this second step. The advantage of this method of study of the YN interaction is two fold. First, technical difficulties related to the production of a hyperon beam, such as in YN elastic scattering experiments, are avoided (the hyperon beam is produced in the nucleus). Second, the nucleons in the deuteron are very weakly bound and are almost on their mass shell (*i.e.* no significant corrections are needed due to many-body effects as in hypernuclear studies). The disadvantage is that one does not have directly full control over the first- and the second-step processes, meaning that contributions from other elementary mechanisms are an integral part of the data sample. Thus, in order to use exclusive $\vec{\gamma}d \rightarrow K^+ \vec{\Lambda}n$ data to extract information about the YN interaction, one needs a comprehensive theoretical model incorporating the full dynamics of the process. In this respect, the data do not provide a direct access to the Λn re-scattering, and the interpretation of our results will be model-dependent. The observables will be used to discriminate between different hyperon-nucleon potentials by comparing our results with model predictions. The best model developed for hyperon-nucleon studies using the $\vec{\gamma}d \rightarrow K^+ \vec{\Lambda}n$ reaction is that of [6]. Within this model, the main mechanisms contributing to the reaction are the quasi-free (QF) mechanism and several final-state interactions (FSI), including pion mediated scattering, Λn re-scattering, and Kn re-scattering. The corresponding diagrams are shown in Fig. 1.8. Overall, the QF mechanism dominates the cross section of the reaction.

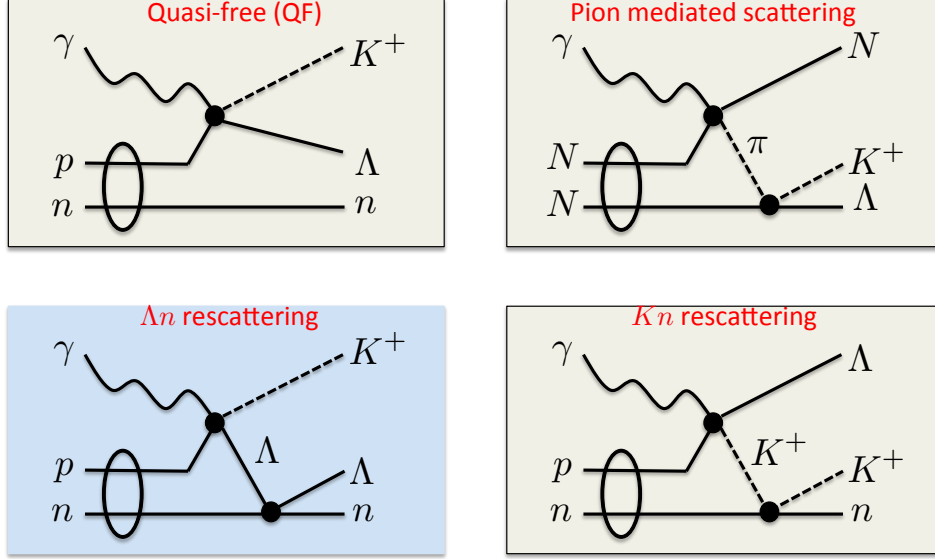


Figure 1.8: The four main mechanisms contributing to the reaction $\vec{\gamma}d \rightarrow K^+ \vec{\Lambda} n$ according to the model [6]. The diagrams show quasi-free production (top left), pion-mediated production (top right), Λn rescattering (bottom left), and $K n$ rescattering (bottom right). The latter three mechanisms are all final-state interactions.

Observables in Hyperon Photoproduction

The objective of this project is to extract the polarization observables C_x , C_z , and P_y for FSI in the reaction $\vec{\gamma}d \rightarrow K^+ \vec{\Lambda} n$ from data taken in the Jefferson Lab (JLab) experiment E06-103 [28] for photon energies between 0.9 GeV and 2.6 GeV and over a broad range of K^+ and Λ scattering angles. For Λ photoproduction off an unpolarized free-nucleon target with unpolarized beam, parity conservation in electromagnetic production allows induced polarization P_y of the Λ only along an axis perpendicular to the reaction plane $\hat{\gamma} \times \hat{K}^+$ [29]. However, when the incoming photons are circularly polarized, that is, when the photons are spin polarized parallel or anti-parallel to the beam direction (*i.e.* the beam has a net helicity), then this polarization may be transferred in whole or in part to the produced hyperons, giving rise to hyperon polarization components in the reaction plane. C_x and C_z thus characterize the polarization transfer from a circularly polarized incident photon beam to a recoiling

Λ along mutually orthogonal axes in the reaction plane [30].

Experimentally, for a given photon energy E_γ , polarization observables in hyperon photoproduction are extracted by using the general expression Eq. (1.3) for the polarized differential cross section [31, 32].

$$\begin{aligned} \frac{d\sigma}{d\Omega d\varphi} = & (d\sigma/d\Omega)_{unpol} [1 - P_{lin}\Sigma \cos 2\varphi \\ & + \alpha \cos \theta_x (-P_{lin}O_x \sin 2\varphi - P_{circ}C_x) \\ & - \alpha \cos \theta_y (-P_y + P_{lin}T \cos 2\varphi) \\ & - \alpha \cos \theta_z (P_{lin}O_z \sin 2\varphi + P_{circ}C_z)], \end{aligned} \quad (1.3)$$

where $(d\sigma/d\Omega)_{unpol}$ is the unpolarized differential cross section; P_{lin} and P_{circ} denote the linear and the circular polarization of the photon beam, respectively; φ is the azimuthal angle between the linear photon polarization vector and the reaction plane $\hat{\gamma} \times \hat{K}^+$; α is the self-analyzing power of the Λ , 0.642 ± 0.013 [33]; $\cos \theta_x$, $\cos \theta_y$ and $\cos \theta_z$ denote the direction cosines of the three-momentum vector of the decay proton in the rest frame of Λ ; Σ , P_y , T , O_x , O_z , C_x , and C_z are polarization observables: beam spin asymmetry, Λ induced polarization, target polarization, polarization transfers to the Λ from linearly polarized photons, and polarization transfers to the Λ from circularly polarized photons, respectively. For the reaction of interest, which has three final-state particles, this expression is incomplete. However, Eq. (1.3) can be used to extract the observables aimed for in this project.

After integrating over φ from 0 to 2π , the terms with linear polarization cancel, and Eq. (1.3) can be simplified into Eq. (1.4) in terms of C_x , C_z , and P_y under consideration of the helicity of the photons

$$\frac{d\sigma^\pm}{d\Omega} = \frac{d\sigma}{d\Omega}|_{unpol} (1 \pm \alpha P_{circ}C_x \cos \theta_x \pm \alpha P_{circ}C_z \cos \theta_z + \alpha P_y \cos \theta_y), \quad (1.4)$$

where $+$ and $-$ represents positive and negative photon helicity, respectively.

Theoretical Studies

As mentioned earlier, the most comprehensive model for the study of the reaction $\vec{\gamma}d \rightarrow K^+ \vec{\Lambda}n$ is the one of Miyagawa *et al.* [6], which not only predicts cross sections but also polarization observables. In addition to the QF mechanism, full FSI are included. The production operator in the model is written as

$$T_{\lambda}^{\gamma K} = T^{\gamma K} + T_{K\pi}^{\gamma K} + T_{\Lambda N}^{\gamma K} + T_{KN}^{\gamma K}, \quad (1.5)$$

where the four terms on the right-hand side denote the contributions of the four mechanisms shown in Fig. 1.8. Kinematic variables are defined in the coordinate system shown in Fig. 1.9, which is also the coordinate system used in this work. Figure 1.10 shows the kinematic evolution of five observables predicted by the model. The results from a Plain Wave Impulse Approximation (PWIA) [22] refer to QF production only, without any FSI. The two Nijmegen potentials, NSC89 and NSC97f, give very different predictions for the polarization observables. Variations between the predictions with the two potentials are of the order of 10% and are more pronounced at larger hyperon polar angles. Differences between the values of several free parameters of NSC89 and NSC97f are shown in Table 1.2. Furthermore, the sensitivity of the predicted observables to various YN potentials varies significantly between different models. For example, the model of Li and Wright [34] predicts variations in the unpolarized differential cross section of up to 50%. Thus, experimental observables of the $\vec{\gamma}d \rightarrow K^+ \vec{\Lambda}n$ reaction have the potential to significantly contribute to the YN studies. The study in this work is also very timely, since extensive measurements of the elementary first-step process $\vec{\gamma}p \rightarrow K^+ \vec{\Lambda}$ are now becoming available as a result of nucleon-resonance programs actively carried out at Jefferson Lab and other facilities. Moreover, the elementary process is measured in complete experiments, meaning all of its helicity independent amplitudes will be determined from the data. These results will reduce the uncertainties in the modeling of this reaction and will

improve the theoretical interpretation of our data.

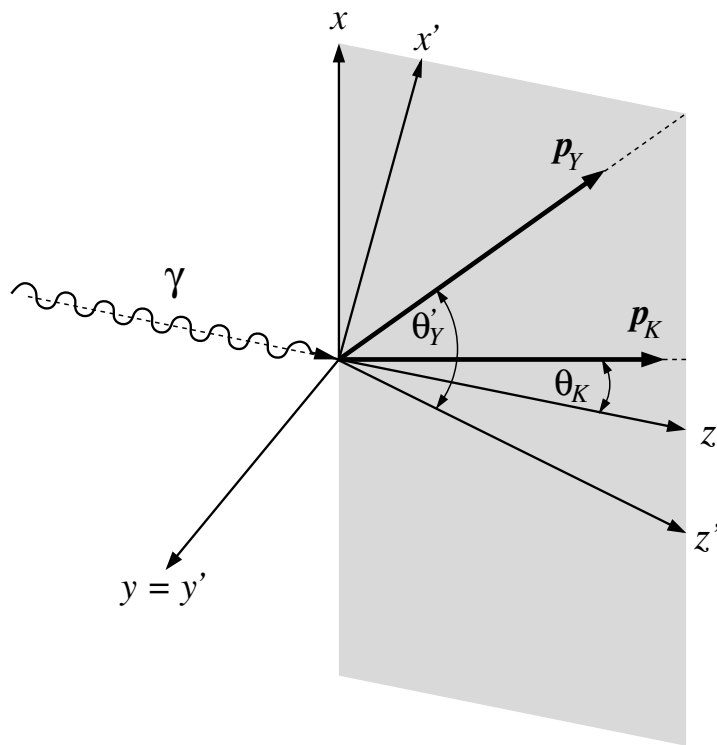


Figure 1.9: The axis convention adopted in the model [6]. The z axis points into the photon beam direction \vec{p}_γ . The kaon momentum, \vec{p}_K , lies in the $x - z$ plane. The momentum transferred to the YN system, $\vec{p}_\gamma - \vec{p}_K$, defines the z' axis. The hyperon angle θ'_Y is measured from the z' axis. The figure is from [6].

A formalism to extract the spin-singlet and the spin-triplet ΛN scattering lengths, a_{1S0} and a_{3S1} , has been developed by Gasparyan *et al.* [26]. In this approach, a dispersion integral is derived that allows to relate ΛN invariant-mass spectra to the scattering lengths. The method has been successfully applied to inclusive K^+ hadroproduction ($pp \rightarrow K^+\Lambda p$) [3]. By fitting the differential cross section as a function of the invariant mass of the p - Λ state, shown in Fig. 1.11, and by using the scattering length formalism, the hadro-production data yielded a spin-averaged scattering length of $-1.5 \pm 0.15 \pm 0.3$ fm [27]. The formalism can be applied to the observables obtained in this work to obtain an estimate for a spin-average Λn scattering length. It must be pointed out that the fits to each observable, C_x , C_z , or P_y are not expected

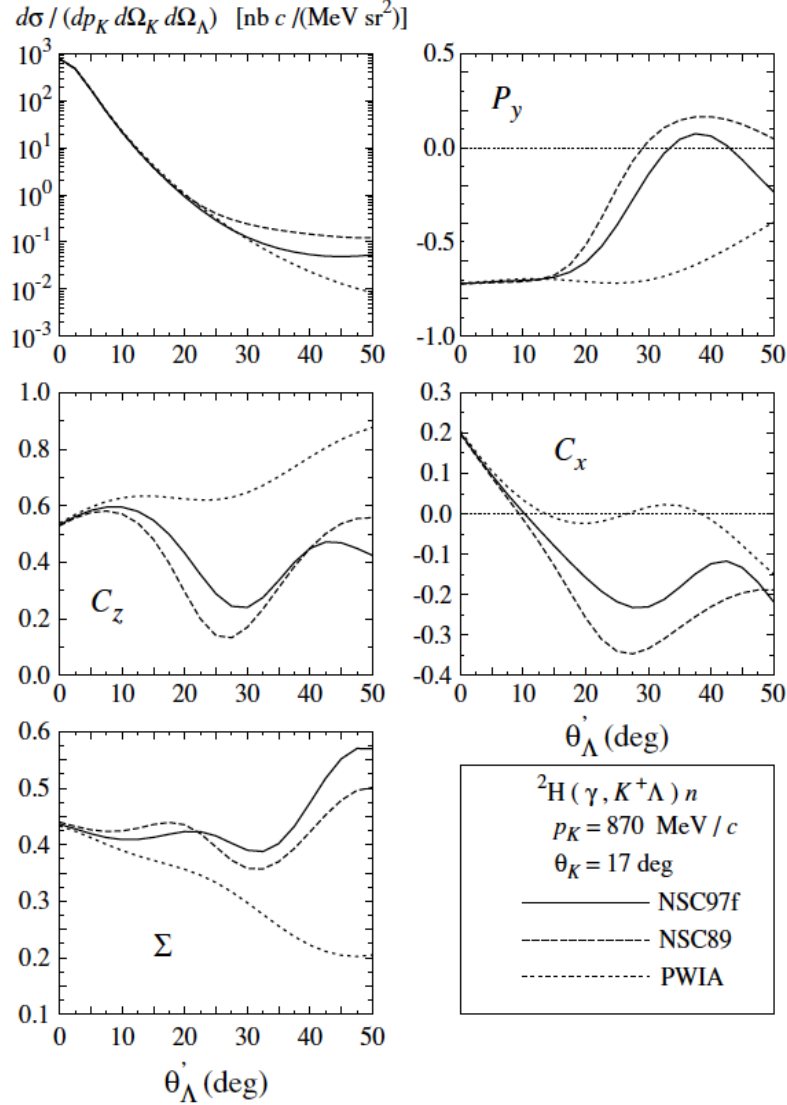


Figure 1.10: Unpolarized differential cross section and polarization observables for $\vec{\gamma}d \rightarrow K^+ \vec{\Lambda} n$ as a function of the hyperon polar angle θ'_Λ . The kaon lab momentum is fixed at $p_K = 870$ MeV/c, and the kaon polar angle is fixed at $\theta_K = 17$ deg. The results obtained from two YN potentials (NSC89 and NSC97f) are compared with the results from a Plain Wave Impulse Approximation (PWIA) [22].

to yield the same value of the scattering length, since the observables are different combinations of the $\Lambda n \rightarrow \Lambda n$ helicity amplitudes. A model needs to be applied further to estimate the spin-singlet and the spin-triplet scattering lengths. Only fits to data with polarized deuteron target would yield separate estimates for a_{1S0} and a_{3S1} [26]. Table 1.4 lists the values of a_{1S0} and a_{3S1} in the NSC97(a-f) models. One can see that the scattering lengths vary significantly from model to model, sometimes by a factor of two or more.

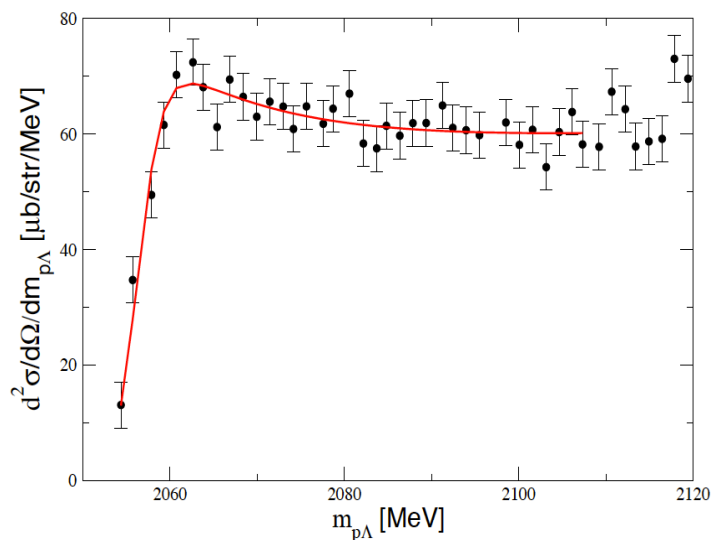


Figure 1.11: Differential cross section as a function of $IM_{p\Lambda}$ for the reaction $pp \rightarrow K^+\Lambda p$. The figure is from [27].

Past Experimental Results

The results for C_x , C_z , and P_y for FSI of $\vec{\gamma}d \rightarrow K^+ \vec{\Lambda}n$ obtained in this work are the first ever to be obtained. No previous data on exclusive hyperon photoproduction off the deuteron have been published so far. For systematic studies, we also extracted C_x , C_z , and P_y for the quasi-free mechanism, *i.e.* for $K^+\Lambda$ photoproduction off the bound proton. Our quasi-free results can be compared to published results [30, 35, 36, 37, 38]

Table 1.4: Values of the isospin-singlet and isospin-triplet Λn scattering lengths, a_{1S0} and a_{3S1} , for NSC97(a-f). One can see that the scattering lengths are poorly constrained.

Model	a_{1S0} (fm)	a_{3S1} (fm)
NSC97a	-0.76	-2.14
NSC97b	-0.97	-2.08
NSC97c	-1.28	-2.06
NSC97d	-1.82	-1.93
NSC97e	-2.24	-1.82
NSC97f	-2.68	-1.66

Table 1.5: Published results of C_x , C_z , and P_y from different experiments.

Experiment	Ref(s)	C_x	C_z	P_y
CLAS g1c	[35, 30]	★	★	★
CLAS g11	[36]			★
SAPHIR	[37]			★
GRAAL	[38]			★

(for full list of experiments and observables see Table 1.5) for the reaction $\vec{\gamma}p \rightarrow K^+ \vec{\Lambda}$.

Figure 1.12 shows published data for P_y for the reaction $\vec{\gamma}p \rightarrow K^+ \vec{\Lambda}$ from different experiments. In the figure, W denotes the square of the center-of-mass (CM) energy, and $\theta_K^{c.m.}$ denotes the K^+ polar angle in the CM system.

Figures 1.13 and 1.14 show C_x and C_z for the reaction $\vec{\gamma}p \rightarrow K^+ \vec{\Lambda}$ from the CLAS Collaboration [30], respectively. The results are compared to various theoretical models [39, 40, 41, 42].

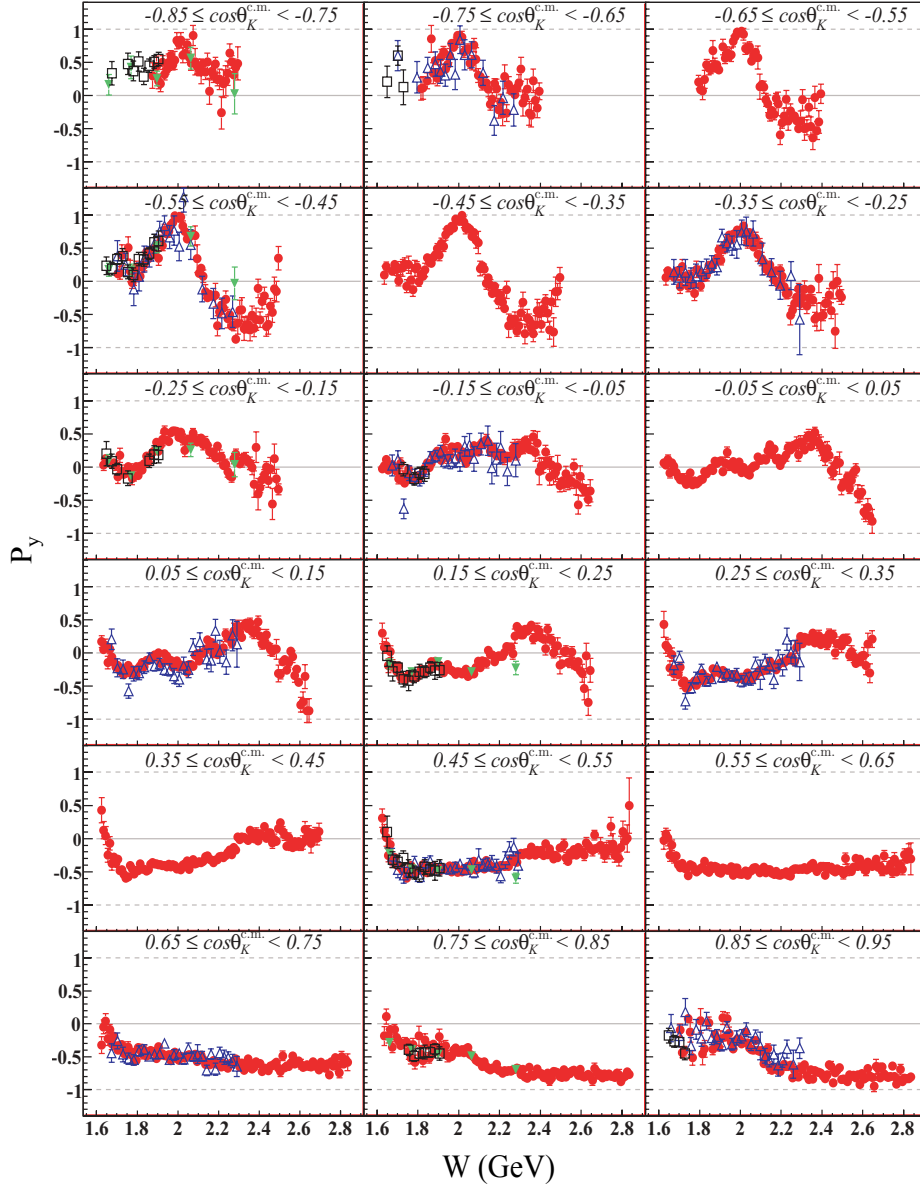


Figure 1.12: P_y vs. W in bins of $\cos\theta_K^{c.m.}$ for different experiments. Results from CLAS 2010 [36] are shown by the red solid circles, results from CLAS 2004 [35] are shown by the open blue triangles, results from SAPHIR [37] are shown by the solid green triangles, and the results from GRAAL [38] are shown by the open black squares. The figure is from [36].

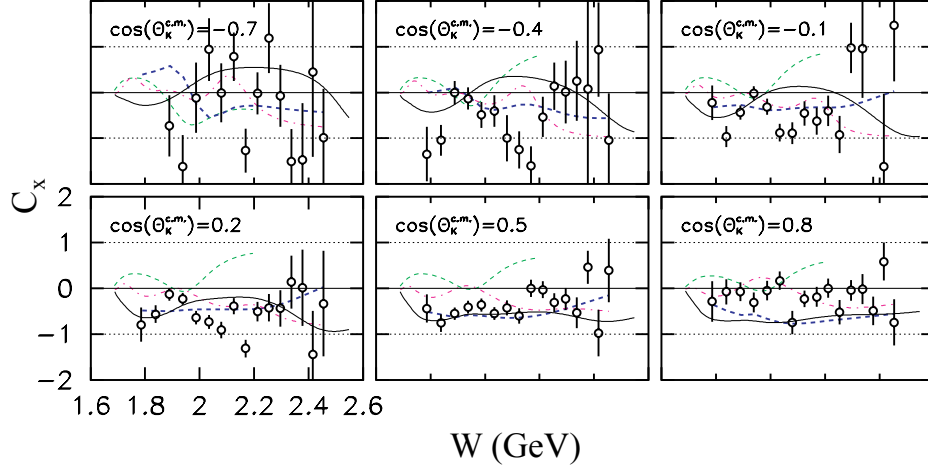


Figure 1.13: C_x vs. W in bins of $\cos \theta_K^{c.m.}$ from the glc experiments [30]. The open circles show the experimental results. Thin-dashed (green) curves are from Kaon-MAID [41], thick-dashed (blue) curves from BG [42], thin solid (black) from RPR [39], and thick dot-dashed (magenta) from GENT [40]. The figure is from [30].

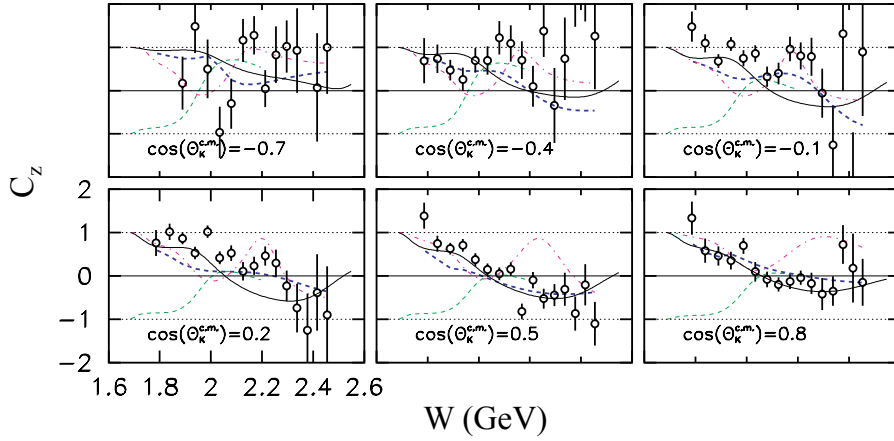


Figure 1.14: C_z vs. W in bins of $\cos \theta_K^{c.m.}$ from the glc experiments [30]. The open circles show the experimental results. Thin-dashed (green) curves are from Kaon-MAID [41], thick-dashed (blue) curves from BG [42], thin solid (black) from RPR [39], and thick dot-dashed (magenta) from GENT [40]. The figure is from [30].

CHAPTER 2

EXPERIMENTAL FACILITY

The data analyzed in this work was collected in the experiment E06-103 [28] conducted at the Thomas Jefferson National Accelerator Facility. General running conditions involved a circularly-polarized real-photon beam incident on an unpolarized liquid deuterium target. The real-photon beam was a product of both the Continuous Electron Beam Accelerator Facility (CEBAF) [43] and the Hall-B photon tagging system [44]. CEBAF provided the electron beam that was used to produce the photon beam using the bremsstrahlung technique. The Hall-B photon tagger was used to determine the energy of the photons interacting in the target. Final-state particles produced in nuclear reactions in the target were detected by the CEBAF Large Acceptance Spectrometer (CLAS) [45], also housed in Hall B.

2.1 THE CONTINUOUS ELECTRON BEAM ACCELERATOR FACILITY

CEBAF (see Fig. 2.1) provides polarized electron beam for three end-stations (Halls A, B and C). The electron beam originates from an injector, which is composed of a GaAs photoemission electron gun, a radio-frequency (RF) accelerating cavity, and an optical chopper. The electron gun uses three separate laser systems to deliver the beam to the three halls simultaneously. Each laser produces a pulse with a frequency of 499 MHz. The three laser pulses with 120° phase separation are optically combined to form a 1497 MHz pulse train, illuminating a GaAs photocathode to emit polarized electrons. The polarization of the electron beams is 70% – 80% as measured by polarimeters in the injector and the halls [46]. A half-wave plate (HWP) is periodically

inserted into one laser path to reverse the sign of the electron beam polarization. The status of the HWP determines the helicity of the circularly-polarized photon beam (more details about the status of the HWP during the E06-103 experiment are given in section 3.1). The electron beam is accelerated by superconducting RF cavities operating at 1497 MHz. Two superconducting RF parallel linacs joined by magnetic 180° recirculation arcs increase the beam energy by $2 \times 0.4 \text{ GeV} - 2 \times 0.6 \text{ GeV}$ in each turn. The beam is recirculated up to five times to reach a maximum energy up to 6 GeV, and is allowed to be simultaneously delivered to the halls at 499 MHz in the form of bunches. The microbunches can be loaded with different current, depending on the operation requirements of the experimental halls [47]. During the E06-103 experiment discussed in this thesis, the current delivered to Hall B was 40 nA. Halls A and C were typically operating at beam currents of $100 \mu\text{A}$.

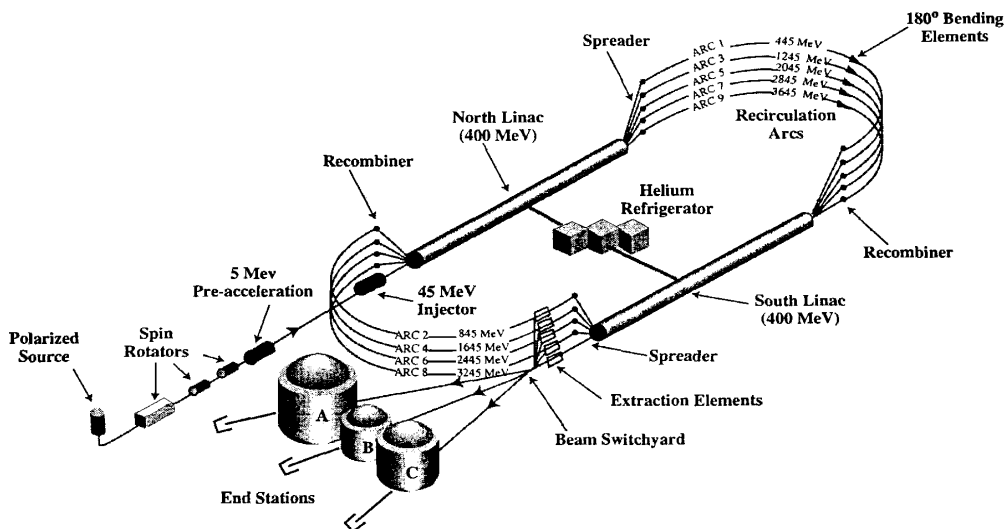


Figure 2.1: Schematic diagram of CEBAF at the Thomas Jefferson Accelerator Facility (JLab). The figure is from [48].

2.2 HALL B AND THE CLAS DETECTOR

Hall B Beamline

The beamline setup used in Hall B is shown in Fig. 2.2. Hall B can operate in three different modes for photon beams: an unpolarized mode, a circularly-polarized mode, and a longitudinally polarized mode. The data discussed in this work was collected using a circularly-polarized photon beam. The circularly-polarized photon beam is obtained when a linearly-polarized electron beam is incident on a thin amorphous radiator, typically a gold-plated carbon foil with a thickness of 5×10^{-5} to 3×10^{-4} radiation lengths. The foil is located 0.5 m in front of the tagging magnet. The beam after the radiator is mixed as it contains both photons and electrons. The electrons are bent by the dipole magnet of the tagging spectrometer away from the beam line, while the photons move straight towards the target. In E06-103, the photon beam was collimated by a pair of collimators before it impinged on the target. The polarization of the electron beam is measured by a Møller polarimeter located upstream of the tagging spectrometer. Another device, which is relevant in real-photon-beam experiments is the total absorption shower counter (TAC) located downstream of the CLAS. TAC measures the number of photons in the photon beam at a very low electron beam current (5 nA), which is needed for intensity calibration of the tagging system. The calibration allows to determine the absolute photon flux at nominal electron beam currents. The absolute photon flux is used to determine nuclear reaction cross sections and for data quality control.

Photon Tagger

The photon tagging system in Hall B is used to determine the energy of the photon beam and the time of the photons at the target. This is done by detecting the electrons that radiated bremsstrahlung photons in the radiator. A dipole magnet

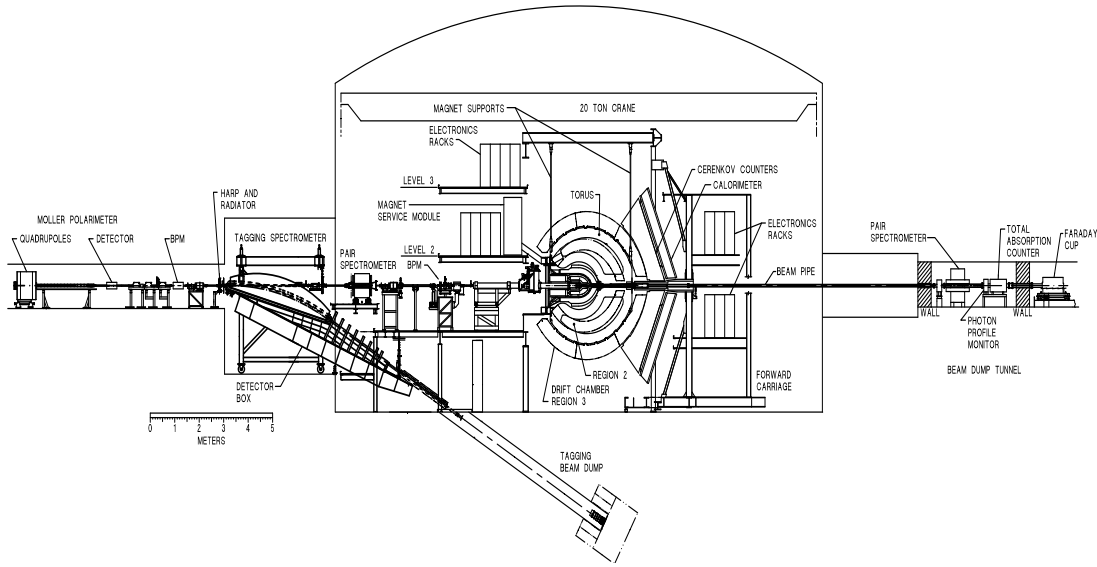


Figure 2.2: Schematic diagram of the Hall-B beam line during real photoproduction experiments. Important beam-line components include the Møller polarimeter, the bremsstrahlung radiator, the tagger magnet, the electron beam position monitors, and the total absorption shower counter. The figure is from [45].

bends the electrons on trajectories with radii depending on the electron energy. A hodoscope located in the focal plane of the magnet measures the position and the arrival time of the electrons. The electron energy, E' , is determined from the electron hit position in the hodoscope. The nominal energy of the electron beam in Hall B, E , is determined by the accelerator settings and by precision measurements in Hall A or Hall C. Then, the energy of the corresponding bremsstrahlung photons, E_γ , is determined as $E_\gamma = E - E'$. The tagging system in Hall B allows for the determination of the photon energy over a range of 20% to 95% of the incident electron energy. A schematic diagram of the tagging system is shown in Fig. 2.3. The focal-plane hodoscope consists of two detector planes of scintillation detectors. The first detector plane is comprised of 384 scintillator paddles referred to as E-counters. Each E-counter is 20-cm long and 4-mm thick. The widths of the E-counters range from 6 mm to 18 mm. The E-counters are used to determine the energy of the scattered

electrons by identifying their hit position in the hodoscope with a resolution of $0.001 \times E$ [44]. The second detector plane consists of 61 2-cm-thick scintillators (referred to as T-counters), which are used to determine the time of the incident electrons with a resolution of 110 ps [44].

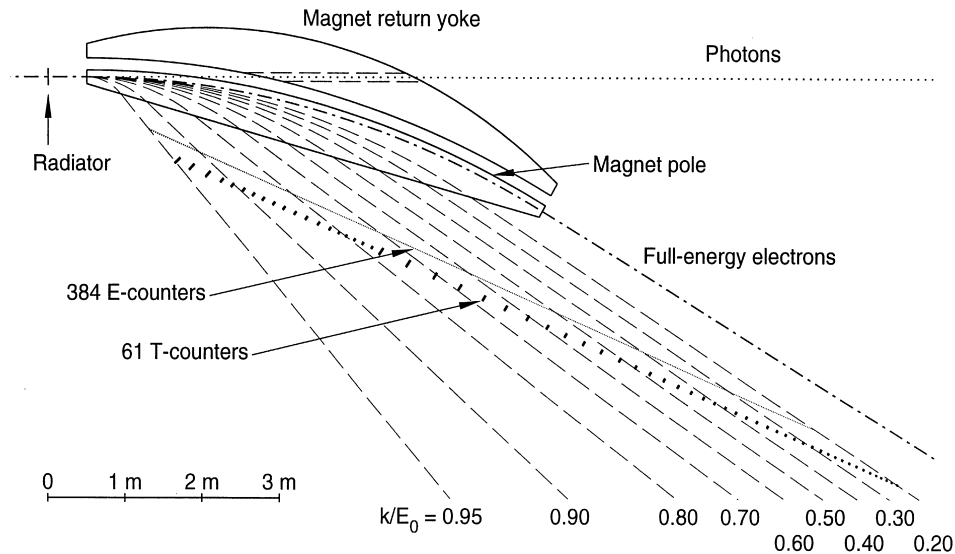


Figure 2.3: Schematic diagram of the Hall-B tagging system. The electron beam hits the radiator and produces bremsstrahlung photons. The electrons are then bent by a dipole field with their radius of curvature defined by their energy. These electrons are then detected by a set of scintillation detectors. The figure is from [44].

The CEBAF Large Acceptance Spectrometer

The data discussed in this thesis were taken with the CLAS, which operated in Hall B from 1995 to 2012. CLAS was being used to study photo- and electro-induced nuclear and hadronic reactions by providing efficient detection of multiple charged particles over a good fraction of the full solid angle [45]. CLAS was optimized to detect charged particles and had a limited acceptance for neutrals. The detector (see Fig. 2.4) was based on a six-coil toroidal magnet that provided a largely-azimuthal field distribution, and thus the whole detection system was divided into six inde-

pendent spectrometers (referred to as sectors). Trajectory reconstruction using drift chambers (DC) [49] resulted in a momentum resolution of 0.5% at forward angles. Time-of-flight (TOF) scintillators [50] and electromagnetic calorimeters (EC) [51] provided good particle identification: pion/kaon separation up to 2 GeV/ c , kaon/proton separation up to 2 GeV/ c , and pion/proton separation up to 3.5 GeV/ c [3]. A start counter (ST) [52] provided the time at which reactions occurred in the target for photon-beam experiments. Fast triggering and high data-acquisition rates allowed operation at a luminosity of $10^{34} \text{ cm}^{-2}\text{s}^{-1}$. These capabilities were being used in a broad experimental program to study the structure and interactions of mesons, nucleons, and nuclei using polarized and unpolarized electron or photon beams and targets [45].

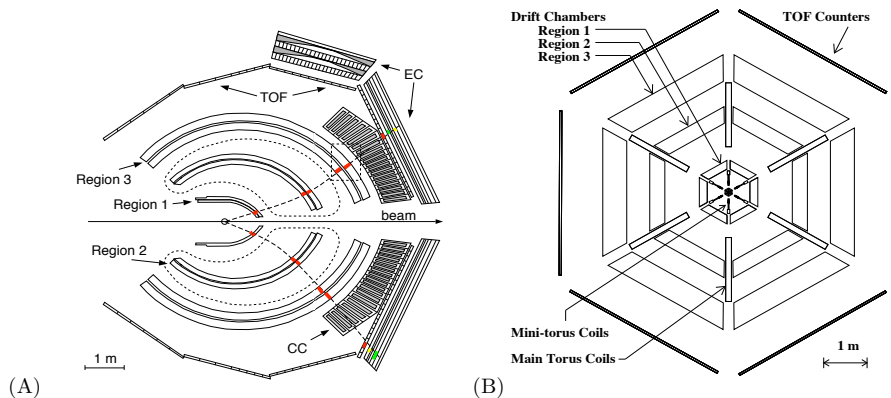


Figure 2.4: Schematic diagram of the CLAS. The detector is composed of a toroidal magnetic spectrometer, three regions of drift chambers, electromagnetic calorimeters, Cherenkov counters, and time-of-flight scintillators. (A) Cross section of the CLAS along the beamline, with typical charged-particle tracks shown. (B) Cross section of the CLAS perpendicular to the beamline. The mini-torus, as well as the Cherenkov Counter, shown in the middle is used only for electron runs. The Start counter used in real-photoproduction experiments is not shown on the diagram. The figure is from [45].

Torus magnet

The magnetic field in CLAS is generated by six superconducting coils (see Fig. 2.5) arranged in a toroidal geometry around the beam line. The field is oriented along the azimuthal direction except in locations close to the coils where there are significant deviations from a pure azimuthal field [45]. The CLAS toroidal magnet bends charged particles toward or away from the beam axis, but leaves the azimuthal angle essentially unchanged. During the E03-106 experiment, the torus field was set so that negatively-charged particles were out-bending while positively-charged particles were in-bending. The magnet was operated at a current of -1500 A, which produced 39% of the maximum field.

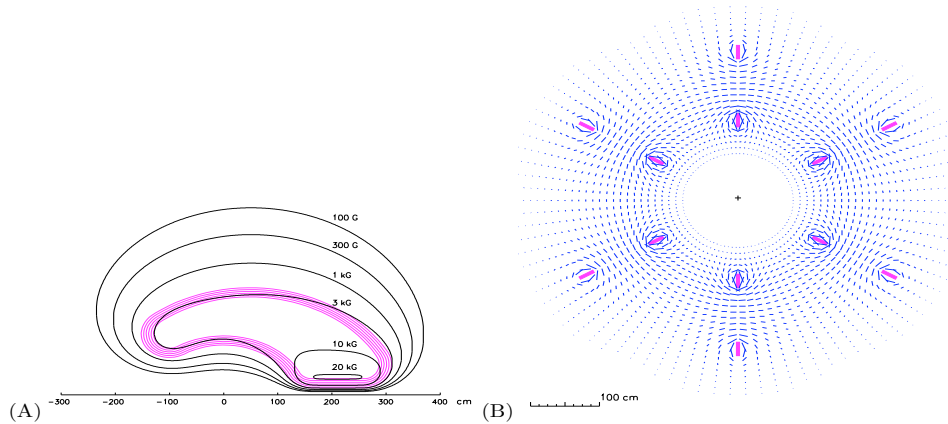


Figure 2.5: Geometry of the magnetic field produced by the CLAS torus. (A) Magnetic field strength in the plane between two of the torus coils. The magenta lines correspond to the projection of one of the coils onto the midplane. (B) Magnetic field vectors in the cross section of the CLAS perpendicular to the beamline. The magenta blocks indicate the location of the six torus coils. The figure is from [45].

Drift Chambers

The drift chambers are used to measure the trajectories of outgoing charged particles. 18 separate drift chambers are located at three radial positions in each of the six sectors. These radial locations are referred to as “Region”. This design of the DC

provides an average spacial resolution of $310 \mu\text{m}$, $315 \mu\text{m}$, and $380 \mu\text{m}$ for Region 1, Region 2, and Region 3, respectively (see Fig. 2.4). Trajectory reconstruction using the drift chambers results in a momentum resolution of $\Delta p/p \leq 0.5\%$ and angular resolutions of $\Delta\theta$ of 1 mrad and $\Delta\phi$ of 4 mrad [45].

Start Counter

The start counter (ST), shown in Fig. 2.6, is a scintillation detector that is used to identify the correct start time of an event for time-of-flight measurements. The detector is made up of six identical sectors surrounding the target cell. Each sector is composed of four scintillator paddles (for a total of 24 scintillators) coupled to an acrylic light guide that leads to a photomultiplier tube. The ST measures the interaction time in the target by detecting the outgoing particles with a time resolution of 350 ps. The design of the ST is such as to keep the rate due to electromagnetic background within acceptable values [52].

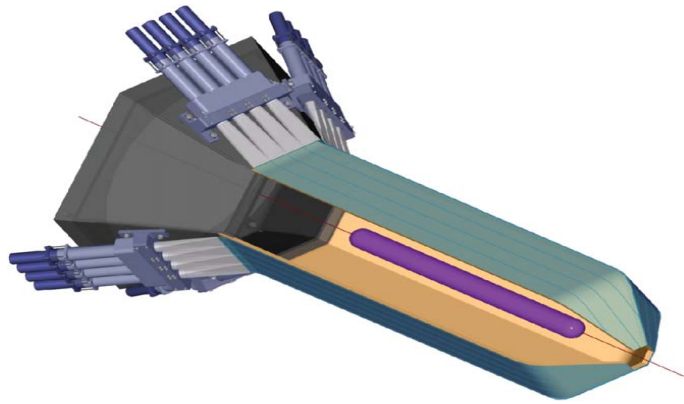


Figure 2.6: A 3-dimensional picture of the start counter. The scintillator paddles are shown in light green. To allow for coverage of forward going particles, the paddles are bent in the forward direction. The target cell is shown in purple. One can see the light guides and the photomultipliers in the backward directions. The figure is from [52].

Time-of-flight Detector

The time-of-flight detector [45] is an array of scintillation counters (57 scintillation paddles in each sector 1, 2, and 4, and 56 paddles in each sector 3, 5, and 6) positioned outside of the magnetic field. As with all the other CLAS detectors, the TOF counters are positioned in a radially symmetric arrangement around the target and cover each of the six sectors. The lengths of the paddles vary from 32 cm at the most forward angle to 450 cm at larger angles. The TOF covers the entire azimuthal angle ϕ (with the exception of the regions shadowed by the torus coils) and polar angles θ from 8° to 142° . The TOF counters are used to measure the time of flight of final-state particles inside the CLAS detector, and thus provide information about the speed of these particles. This information, along with momentum information provided by the drift chambers, allows for the reconstruction of charged-particle masses and, thus, for charged-particle identification. The intrinsic time resolution of the TOF detector varies from about 80 ps for the forward counters to 160 ps for the backward counters.

Figure 2.7 shows the arrangement of TOF paddles within a sector. Photons are radiated after a charged particle passes through the scintillator and excites the material. Then, these photons are transmitted towards the two sides of the paddle. Finally, they are converted into current signals by photomultiplier tubes that are attached at each end of the paddles.

Electromagnetic Calorimeter

The forward electromagnetic calorimeter, which covers polar angles up to 45° , is used to detect electrons, photons, and neutrons. Although, information from the EC is not used in the analysis presented here, we give a short description of this CLAS component due to its importance in the detection of charge-neutral particles. This detection system also consists of 6 sectors. The structure of one sector of EC is shown in Fig. 2.8. It is made of 39 alternating layers of 10-mm thick scintillator strips

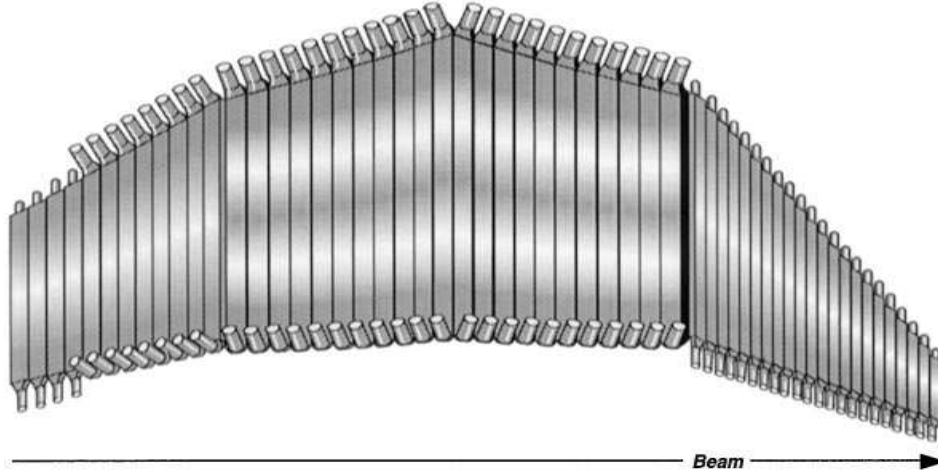


Figure 2.7: Schematic diagram of a set of 56 scintillator paddles that comprise one sector of the time-of-flight system. Each TOF paddle covers a narrow range of polar angle, which is important for matching the DC tracks with hits in the TOF. The figure is from [45].

and 2.2-mm thick lead sheets, and its total thickness is 16 radiation length. Each successive layer, whose shape is close to a triangle, consists of 36 stripes parallel to one side of the triangle. One layer is rotated by 120° with respect to the previous one, so 3 layers (labelled U, V, and W) form a cell (there are 13 cells in total in each sector). These cells are used to measure time and energy deposition of particles. Radiation, emitted by the interaction between particles with the lead sheets, is detected by the scintillators and converted into current signals by photomultiplier tubes [51].

2.3 THE E06-103 EXPERIMENT

The E06-103 experiment (also referred to as g13 experiment) contains two run periods, g13a with circularly-polarized photon beam and g13b with linearly-polarized photon beam. The data for this project were taken during the g13a period that ran between October and December of 2006 with an additional week in March 2007. The experiment was performed at two different electron beam energies (1.987 GeV and 2.649 GeV). Table 2.1 lists three datasets according to the periods of the experiment

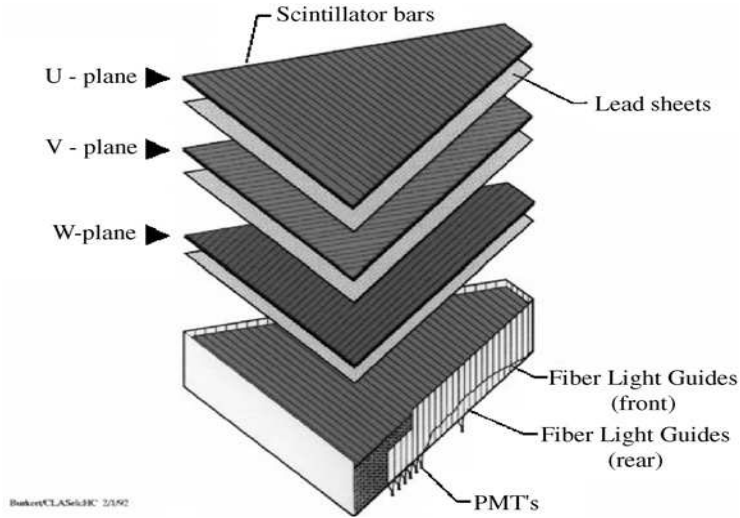


Figure 2.8: Schematic diagram of a sector of the forward electromagnetic calorimeter. One can see the successive layers of alternating orientation. The figure is from [51].

Table 2.1: A list of the data acquired in the g13a experiment. The data are classified according to electron beam energy and acquisition period. A run is a small set of data collected continuously over a period of about 2 hours. Each run consists of up to 100 data files. The experimental conditions were kept steady throughout a run.

Period	Electron Beam Energy	Run Number
October 30 – November 21, 2006	1.987 GeV	53164 – 53532
November 28 – December 22, 2006	2.649 GeV	53538 – 53862
March 12 – March 15, 2007	1.987 GeV	53998 – 54035

and their electron beam energies. The polarization of the electron beam was up to 85%. A current of -1500 A in the torus magnet produced a magnetic field that bent negatively-charged particles away from the beamline. The current was chosen such as to maximize the CLAS acceptance for low-momentum π^- that originated from hyperon decays [3]. A total of 20 billion events were collected during g13a. During g13b the total collected number of events was 30 billion.

The g13a experiment used a 40-cm-long unpolarized liquid deuterium (LD_2) target (see Fig. 2.9). The center of the target was located 20 cm upstream from the CLAS

center in order to increase the acceptance for forward-scattered particles. The LD_2 target with a thickness of $6.5 \text{ cm}^2/\text{g}$ and a density of $162 \text{ mg}/\text{cm}^3$ had the advantage of producing a luminosity that was more than an order of magnitude higher for a given set of running conditions than the luminosity that could have been obtained with a standard 5-cm-long polarized target. For systematic checks and detector alignment, a small set of data were acquired with a liquid hydrogen (LH_2) target of the same length and at the same location as the deuterium target.



Figure 2.9: Schematic diagram of the 40-cm long LD_2 target cell used in the g13 experiment. The figure is from [53].

A two-level hierarchical trigger system was used in the g13 experiment in order to acquire events of interest while minimizing deadtime. The deadtimeless Level 1 trigger processed all prompt photomultiplier signals through a pipelined memory lookup with a period of about 100 ns. After the Level 1 trigger signal had occurred, the event was stored, unless a fast-clear signal was issued within a period of time called the fast-clear window. The Level 2 trigger made use of this fast-clear capability to clear events that satisfied Level 1, but which had no tracks in DC [45]. During the g13a experiment, a two-sector trigger with a two-track Level-2 requirement was used, *i.e.* data acquisition required a coincidence between the ST and the TOF in at least

two of the six sectors of the CLAS detector [54].

To evaluate the g13a data quality, we extracted the number of exclusive $\vec{\gamma}d \rightarrow K^+ \vec{\Lambda} n$ events (details in Chapter 4) in each data file and divided that number by the corresponding number of photons incident on the target ¹. The timeline of the normalized yield for g13a data is shown in Fig. 2.10. The timeline shows that the data taken at electron energy of 1.987 GeV yield a lower normalized yield than the one taken at 2.649 GeV (which is expected as reaction rates depend on the experimental conditions). Within each of these data groups, the normalized yields show good consistency from file to file. To quantify the consistency, the yield distributions were fitted to a Gaussian (see Fig. 2.11) and the fit quality was examined - no bad data files were identified. The timeline of the photon-flux-normalized yield allows to identify significant changes in the overall detector response, *i.e.* CLAS and/or tagger acceptance, or in beam quality.

Further studies of data quality involving polarization-dependent control variables (details can be found in Section 3.1) identified several data runs inconsistent with the rest of the data set. Those were removed from further analysis.

¹For each data file, the number of corresponding photons incident on the target is produced routinely at raw-data processing by using a standard CLAS method [55].

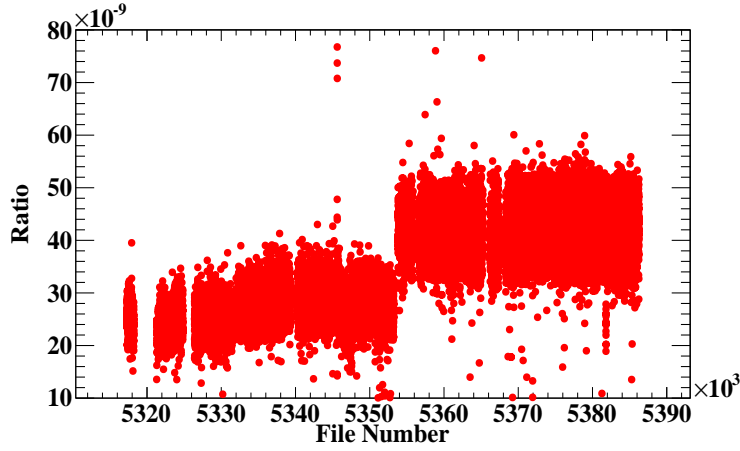


Figure 2.10: Timeline of the $K^+\Lambda n$ photon-flux-normalized yield. One can see that the data cluster around two distinct mean values. The latter correspond to the two different electron beam energies at which g13 ran. Within each cluster the normalized yields are consistent from file to file. Data of runs 53168 – 53862 are only used for this study. Runs 53164 – 53167 were not included in the data sample because they were not stable during the g13 experiment. Runs 53998 – 54035 are not shown on the figure as the number of the corresponding photons incident on the target for each of these runs was not available at the time of the study.

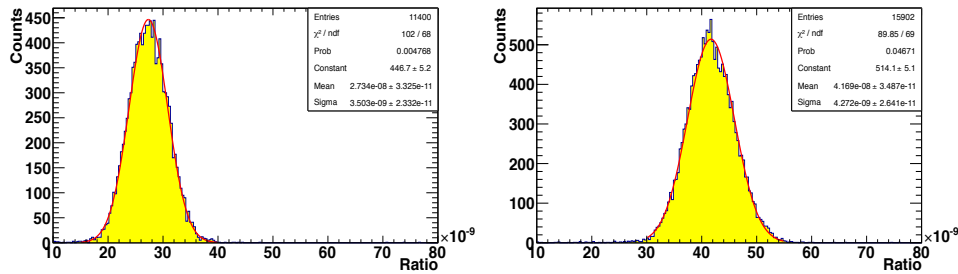


Figure 2.11: Distributions of normalized $K^+\Lambda n$ yields. Left: 1.987-GeV data files. Right: 2.649-GeV data set. The red lines show fits to a Gaussian function. The widths of the distributions are due to statistical fluctuations. No bad-quality data files are identified.

CHAPTER 3

HELICITY AND POLARIZATION OF THE PHOTON BEAM

3.1 PHOTON-BEAM HELICITY

In order to determine the absolute sign of the photon helicity for each run and to evaluate the quality of polarization data, we extracted the polarization transfer coefficient C_z for the quasi-free mechanism of the $\vec{\gamma}d \rightarrow K^+\vec{\Lambda}n$ reaction (*i.e.* for $K^+\Lambda$ photoproduction off the bound proton). The value of C_z was determined for each data run, while integrating over all photon energies and center-of-mass scattering angles. Previously published CLAS results [30] have shown that for the reaction $\vec{\gamma}p \rightarrow K^+\vec{\Lambda}$, C_z is positive (close to 1) over the full kinematic range covered by the g13a experiment. Since C_z for QF events should be close to that for $\vec{\gamma}p \rightarrow K^+\vec{\Lambda}$, we expect the integrated value of C_z over the full kinematic range covered by the CLAS to be positive and large. Negative values of the integrated C_z would mean that the status of the HWP was flipped and we could correct the sign of photon helicity for the corresponding data accordingly.

To extract the integrated value of C_z , for each data run $\vec{\gamma}d \rightarrow K^+\vec{\Lambda}n$ exclusive yields were first obtained, and then a missing-momentum cut was applied to remove final-state interaction events. Details about the yield extraction and the missing-momentum cut are given in Chapter 4. Finally, the distribution of the helicity asymmetry as a function of $\cos\theta_z$ was fitted to a straight line. The slope of the line is directly proportional to C_z . The fitting method is described in Section 5.1. Figure 3.1 shows the timeline of the fitted slope. Runs for which the slope is negative

were taken with inverted definition of “positive” helicity due to inverted status of the HWP. For all the events in those runs, the sign of the helicity was redefined. Several points on the timeline have large statistical uncertainties and fall within one to two standard deviations from the average slope. An example of the fitted helicity distribution for one such point is shown on Fig. 3.2. The statistical uncertainties of the data are large and the slope, although positive, is consistent with zero. In addition, some distributions do not exhibit a linear trend as expected. Low statistics and non-linear data have been removed from the analysis presented here.

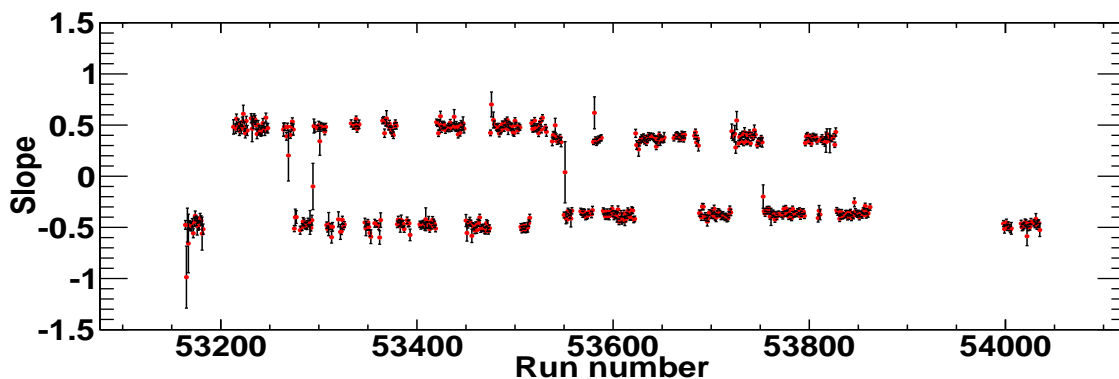


Figure 3.1: Timeline of the slope of a linear fit to the distribution of helicity asymmetry vs. $\cos\theta_z$. Negative slope means inverted definition of “positive” helicity, due to a reversed status of the HWP at the injector. For these runs the sign of the photon helicity was redefined.

3.2 ELECTRON BEAM POLARIZATION

In order to extract polarization observables from the g13a data, the magnitude of the photon polarization must be known. In order to obtain the latter, the electron beam polarization is needed. In Hall B of JLab, a Møller polarimeter located upstream from CLAS was used to directly measure the electron beam polarization. During the special runs when the Møller polarimeter was used, the tagger and the standard CLAS data acquisition were turned off. The results of electron polarization measurements

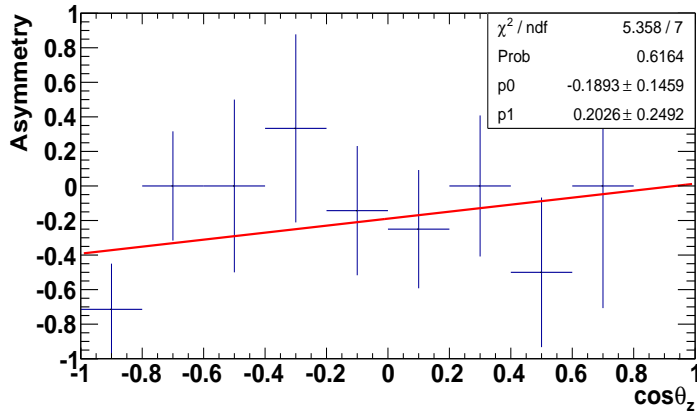


Figure 3.2: Helicity asymmetry vs. $\cos\theta_z$ for a bad-quality run. The red line shows a linear fit to the distribution. Low statistics data (as the one shown) and non-linear data are excluded from the analysis discussed in this work.

during the 1.987-GeV and 2.649-GeV run periods in 2006 of the g13a experiment are shown in Fig. 3.3, where the x axis shows the Møller run numbers. During the 1.987-GeV run period in 2007, *i.e.* runs 53998–54035 (not shown in the figure), only one electron beam polarization measurement was taken which yielded a polarization of $84.1\% \pm 1.1\%$ (as shown in Table 3.1). One can see that even though the electron beam energy was kept constant, the polarization of the electrons changed. The polarization change was traced back to a changing Wien angle at the injector. For a fixed value of the Wien angle, the Møller measurements randomly fluctuate about a mean value and there is no systematic dependence on the status of the half-wave plate. Thus, four weighted averages of the electron beam polarization, as shown in Table 3.1, were calculated for the four distinct run ranges.

3.3 PHOTON BEAM POLARIZATION

The polarization of the photon beam can be calculated using the Olsen and Maximon relation [56]

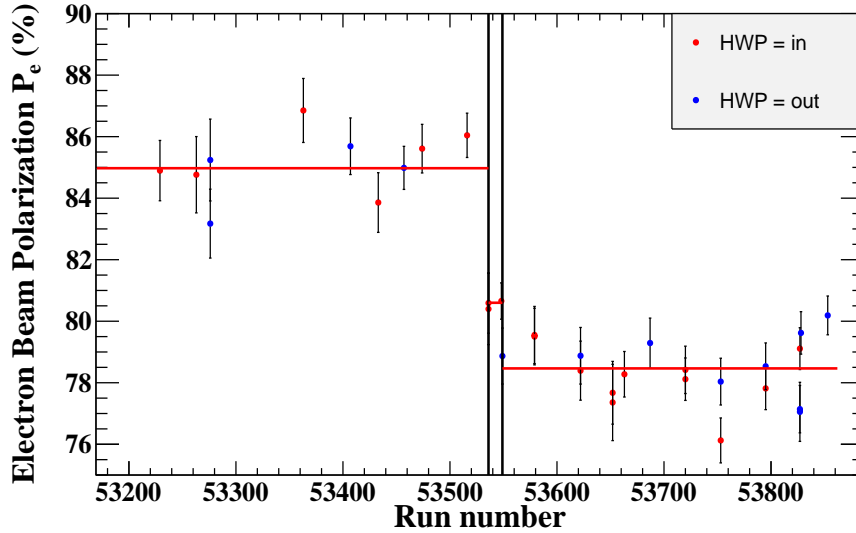


Figure 3.3: Electron-beam polarization measurements taken during the 1.987-GeV and 2.649-GeV run periods in 2006 of the g13a experiment. The two run periods are separated by the first vertical solid black line. The runs within the two vertical solid black lines were taken with a different Wien angle at the injector. The g13a experiment covers data taken at three different Wien angles, 92.246° , 90.844° , and 90.043° .

Table 3.1: Electron-beam polarization values obtained by averaging the set of Møller measurements taken throughout g13a. The four distinct run ranges, characterized with different values of the polarization, correspond to different values of the Wien angle at the injector.

Run	Electron Beam Energy	Wien Angle	Weighted Average
53164-53532	1.987 GeV	92.246°	$84.97\% \pm 0.28\%$
53538-53547	2.649 GeV	90.844°	$80.60\% \pm 0.18\%$
53550-53862	2.649 GeV	90.043°	$78.47\% \pm 0.18\%$
53998-54035	1.987 GeV	93.247°	$84.11\% \pm 1.1\%$

$$P_\gamma = \frac{E_\gamma(E + \frac{1}{3}E')P_e}{E^2 + E'^2 - \frac{2}{3}EE'}, \quad (3.1)$$

where E_γ is the photon energy, E is the electron beam energy, E' is the recoiling electron energy, and P_e is the electron beam polarization. In particular, with $x = E_\gamma/E_e$ and $E_\gamma = E - E'$, the photon beam polarization P_γ is given by

$$P_\gamma = P_e \frac{4x - x^2}{4 - 4x + 3x^2}. \quad (3.2)$$

Figure 3.4 shows the relation of the photon polarization (as fraction of electron polarization) versus the photon energy (as a fraction of the electron energy) for the final-state of interest in g13a. One can see that the photon polarization varies from 40% to 100% of the electron polarization, depending on the photon energy.

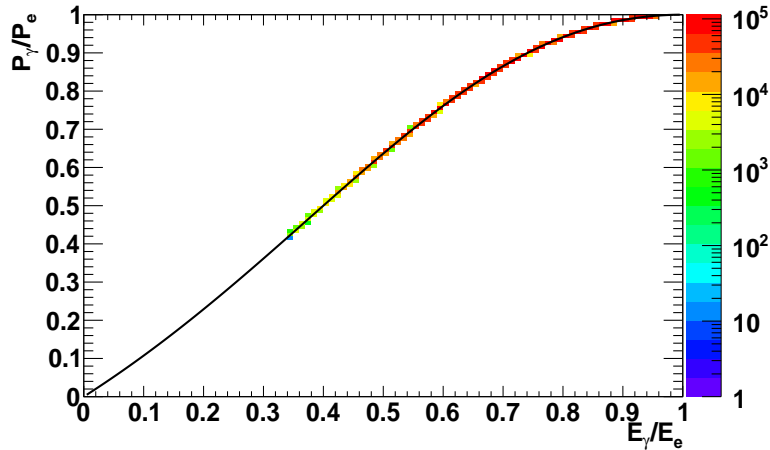


Figure 3.4: Ratio of P_γ to P_e as a function of the ratio of E_γ to E_e . The black line shows the function from Eq. (3.1). The colors reflect the amount of actual $K^+\Lambda n$ data for each photon energy.

CHAPTER 4

DATA ANALYSIS

This chapter describes in details the procedure to select the events of interest as well as identify and reconstruct the reaction $\vec{\gamma}d \rightarrow K^+ \vec{\Lambda} n$.

4.1 PARTICLE IDENTIFICATION (PID)

The main particle-identification method for charged particles detected in the CLAS is based on time-of-flight measurements. In this work, the method was applied as follows. The speed of the particle (in units of the speed of light, c), β_{meas} , was determined as

$$\beta_{meas} = \frac{l}{ct}, \quad (4.1)$$

where, t and l are the flight time and the flight path from the production vertex to the TOF detector. Then, for the same track, the expected speed, β_{calc} , was determined under a specific assumption for the particle identity, *i.e.* for its nominal mass

$$\beta_{calc} = \sqrt{\frac{p}{p^2 + m^2}}, \quad (4.2)$$

where p is the measured momentum of the particle and m is the nominal mass for a specific assumed identity. The difference

$$\Delta\beta = \beta_{meas} - \beta_{calc} \quad (4.3)$$

was then formed. When the nominal mass is the true particle mass, then $\Delta\beta$ should be consistent with zero within the experimental resolution. The particles of interest K^+ , proton, and π^- were each identified by applying a $\Delta\beta$ cut. To make particles of interest stand out, extra cuts, including event vertex, photon selection, and kinematic cuts were applied firstly, and then distributions of $\Delta\beta$ vs. p were studied for K^+ , proton, and π^- , separately. Figures 4.1 and 4.2 show event distributions of $\Delta\beta$ vs. p for proton and K^+ candidates, respectively. The red solid lines show the cut ranges we used to identify if a track was a proton or a K^+ . The points on the curves were determined by dividing the momentum range into sub-ranges and fitting the $\Delta\beta$ distribution in each sub-range to a Gaussian. The points on the curves show the $\pm 3\sigma$ range for each momentum bin. The discrete upper and lower range points were fitted to 3rd order polynomials (parameters are shown in Figs. 4.1 and 4.2), and the polynomials were used as PID cuts. The π^- were selected by applying the $\Delta\beta$ cut in the range of -0.2 to 0.2 where pions overwhelmingly dominate (see Fig. 4.3). The extra cuts were removed after the PID selection was finalized.

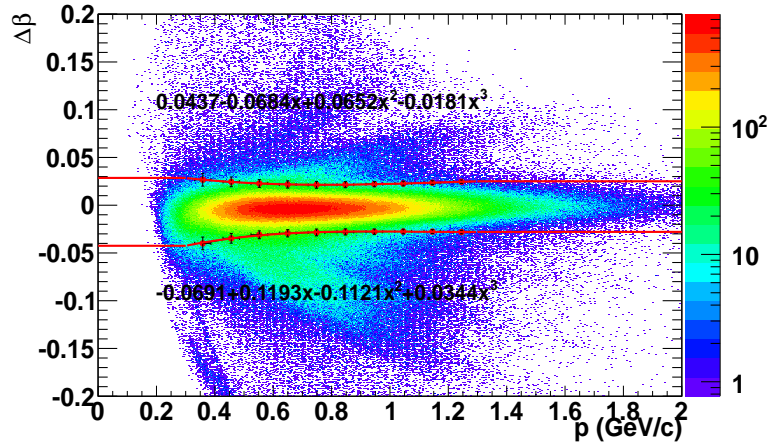


Figure 4.1: $\Delta\beta$ as a function of momentum for proton candidates. The red lines show the proton PID cut range. The curves are 3rd order polynomials, the parameters of which are given in the equations.

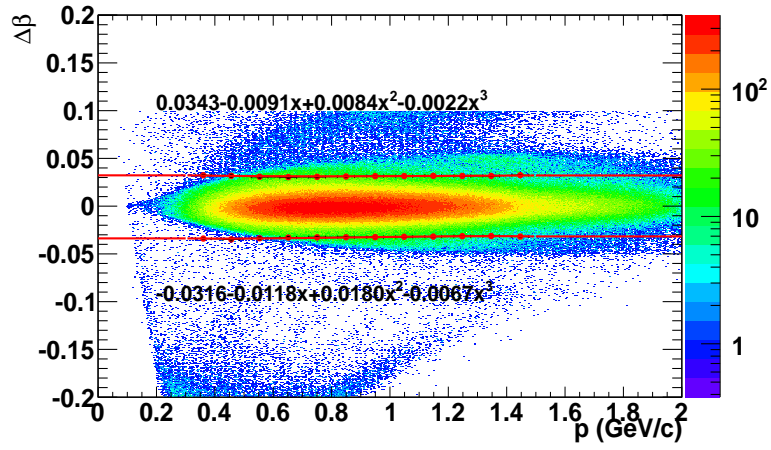


Figure 4.2: $\Delta\beta$ as a function of momentum for K^+ candidates. The red lines show the kaon PID cut range. The curves are 3^{rd} order polynomials, the parameters of which are given in the equations.

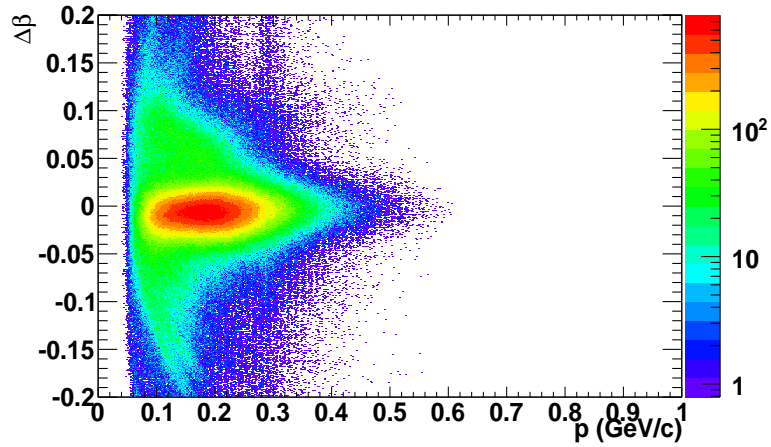


Figure 4.3: $\Delta\beta$ as a function of momentum for π^- candidates. Pions overwhelmingly dominate in the $\Delta\beta$ range of -0.2 to 0.2 .

Vertex Determination

In general, at least two final-state charged-particle tracks are needed in order to reconstruct the event vertex. For our final-state of interest, however, another solution is used since two (namely the proton and the π^-) out of the three detected particles do not originate from the primary $K^+\Lambda$ vertex. For this reaction, we use the tracks from the γ and K^+ to determine the event vertex. A line parallel to the beam line was used to represent the γ , with the beam x - and y -positions determined for each run using all multi-charged-track events for that run (the beam position was determined during the initial processing of the g13a data). The two tracks are not exactly coplanar due to the finite position resolution of the CLAS. Therefore, we applied a method called DOCA (Distance Of Closest Approach) to determine the location of the reaction vertex. Firstly, the line which was perpendicular to both tracks was determined. Secondly, the intersection point of the perpendicular line and each track was determined. Finally, the reaction vertex was determined by finding the bisector between these two points. Schematically, the reaction vertex and its determination from the kaon and the photon tracks are visualized in Fig. 4.4. Figure 4.5 shows the event distribution over the z -component of the reaction vertex. Only events with z -vertices from -40 cm to 0 cm were kept for further analysis.

4.2 PHOTON SELECTION

The g13a ran at an electron beam current of about 40 nA, with electron bunches delivered every 2.004 ns from CEBAF. The trigger window for digitizing data by the CLAS electronics was about 30 ns wide. Since the latter is an order of magnitude larger than the time between different beam bunches, and given the beam intensity, typically, 14 good electron hits on average were recorded in the tagger for each trigger event. For kinematic calculations, we have to identify which of these electrons radiated the photon that produced the final-state particles detected by the CLAS.

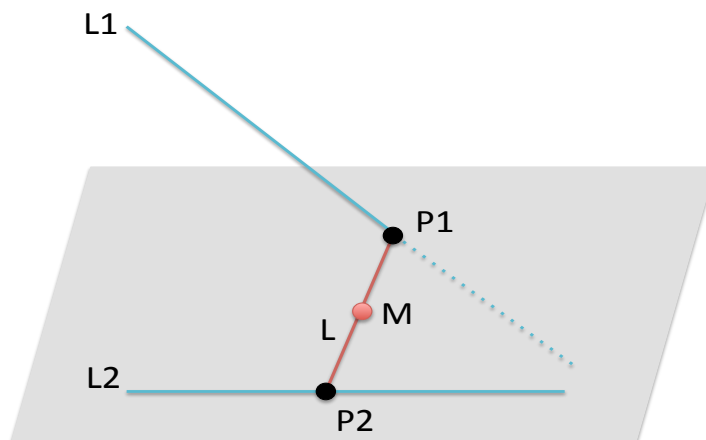


Figure 4.4: Schematic diagram visualizing the DOCA method to determine the vertex position. The straight lines L1 and L2 visualize the γ and the K^+ tracks in the target. In general, the two tracks are not coplanar. L is vertical to both tracks. P1 and P2 are the intersection points between L and L1 and L2, respectively. M is midway between P1 and P2 and represents the location of the reaction vertex.

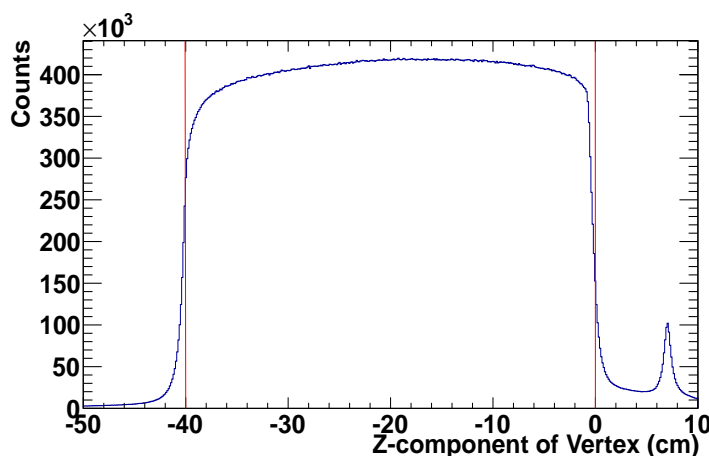


Figure 4.5: Event distribution over the z -component of the reaction vertex. The red lines show the z -vertex range from -40 cm to 0 cm outside of which no events are considered for further analysis. Distances along the z axis are measured relative to the center of the CLAS, which is located at 0 cm. The z -vertex distribution reflects the fact that the center of the target during the g13 experiment was located 20 cm upstream from the center of the CLAS.

The photon identification was done by studying the correlation between the arrival time of the photon at the event vertex, t_γ (determined by tagger timing), and the kaon vertex time, t_ν , calculated using information from the CLAS as indicated in Eq. (4.4). For each event, the difference $\Delta t = t_\nu - t_\gamma$ was then formed as follows

$$\Delta t = t_\nu - t_\gamma = \left(t_{SC} - \frac{d_{SC}}{c\beta_{calc}}\right) - \left(t_{TAGR} + \frac{z + 20}{c}\right), \quad (4.4)$$

where t_{SC} is the time measured by the scintillation counters of the TOF system with respect to the global start time, d_{SC} is the length of the track from the kaon vertex to the TOF paddle, β_{calc} is the particle's speed as a fraction of the speed of light calculated using the measured track's momentum and the nominal mass of the K^+ (see Eq. 4.2), t_{TAGR} is the photon arrival time at the center of the target, and z is the position of the event vertex along the beam axis measured relative to the CLAS center (the 40-cm long target was placed with its center 20 cm upstream of the CLAS center). The Δt distribution of events in our sample is shown in Fig. 4.6. The photon that gives a Δt within the range of -1 ns to 1 ns is selected as the good photon.

For a portion of events, two or more photons with a time coincidence $|\Delta t| < 1$ ns were detected. The additional photons occurred from background hits in the T-counters that happened in the same time window. Figure 4.7 shows that 9.2% of our events contain two photons within the ± 1 -ns coincidence time window. Overall, less than 10% of events contain two or more photons within the ± 1 -ns coincidence range. In order to be able to use these events in our analysis, an additional photo-selection criterion must be implemented. We performed additional studies of the two-photon events in order to evaluate if an appropriate photon-selection procedure can be established. We used two control variables in the studies, the coincident time and the energy of the photon. The latter was used to calculate the mass of the missing state in the $\gamma d \rightarrow K^+ \Lambda X$ reaction (based on 4-momentum conservation, see section 4.4). If one of the two photons is the good photon, it should yield a missing-

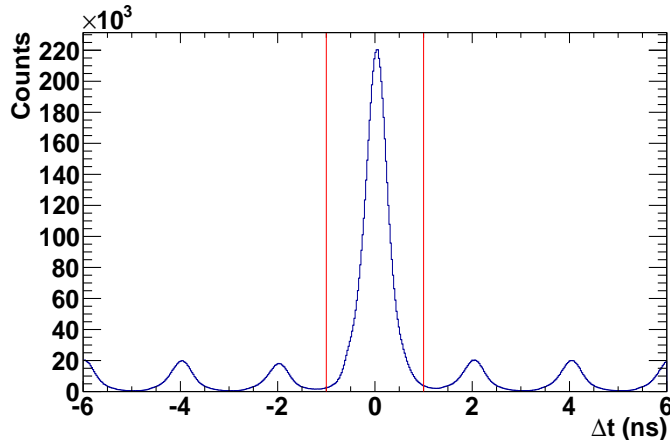


Figure 4.6: Vertex time difference distribution after PID and a narrow IM cut. For each event, only Δt for the photon that is closest in time to the kaon is included in the distribution. One can clearly see the 2.004 ns structure of the electron beam as photons due to electrons from different beam bunches show to be clustered in peaks that are about 2-ns apart. The large peak around Δt of 0 contains photons and kaons that are coincident in time. The red vertical lines show the range of Δt within which we chose the good photon for the event.

state mass, $M_X \equiv MM$, consistent with the nominal neutron mass ($X = n$ for the events of interest from the reaction $\gamma d \rightarrow K^+ \Lambda X$). Event distributions over MM for the photon with the smaller Δt and for the one with the larger Δt are shown in Fig. 4.8.

One can see that the photons with smaller Δt had no advantage relative to the photons with larger Δt , *i.e.* they both produced consistent kinematic distributions. This means that the good photon has randomly smaller or larger Δt and an additional timing criterion cannot be used for photon selection when more than one photon fall within the ± 1 -ns coincidence window. We decided against kinematic selection, based on MM, as this procedure would skew the shape of the background in the MM distribution. Because of these reasons and since the events under question are less than 10% of the full dataset, events with two or more photons were removed from the dataset, and only events with one good photon after the Δt selection were kept for further analysis.

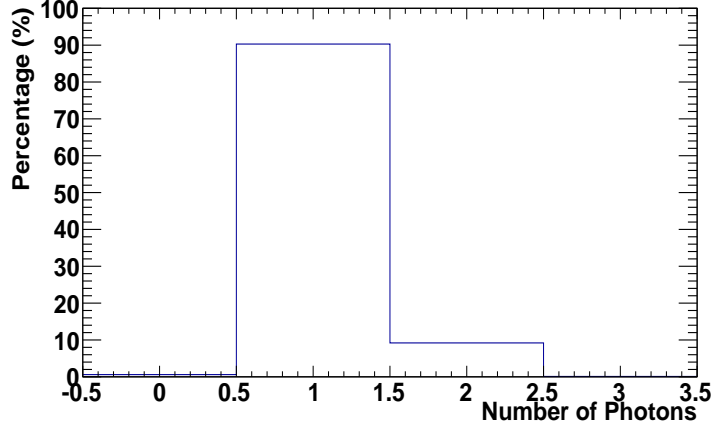


Figure 4.7: Fractions of events with different number of photons within our ± 1 -ns coincidence window (after PID, a narrow IM cut, and the Δt cut). The x -axis shows the number of photons in each event within a coincidence time $|\Delta t| < 1$ ns. The events with two or more photons within ± 1 ns are less than 10% of the full data sample. These events were removed from further analysis.

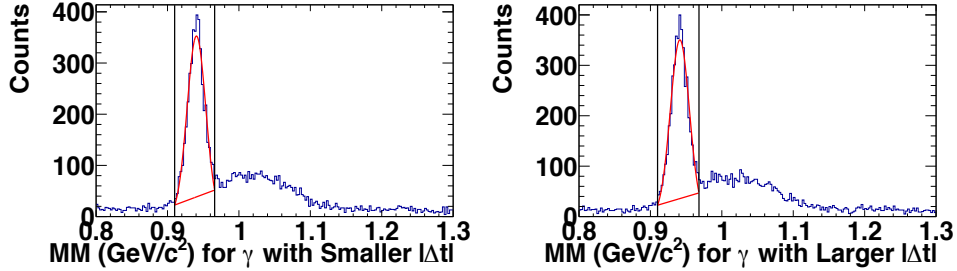


Figure 4.8: Missing-mass distributions of events with two photons giving $|\Delta t| < 1$ ns (50 runs of the g13a dataset were used in this study). The left figure shows MM distribution for photons with the smaller $|\Delta t|$. The right figure shows MM distribution for photons with the larger $|\Delta t|$. The distributions were fit around the neutron peak to Gaussian functions. The black lines show $\pm 3\sigma$ ranges. The areas bound by the red lines contain the events from the reaction of interest. For the photons with smaller $|\Delta t|$, the ratio of signal to the sum of signal and background is approximately 78%. For the photons with larger $|\Delta t|$, the ratio of signal to the sum of signal and background is approximately 76%.

Energy Loss and Momentum Corrections

We applied energy loss and momentum corrections to the detected particles momenta in an attempt to eliminate bias in the reconstructed kinematics of each event. In addition, the corrections brought real experimental distributions in consistency with simulated distributions, which was critical for unbiased estimate of the background in our data sample. The latter allowed to reduce the systematic uncertainties of the background subtraction. The energy loss corrections account for the energy lost by the charged particle via ionization when it passed through the target, beam-line components, and start counter [57]. The momentum corrections account for energy lost by the particles in the gas of the drift chambers, DC misalignments, and differences between the actual toroidal field and the field map used for track reconstruction [58]. A correction to the photon energy was also applied due to a small gravitational sag in the tagger scintillator paddles [59]. Standard CLAS software packages [60] were used to implement all of these corrections in the data analysis presented here.

4.3 ADDITIONAL SELECTION CUTS

Photon Energy Cut

The quasi-free and the Λn FSI mechanisms of interest in this work involve the reaction $\gamma p \rightarrow K^+ \Lambda$ in the first step. This is a threshold reaction, which means that the incoming photon needs to have a minimum energy, $E_{\gamma,threshold}$, in order to be able to initiate the reaction. The threshold energy value can be obtained by using energy conservation in CM and the Lorentz invariance of the Mandelstam variable s

$$\sqrt{s} = \sqrt{p^{*2} + m_{K^+}^2} + \sqrt{p^{*2} + m_{\Lambda}^2} = \sqrt{2E_{\gamma}m_p + m_p^2} = W, \quad (4.5)$$

where s denotes the square of the center-of-mass energy, W denotes the invariant

mass of the initial or the final state, p^* is the magnitude of the CM K^+ or Λ three-momentum, m_{K^+} , m_Λ , and m_p are the nominal masses of the K^+ , Λ , and proton, respectively, and E_γ is the photon beam energy in the lab frame. With $p^* = 0$, the threshold photon energy is given by

$$E_{\gamma,\text{threshold}} = \frac{(m_{K^+} + m_\Lambda)^2 - m_p^2}{2m_p} = 0.911 \text{ GeV}. \quad (4.6)$$

This value, combined with the observed kinematic distributions of the events of interest, led to the removal of all events with photon energy smaller than 0.9 GeV from further analysis.

Invariant-Mass Cut

In the data sample, not all detected proton and π^- pairs originate from a Λ decay. Even when other selection cuts, such as PID, photon selection, and E_γ cuts, were applied, background events were not completely removed as can be seen in Fig. 4.9, which shows the invariant-mass (IM) distribution of p and π^- . The IM is given by

$$IM = \sqrt{(\tilde{p}_p + \tilde{p}_{\pi^-})^2}, \quad (4.7)$$

where \tilde{p}_p and \tilde{p}_{π^-} are the four-momentum vectors of p and π^- , respectively. The distribution exhibits low- and high-invariant-mass tails containing non- Λ events. These events were removed from further analysis by applying a constraint on the allowed invariant mass. Only events yielding invariant mass in the range between 1.11075 GeV/ c^2 and 1.12125 GeV/ c^2 were selected. The cut was defined by using the width of a Gaussian fit to the Λ peak in the IM distribution as shown in Fig. 4.9.

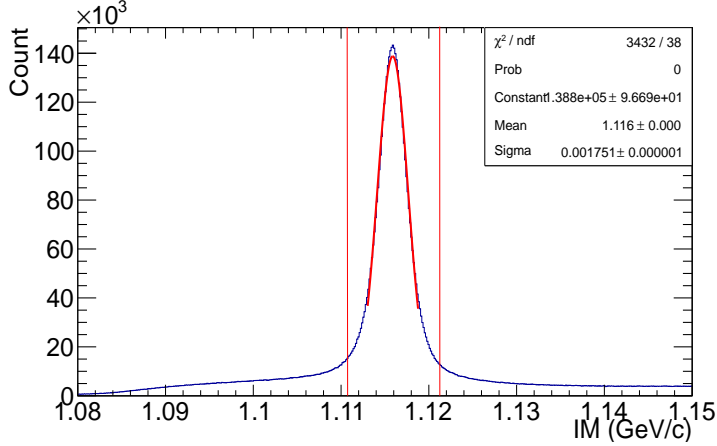


Figure 4.9: Invariant-mass distribution after PID, photon selection, and E_γ cuts. The Λ peak was fitted to a Gaussian and a 3σ cut was applied to select the events where the $p\pi^-$ pair was produced by a Λ decay. The red lines show the cut range.

Missing-Momentum Cut

The $\vec{\gamma}d \rightarrow K^+ \vec{\Lambda} n$ measurement discussed here is fully exclusive, *i.e.* the full kinematics of each initial- and final-state particle is known. This provides a powerful means to separate QF from FSI events in a completely model-independent way. This is a great advantage for Λn scattering studies, compared to inclusive measurements, since the relatively small FSI signal can be identified and isolated from the dominant QF events. Extracting FSI observables should decrease the uncertainties in the model interpretation stemming from the imprecise modeling of the first-step process. Neutrons are spectators in the QF mechanism of the reaction $\vec{\gamma}d \rightarrow K^+ \vec{\Lambda} n$, while neutrons fully participate in the FSI mechanisms. Therefore, the magnitude of the neutron momentum in a QF event should be its Fermi momentum and should be in general smaller than the momentum of a neutron in a FSI event. In the analysis presented here, the final-state neutron momentum is reconstructed using momentum conservation as shown below

$$MP = |\vec{p}_\gamma - (\vec{p}_{K^+} + \vec{p}_p + \vec{p}_{\pi^-})|, \quad (4.8)$$

where \vec{p}_γ , \vec{p}_{K^+} , \vec{p}_p , and \vec{p}_{π^-} are the momentum vectors of γ , K^+ , p , and π^- respectively. The magnitude of the neutron 3-momentum is referred to as missing momentum (MP). We separate QF from FSI events by using the neutron momentum, MP. Events with MP smaller than 0.2 GeV/ c are classified as QF events, while events with MP larger than 0.2 GeV/ c are classified as FSI events. Figure 4.9 shows the experimental MP event distribution of the g13a data sample. The missing-momentum cut is indicated by the solid red line. To evaluate the appropriateness of the value of 0.2 GeV/ c we extracted C_x , C_z , and P_y for the QF mechanism for different MP cut ranges: 0.1 – 0.2 GeV/ c , 0.05 – 0.1 GeV/ c , and 0 – 0.05 GeV/ c . The results with the three different cuts do not exhibit systematic differences, which means the upper limit of 0.2 GeV/ c for the neutron momentum is an adequate choice to select QF events. The details of this study are described in section 7.3. Additionally, we performed a study using simulated data to estimate the amount of QF events with neutron momenta above 0.2 GeV/ c . The results showed that a lower limit of 0.2 GeV/ c was an adequate choice to select FSI events.

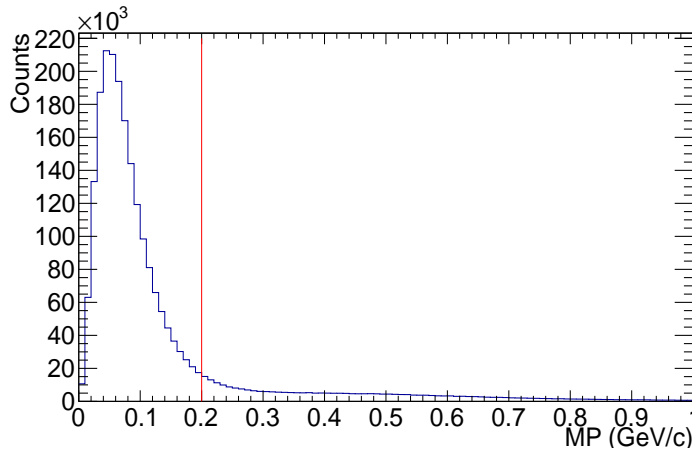


Figure 4.10: Missing-momentum distribution after PID, photon selection, E_γ , and invariant-mass cuts. The red vertical line shows our missing-momentum cut to separate QF and FSI events. To the left of the line, the distribution is dominated by QF events, whereas, to the right of the line the distribution is dominated by FSI events.

4.4 BACKGROUND SUBTRACTION

The mass of the missing state in the $\gamma d \rightarrow K^+ \Lambda X$ reaction, referred to as the missing mass, is defined as

$$MM = \sqrt{((\tilde{p}_\gamma + \tilde{p}_d) - (\tilde{p}_{K^+} + \tilde{p}_p + \tilde{p}_{\pi^-}))^2}, \quad (4.9)$$

where \tilde{p}_γ , \tilde{p}_d , \tilde{p}_{K^+} , \tilde{p}_p , and \tilde{p}_{π^-} are the four-momentum vectors of γ , d , K^+ , p , and π^- , respectively. The MM distribution of the reduced data set (after the application of selections discussed in the previous sections) is shown in Fig. 4.11. For better visualization of the MM patterns, Fig. 4.11 shows the 2-dimensional spectrum of E_γ vs. MM. One can see that in addition to the events of interest, clustered around the nominal neutron mass, there are background events from other physical channels (predominantly Σ and Σ^* production) as well as accidental background events. Since contribution from background can result in false asymmetries, it was important to separate signal events from background events. To this end, a background subtraction method was applied. The critical step in this method was to obtain an independent description of the shape of the MM distributions of the physical and the accidental backgrounds. This was accomplished by a realistic simulation of the reaction dynamics.

Simulation of Reaction Mechanisms and Background

Channels

MM distributions of the physical background were simulated by the use of the Monte Carlo method. Firstly, events from the elementary mechanisms of our reaction and from the background channels were generated using a realistic event generator. The development of the generator is part of the work discussed here. Then, the generated data were processed through the standard CLAS simulation software GSIM and were

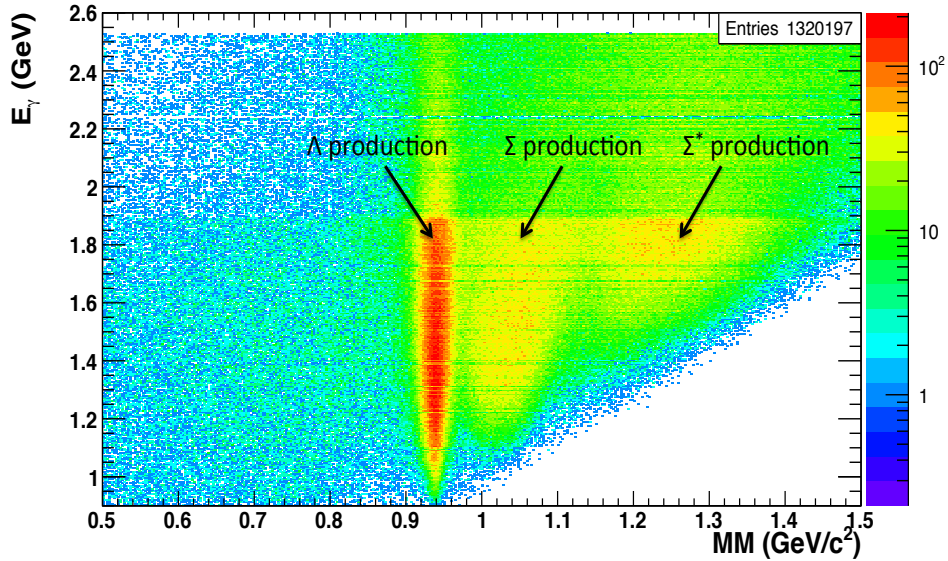


Figure 4.11: E_γ vs. MM distribution after PID, photon selection, E_γ , and IM cuts. One can see the events of interest clustered around the nominal neutron mass (labelled as Λ production) and the physics background events from Σ and Σ^* production. Partial evidence for accidental background can be seen in the existence of low-missing-mass events.

analyzed in exactly the same manner as were the real data. GSIM is a GEANT3-based simulation of the CLAS detector [61].

In the generator, the four main mechanisms of our reaction, including π^0 mediated scattering, π^+ mediated scattering, Kn re-scattering, and Λn re-scattering, as well as three background channels, including Σn re-scattering, Σ^{*0} quasi-free production, and Σ^{*-} quasi-free production were implemented. Table 4.1 lists these 7 physical processes. For the two-step mechanisms, the first-step mechanism was generated first and then one of the final-state particles of that step was used as the beam particle for the generation of the second-step mechanism. The proton and the neutron in the deuteron target were assigned Fermi momentum generated from the Paris potential. Of the two target nucleons, the spectator in the second step was assigned its nominal mass. The mass of the other nucleon was determined so that the sum of the energies of the two nucleons yielded the deuteron rest mass. Decays of Λ , Σ , Σ^{*0} , and Σ^{*-}

Table 4.1: Reaction channels implemented in our realistic event generator.

Channel	Channel Name	First Step	Second Step
1	π^0 mediated for signal	$\gamma n \rightarrow \pi^0 n$	$\pi^0 p \rightarrow K^+ \Lambda$
2	Kn re-scattering for signal	$\gamma p \rightarrow K^+ \Lambda$	$K^+ n \rightarrow K^+ n$
3	Λn re-scattering for signal	$\gamma p \rightarrow K^+ \Lambda$	$\Lambda n \rightarrow \Lambda n$
4	π^+ mediated for signal	$\gamma p \rightarrow \pi^+ n$	$\pi^+ n \rightarrow K^+ \Lambda$
5	Σn re-scattering for Σ production	$\gamma p \rightarrow K^+ \Sigma$	$\Sigma n \rightarrow \Sigma n$
6	Quasi-free for Σ^{*0} production	$\gamma p \rightarrow K^+ \Sigma^{*0}$	$\Sigma^{*0} \rightarrow \Lambda \pi$
7	Quasi-free for Σ^{*-} production	$\gamma n \rightarrow K^+ \Sigma^{*-}$	$\Sigma^{*-} \rightarrow \Lambda \pi^-$

were done in GSIM. Additionally, two extra channels were processed through GSIM and were analyzed, although no extra events were generated. One of the channels is the quasi-free mechanism of our reaction, which shares the final-state particles with the Kn and the Λn rescattering channels. The other channel is the quasi-free Σ production, which shares its final-state particles with the Σn rescattering channel. Cross sections were implemented for some of the channels. The acceptance-rejection method was implemented so that the generated events were distributed according to a cross section.

Figure 4.12 shows the flow chart of the generator. Firstly, the photon beam energy and the Fermi momentum of the target nucleons were generated. Then, a uniformly-distributed random number, called RN1, was used to select the channel to be generated. Several steps were executed after a channel was selected.

- Step 1: Generate the kinematics for the first step of the channel based on a phase-space distribution.
- Step 2: Determine whether unpolarized or polarized cross section is to be used to weight the current event (this is done via a command-line option “p”).
- Step 3: Generate uniformly distributed random number 2 (RN2) and random number 3 (RN3). The range of values of RN2 and RN3 is from 0 to the maximum

differential cross section for the current mechanism (unpolarized for RN2 and polarized for RN3) as determined from cross-section tables. The cross-section tables are based on SAID and Kaon-MAID unpolarized cross sections, as well as polarization observable values obtained in this work.

- Step 4: Calculate the polarized or unpolarized cross section for the current event using its kinematics. Then remove or keep the event by comparing the calculated cross section to the value of RN2 or RN3.
- Step 5: Calculate kinematics for the second step of the channel using a phase-space distribution.

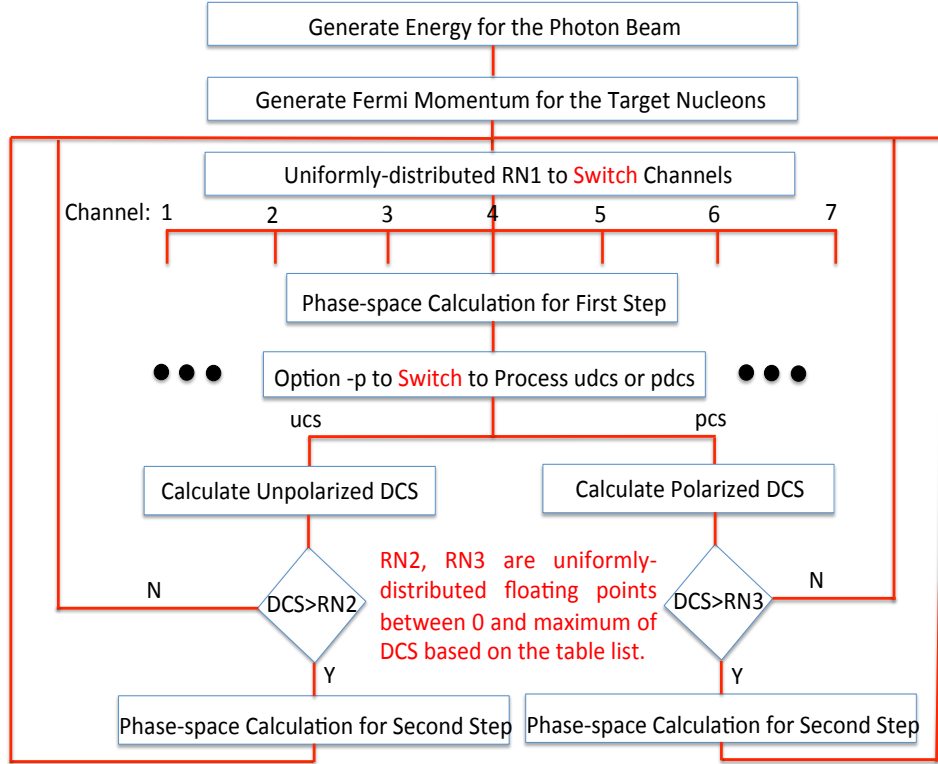


Figure 4.12: Flow chart of the comprehensive event generator used in the simulation of physics backgrounds to the reaction $\vec{\gamma}d \rightarrow K^+ \vec{\Lambda}n$.

The simulated detection environment generated by GSIM does not match exactly the true experimental conditions. We found that the functions of momentum cor-

rections extracted by the experimental data could not be applied to the simulated data. Therefore, functions of momentum corrections specifically for the simulated data were produced by comparing the value of reconstructed particle momentum, p , in the simulated data sample to the true momentum value, p_0 , from the generator (the difference, $\Delta p = p - p_0$ was our control variable). To this end, a simple generator for the reaction $\gamma p \rightarrow K^+ \Lambda$ was produced. After PID cuts and photon selection was applied to the simulated data, we divided the events in bins of the azimuthal angle and the polar angle of K^+ in the lab system as well as of the reaction vertex. Then, Δp vs. p distribution of the events in each bin was plotted for K^+ , p , and π^- . Momentum corrections for each particle type were obtained by fitting the corresponding Δp vs. p distribution to an exponential function defined as

$$f(x) = p_0 e^{p_1 x + p_2} + p_3, \quad (4.10)$$

where p_0 , p_1 , p_2 , and p_3 are free parameters determined by the fit. Figure 4.13 shows an example of the momentum correction for protons. The red solid line shows the momentum correction function. The points on the curve were determined by dividing the momentum range into sub-ranges and fitting the Δp distribution in each sub-range to a Gaussian. The points with the bars on the curve show the mean with 3σ uncertainties for each momentum bin.

Accidental Background

Even though the particle identification selection we use in this work removes a substantial fraction of tracks that are inconsistent with the final state of interest, background from accidental tracks remains in the data sample. The accidental background consists of misidentified particles, *i.e.* particles that were identified to be p , π^- , or K^+ , but had a different true identity.

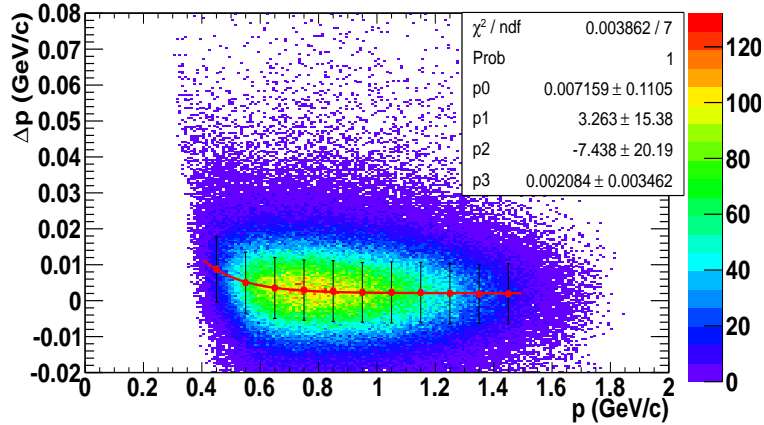


Figure 4.13: An example of momentum correction function (red curve) for the simulated data. The curve is described by an exponential function.

In order to obtain the shape of the accidental background, which is needed in the application of our background subtraction procedure, a study of misidentified p , π^- , or K^+ was performed. For each of these particles, the accidental background was obtained by using the event-mixing technique.

Firstly, we obtained a relatively clean sample of signal events by applying PID, photon selection, IM, and MM cuts. Then, for every event in the clean sample, we replaced the p , π^- , or K^+ with a randomly selected track from a randomly selected another event in the full g13 dataset. We randomly extracted positive particles to replace K^+ or p and negative particles to replace π^- . Finally, the MM for that signal event was recalculated using the four-momenta of the random track and the two good tracks. The MM distributions for particles misidentified as p , π^- , or K^+ are shown in Fig. 4.14 in green, red, and blue, respectively. These distributions were input in the background subtraction procedure as accidental backgrounds.

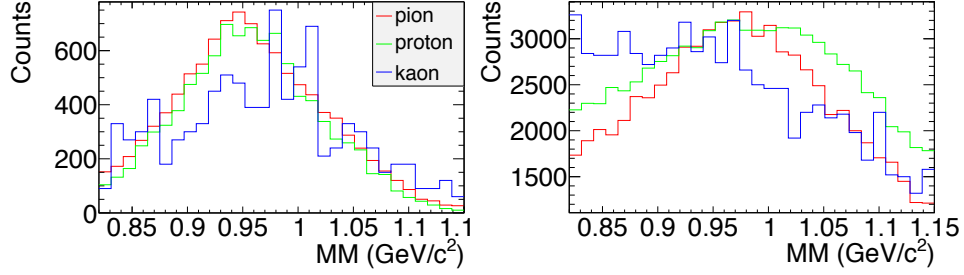


Figure 4.14: Missing-mass distributions of accidental quasi-free (left) and final-state interaction (right) events. The green, red, and blue colors show distributions when the p , π^- , or K^+ good track was substituted with an accidental track. See text for more details.

Background Subtraction Method

After obtaining the MM distributions of the physical and the accidental backgrounds, we fitted the MM distributions of the experimental data for each kinematic bin to the function

$$f(x) = \sum_{i=0}^6 par[i] * hist[i] + Gaus, \quad (4.11)$$

where $hist[0] - hist[3]$ denote the MM distributions of the physical background for the Σn re-scattering channel, the Σ^{*0} quasi-free production channel, the Σ^{*-} quasi-free production channel, and the Σ^0 quasi-free production channel, respectively, for the corresponding kinematic bin of the simulated data. The setup of kinematic bins for the simulated data was the same as for the experimental data. $hist[4] - hist[6]$ denote the MM distributions of the accidental background for particles misidentified as p , π^- , or K^+ , respectively. $p[0] - p[6]$ are free parameters determined by the MM fits. The accidental backgrounds are independent of kinematics, so all kinematic bins have the same accidental background distributions. $Gaus$ is a double Gaussian function, which models the signal. A double Gaussian is used since the signal events, even though they form a symmetric peak around the mean, have long non-Gaussian tails. One of the Gaussians has a small amplitude and a large width and describes

the tails, the other Gaussian has a large amplitude and a smaller width and describes the rest of the peak. Both Gaussian functions have a common mean. Figure 4.15 shows an example of MM fitting for one kinematic bin. After fitting, the signal was obtained as the difference between the initial distribution of all events and the fitted background. The signal was then fitted to a Gaussian function to determine a 3σ range. The reaction yield was obtained as the sum of all the events within the 3σ range of the background-subtracted distribution.

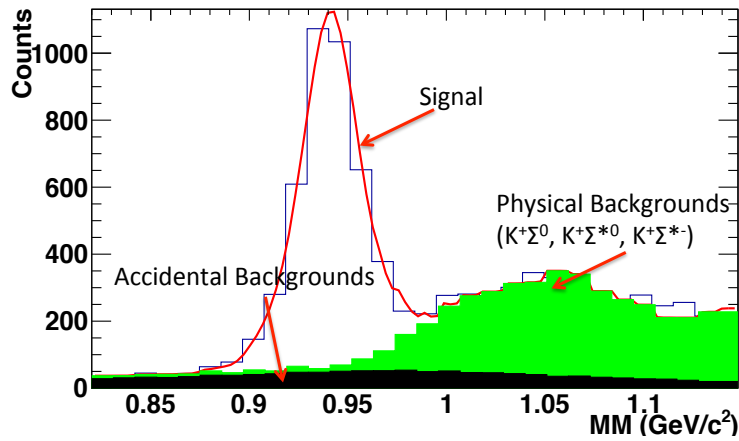


Figure 4.15: An example of MM fitting for one kinematic bin. The red line shows the full fit over the MM range of the histogram, $0.82 \text{ GeV}/c^2 - 1.15 \text{ GeV}/c^2$. The black part shows the accidental background. The green part shows the physical background, which contains the $K^+\Sigma$, $K^+\Sigma^{*0}$, and $K^+\Sigma^{*-}$ channels.

Quality of Missing-Mass Fit

Good fits of the MM distributions are important to ensure that extracted observables are reliable. Thousands of bins were set in this study, and it is impossible to show all fitting plots in this document. The quality of the fits is evaluated by the χ^2 test. During fitting, χ^2/NDF (χ^2 per degree of freedom) was extracted for each bin, and the distribution of these values is shown in Fig. 4.16. Most χ^2/NDF values are between 1 and 2, which indicates that our description of the shape of the MM

distributions is overall good and the fitting had not failed. χ^2/NDF was high for some low-statistic kinematic bins. We removed these bins from further analysis, by requesting a minimum of 50 signal events in a bin, after background subtraction, in order to keep that bin in our data.

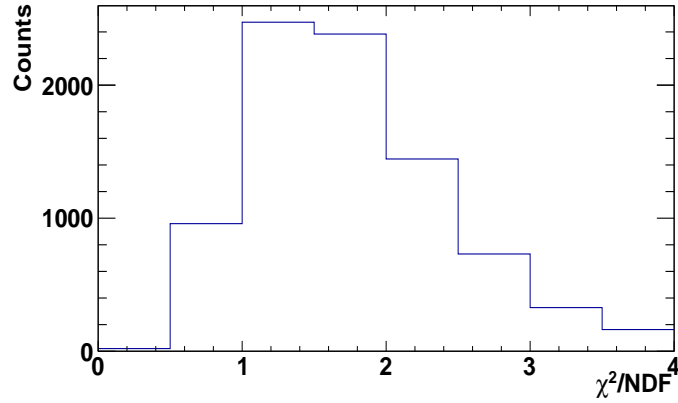


Figure 4.16: Distribution over χ^2 per degree of freedom of the fits to MM histograms. The distribution contains 8800 entries in total. The χ^2 test suggests that the fitting function describes well the MM distribution and that there are no failed fits.

CHAPTER 5

DETERMINATION OF C_x , C_z , AND P_y

5.1 OBSERVABLE-EXTRACTION METHODS

Introduction to Three Different Observable-Extraction Methods

For obtaining optimized results of the polarization observables C_x , C_z , and P_y , different observable-extraction methods were compared. Three different methods can be applied to extract the double polarization observables C_x and C_z . The simplest method, which has been commonly used in CLAS analyses, is a 1-dimensional (1D) fit method. After integrating the polarized differential cross section of Eq. (1.4) over $\cos\theta_y$ and one of $\cos\theta_z$ and $\cos\theta_x$, the beam-helicity asymmetry can be expressed as

$$\begin{aligned}
 Asym(\cos\theta_{x/z}) &= \frac{Y^+ - Y^-}{Y^+ + Y^-} \\
 &= \frac{\int \int \frac{d\sigma^+}{d\Omega} d(\cos\theta_y) d(\cos\theta_{z/x}) - \int \int \frac{d\sigma^-}{d\Omega} d(\cos\theta_y) d(\cos\theta_{z/x})}{\int \int \frac{d\sigma^+}{d\Omega} d(\cos\theta_y) d(\cos\theta_{z/x}) + \int \int \frac{d\sigma^-}{d\Omega} d(\cos\theta_y) d(\cos\theta_{z/x})} \quad (5.1) \\
 &= \alpha P_{circ} C_{x/z} \cos\theta_{x/z},
 \end{aligned}$$

where Y^+ and Y^- denote positive and negative helicity event yields. During the derivation of the 1D fit method, all of formulas are correct under the assumption that the CLAS acceptance is constant over $\cos\theta_y$ and $\cos\theta_z$ or $\cos\theta_y$ and $\cos\theta_x$. This method was used to obtain the previously published CLAS results for C_x and C_z for the reaction $\vec{\gamma}p \rightarrow K^+\vec{\Lambda}$ off the free proton [30]. Similarly, a 2-dimensional fit method (referred to as 2D method here) can be applied to extract C_x and C_z

simultaneously. In the 2D method, the beam-helicity asymmetry is obtained by integrating the differential cross section over $\cos \theta_y$

$$\begin{aligned}
Asym(\cos \theta_x, \cos \theta_z) &= \frac{Y^+ - Y^-}{Y^+ + Y^-} \\
&= \frac{\int \frac{d\sigma^+}{d\Omega} d(\cos \theta_y) - \int \frac{d\sigma^-}{d\Omega} d(\cos \theta_y)}{\int \frac{d\sigma^+}{d\Omega} d(\cos \theta_y) + \int \frac{d\sigma^-}{d\Omega} d(\cos \theta_y)} \\
&= \alpha P_{circ} C_x \cos \theta_x + \alpha P_{circ} C_z \cos \theta_z.
\end{aligned} \tag{5.2}$$

During the derivation of the 2D fit method, all of formulas are correct under the assumption that the CLAS acceptance is constant over $\cos \theta_y$. An event-by-event maximum likelihood (ML) fit method can be used to extract C_x , C_z , and P_y simultaneously. The results reported in this work were obtained with this method. We define the probability density function for the maximum likelihood method as

$$\begin{aligned}
f(\cos \theta_x, \cos \theta_z, \cos \theta_y | C_x, C_z, P_y) &= c(1 \pm \alpha P_{circ} C_x \cos \theta_x \pm \alpha P_{circ} C_z \cos \theta_z \\
&\quad + \alpha P_y \cos \theta_y),
\end{aligned} \tag{5.3}$$

where c represents the unpolarized differential cross section. The total log-likelihood is the product of the log-likelihoods for all individual events

$$\begin{aligned}
\log L &= b + \sum_{i=1}^{n^+} \log[(1 + \alpha P_{circ}^i C_x \cos \theta_x^i + \alpha P_{circ}^i C_z \cos \theta_z^i + \alpha P_y \cos \theta_y^i) w^i] \\
&\quad + \sum_{j=1}^{n^-} \log[(1 - \alpha P_{circ}^j C_x \cos \theta_x^j - \alpha P_{circ}^j C_z \cos \theta_z^j + \alpha P_y \cos \theta_y^j) w^j],
\end{aligned} \tag{5.4}$$

where b is a constant obtained from the unpolarized differential-cross-section term, and is cancelled in the further derivative calculations over C_x , C_z , and P_y since b is independent of them, and w^i or w^j is a weight value of the signal probability for the i^{th} or j^{th} event. Figure 5.1 shows how we determine the weight for each event. After fitting the missing-mass distribution for a given kinematic bin, the number of signal

events is obtained by subtracting the background from the total number of events in the MM histogram. For an event i located in a given missing-mass-histogram bin, we calculate the weight w^i as the ratio of the number of signal events to the number of all events in that MM bin

$$R = \frac{N_{all} - N_{backgrounds}}{N_{all}}. \quad (5.5)$$

All events in the same MM bin are assigned the same weight. Further details, about the determination of the observables of interest using the maximum likelihood method are given in section 5.2.

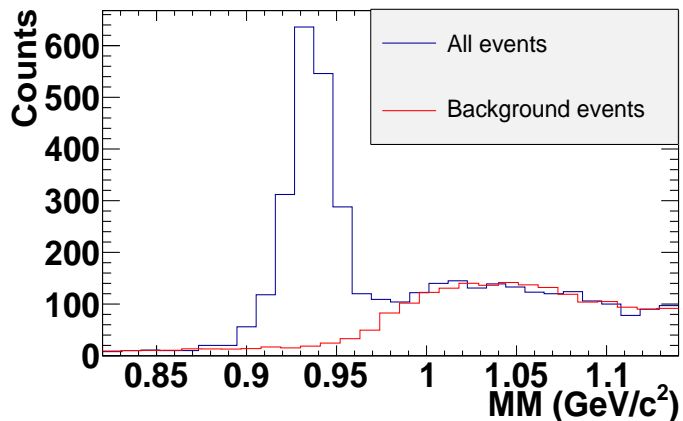


Figure 5.1: Information about the number of background events obtained from MM fitting is used to determine the weight w^i for the i^{th} event in a given kinematic bin. When constructing the corresponding MM histogram (blue histogram), the i^{th} event falls in one of the histogram bins. Background subtraction yields the number of background events in that MM bin (red histogram). The weight w^i is then determined by applying Eq. 5.5. All events in the same MM bin are assigned the same weight.

Analytical Studies of the Observable-Extraction Methods

The three methods, 1D fit, 2D fit, and the maximum likelihood methods were studied analytically in an effort to understand their potential biases. This study was important in order to determine if results obtained with the three methods should

be expected to be consistent with each other and if they can be used for systematic checks.

We consider the 1D method first. According to Eq. (5.1), both distributions of $Asym$ vs. $\cos \theta_x$ and $Asym$ vs. $\cos \theta_z$ should be linear. However, when extracting the observables using the 1D fit method, we found that distributions of $Asym$ vs. $\cos \theta_z$ were indeed linear, while distributions of $Asym$ vs. $\cos \theta_x$ were not linear (see Fig. 5.2). This was true for both the experimental and the simulated data. Throughout further analysis, we realized that the acceptance of the CLAS needed to be considered rather than be cancelled in the calculation of $Asym$ even if the detector performance could not depend on the helicity state of the incident beam. The next step was to understand why the effect of acceptance was much smaller for C_z than for C_x .

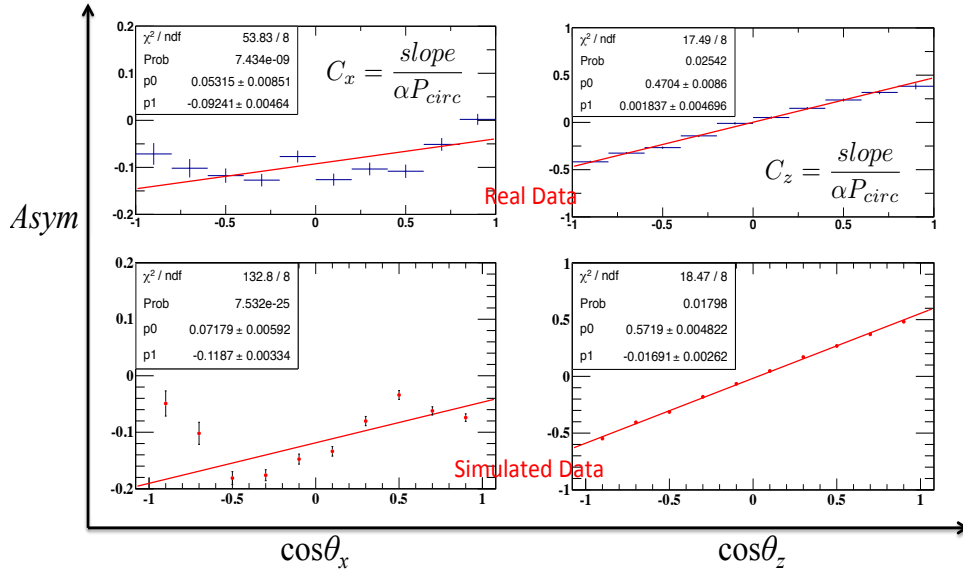


Figure 5.2: Examples of distributions of $Asym$ vs. $\cos \theta_x$ (left column) and $\cos \theta_z$ (right column) from the results for quasi-free events in $\vec{\gamma}d \rightarrow K^+ \vec{\Lambda} n$. The top figures show real experimental data. The bottom distributions show simulated data. The red lines show fits to linear functions.

Firstly, we need to indicate that the direction cosines, $\cos \theta_x$, $\cos \theta_y$, and $\cos \theta_z$, of the three-momentum vector of the decay proton are not independent as they obey the relation

$$\cos^2 \theta_x + \cos^2 \theta_y + \cos^2 \theta_z = 1. \quad (5.6)$$

Therefore, it is not correct to integrate the polarized differential cross section over $\cos \theta_y$ and $\cos \theta_x$, or $\cos \theta_y$ and $\cos \theta_z$, simultaneously. To make a more quantitative statement about the effect of acceptance on each of the double-polarization observables, we proceed as follows. In a spherical coordinate system, $\cos \theta_x$, $\cos \theta_y$, and $\cos \theta_z$ can be expressed in terms of two independent angles, a polar angle θ and an azimuthal angle ϕ ¹

$$\begin{cases} \cos \theta_x = \sin \theta \cos \phi \\ \cos \theta_y = \sin \theta \sin \phi \\ \cos \theta_z = \cos \theta. \end{cases} \quad (5.7)$$

Here, we have set $\theta \equiv \theta_z$. Then, experimental event yields for positive and negative beam helicity can be expressed as

$$Y^\pm(\theta, \phi) = N_\gamma^\pm N_T \sigma^\pm(\theta, \phi) A(\theta, \phi), \quad (5.8)$$

where N_γ^\pm is the number of photons with a positive or negative helicity, N_T is the number of scattering centers in the target, $\sigma^\pm(\theta, \phi)$ represents the polarized differential cross section depending on the independent variables of θ and ϕ , and $A(\theta, \phi)$ is the detector acceptance. For simplicity, we will neglect the momentum dependence of the acceptance within a kinematic bin. Since the beam helicity was flipped very frequently during the experiment, N_γ^+ is equal to N_γ^- . Additionally, N_T is constant. Therefore, we can use a constant c to replace the product $N_\gamma^\pm N_T$. After integrating over ϕ , the event yields can be expressed as

¹Please, note that the angles θ and ϕ here denote some general polar and azimuthal angles, and should not be confused with the measured particle angles in the experiment.

$$Y^\pm(\theta) = c[A(\theta) \pm \alpha P_{circ} C_x \sin \theta A_x(\theta) \pm \alpha P_{circ} C_z \cos \theta A(\theta) + \alpha P_y \sin \theta A_y(\theta)], \quad (5.9)$$

where

$$A(\theta) = \int_0^{2\pi} A(\theta, \phi) d\phi, \quad (5.10)$$

$$A_x(\theta) = \int_0^{2\pi} A(\theta, \phi) \cos \phi d\phi, \quad (5.11)$$

$$A_y(\theta) = \int_0^{2\pi} A(\theta, \phi) \sin \phi d\phi. \quad (5.12)$$

Next, the beam-helicity asymmetry, $Asym$, can be constructed from the event yields with positive and negative helicity as

$$\begin{aligned} Asym &= \frac{Y^+ - Y^-}{Y^+ + Y^-} \\ &= \frac{\alpha P_{circ} C_x \sin \theta A_x(\theta) + \alpha P_{circ} C_z \cos \theta A(\theta)}{A(\theta) + \alpha P_y \sin \theta A_y(\theta)}. \end{aligned} \quad (5.13)$$

Equation (5.13) tells us that $Asym$ does not just depend on C_z and θ , but also depends on C_x and P_y . If the acceptance is constant over ϕ within the kinematic bin, so that A_x and A_y are 0, or if C_x and P_y are 0, then the C_x and P_y terms disappear. In these two cases, $Asym$ as a function of $\cos \theta$ is linear. In reality, nothing guarantees that these conditions are fulfilled, so $Asym$ is generally not a linear function.

However, both real and simulated data yielded distributions of $Asym$ vs. $\cos \theta_z$ that were linear. There are two reasons for this. Firstly, $A_x(\theta)$ and $A_y(\theta)$ can be proved to be much smaller than $A(\theta)$ (see Eq. (5.14) and Eq. (5.15)). Secondly, the actual results of C_x , C_z , and P_y for QF showed that $|C_x|$ was generally much smaller than $|C_z|$, while $|P_y|$ was smaller than $|C_z|$. Thus, the C_x term in Eq. (5.13) is much

smaller than the C_z term, while the $P_y A_y(\theta)$ term is much smaller than the $A(\theta)$ term, which means that the $Asym$ is mostly a linear function of $\cos \theta_z$.

$$\begin{aligned}
A_x(\theta) &= \int_0^{2\pi} A(\theta, \phi) \cos \phi d\phi \\
&< \int_0^{2\pi} A(\theta, \phi) |\cos \phi| d\phi \\
&< |\cos \phi|_{max} \int_0^{2\pi} A(\theta, \phi) d\phi \\
&= \int_0^{2\pi} A(\theta, \phi) d\phi \\
&= A(\theta),
\end{aligned} \tag{5.14}$$

$$\begin{aligned}
A_y(\theta) &= \int_0^{2\pi} A(\theta, \phi) \sin \phi d\phi \\
&< \int_0^{2\pi} A(\theta, \phi) |\sin \phi| d\phi \\
&< |\sin \phi|_{max} \int_0^{2\pi} A(\theta, \phi) d\phi \\
&= \int_0^{2\pi} A(\theta, \phi) d\phi \\
&= A(\theta).
\end{aligned} \tag{5.15}$$

For the convenience of discussing C_x , we define another spherical coordinate system (see Eq. (5.16)). Similar to the case of C_z , $Asym$ can be expressed by Eq. (5.17). However, in this case the C_z and P_y terms in Eq. (5.17) do not disappear because generally $|C_x|$ is smaller than $|C_z|$ and $|P_y|$.

$$\begin{cases} \cos \theta_x = \cos \theta \\ \cos \theta_y = \sin \theta \cos \phi \\ \cos \theta_z = \sin \theta \sin \phi. \end{cases} \tag{5.16}$$

$$\begin{aligned}
Asym &= \frac{Y^+ - Y^-}{Y^+ + Y^-} \\
&= \frac{\alpha P_{circ} C_x \cos \theta A(\theta) + \alpha P_{circ} C_z \sin \theta A_z(\theta)}{A(\theta) + \alpha P_y \sin \theta A_y(\theta)},
\end{aligned} \tag{5.17}$$

where,

$$A_z(\theta) = \int_0^{2\pi} A(\theta, \phi) \sin \phi d\phi, \quad (5.18)$$

$$A_y(\theta) = \int_0^{2\pi} A(\theta, \phi) \cos \phi d\phi. \quad (5.19)$$

In conclusion, the effect of detector acceptance cannot be ignored in the 1D fit method, especially for C_x . The acceptance effect on P_y should be somewhere between the effect on C_x and C_z , when P_y is extracted by a 1D fit method. The 2D fit can reduce the effect of acceptance to some extent because the acceptance is approximately fixed, *i.e.* it is constant over a bin, when the experimental data is binned in two angles. The maximum likelihood method is the most efficient way to reduce the effect of acceptance since it is an event-by-event method.

Statistical Studies of the Observable-Extraction Methods

To quantify any potential biases in each method, we performed studies with simulated data. The idea is to generate a large number, N , of experiments with each experiment yielding one set of estimates for C_x , C_z , and P_y . This will produce samples of N estimates for C_x , C_z , and P_y , respectively. We will use the mean of each sample as an estimate of the total bias in the method. The standard deviation of the sample yields the statistical uncertainty of each outcome in the sample. The latter is important for the maximum likelihood method where we need an independent estimate of the statistical uncertainty of each C_x , C_z , and P_y .

We setup a generator to generate events distributed according to the polarized cross section of the reaction $\vec{\gamma} p \rightarrow K^+ \vec{\Lambda}$. During the generation, we ensured that the number of events with positive and negative beam helicities were the same. Then, we randomly produced values of the polarization observables C_x , C_z , and P_y in reasonable ranges derived from the experiment (C_x : $[0, 0.15]$, C_z : $[0.5, 1]$, and P_y : $[-0.4, 0]$),

and input these values into the polarized differential cross section. Next, we let the generated data pass through the detector simulation and analyzed them as we did real data. Then, the helicity dependent observables C_x and C_z were extracted using the three different methods described earlier, while the helicity independent observable P_y was extracted only using the maximum likelihood method. Totally, we generated 6000 experiments, with 1 million events in each experiment, *i.e.*, we obtained 6000 estimates for C_x , C_z , and P_y . Figure 5.3 shows distributions of the differences between the 6000 extracted values with the fitting methods and the values put in the generator (true values) for C_x and C_z , separately. Table 5.1 lists the means and the standard deviations of the means of the difference distributions. One can see that of all the methods the 1D fit method is biased the most. The estimate of C_x is about 261 standard deviations from zero. C_z has a smaller but still significant bias that is about 22 standard deviations from zero. The biases in the 2D fit method are about 20 standard deviations from zero (for C_x) and about 30 standard deviations from zero (for C_z). For both observables, the bias of the maximum likelihood method is an order of magnitude smaller than that of the 2D fit. For C_x the bias is about 10 standard deviations from zero, while for C_z it is about 6 standard deviations from zero. This residual bias can be explained by the fact that an unnormalized probability density function (PDF) was used in the fits. In a normalized PDF the normalization constant would depend on the polarization observables, due to the non-constant detector acceptance. The biases of the observables estimated via the ML method will be reported as systematic uncertainties. We choose to rather not correct the observables for the bias due to the uncertainties of the CLAS acceptance.

The results of the simulated studies are consistent with the conclusions of the analytical studies. Our overall conclusion is that the 1D fit method is biased due to the effect of the acceptance. The bias is especially large for C_x and cannot be neglected. Biases can be significantly reduced if the observables are extracted by

Table 5.1: Means and standard deviations of the means of distributions over the differences between C_x and C_z values extracted by the different fitting methods and the true values of C_x and C_z .

Fitting Method	$\overline{\Delta C_x} \pm \sigma_{\overline{\Delta C_x}}$	$\overline{\Delta C_z} \pm \sigma_{\overline{\Delta C_z}}$	$\overline{\Delta P_y} \pm \sigma_{\overline{\Delta P_y}}$
1D	0.14085 ± 0.00054	-0.01108 ± 0.00050	—
2D	0.01030 ± 0.00052	-0.01647 ± 0.00051	—
Maximum Likelihood	0.00486 ± 0.00048	-0.00261 ± 0.00046	0.00803 ± 0.00043

the maximum likelihood method. All of our final results were extracted by the ML method.

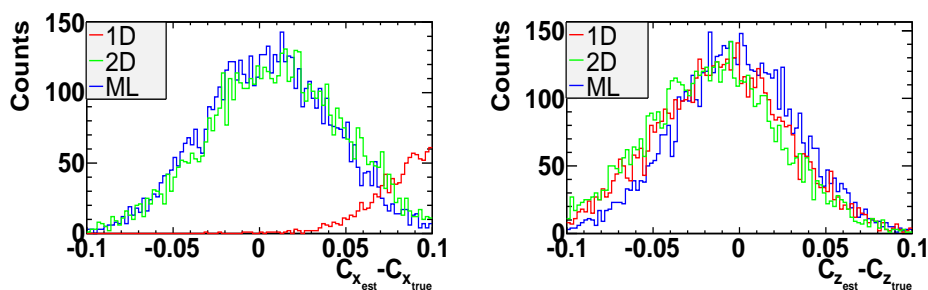


Figure 5.3: Differences between the extracted and true values for C_x (left) and C_z (right). The red lines show difference distributions with estimates from the 1D method, the green lines show difference distributions with estimates from the 2D fit method, and the blue lines are difference distributions with estimates from the maximum likelihood method.

To prove that the observed biases of the observable-extraction methods were indeed caused by the CLAS acceptance, we compared estimates of C_x , C_z , and P_y obtained by the three methods from analysis of simulated data affected and not affected by the CLAS acceptance. The estimates from data affected by the CLAS acceptance were taken from the study described above. To obtain estimates from data not affected by the CLAS acceptance, we generated the data using the same generator as described above, but did not let the generated data pass through the detector simulation, rather we directly extracted the observables using the three different methods. Combining both sets of estimates, we obtained the biases of the

observable-extraction methods due only to detector acceptance. The comparison is shown in Fig. 5.4. Biases are negligible for the case of ideal (constant) acceptance. However, when the data are subjected to the CLAS acceptance, the estimates of the observables are biased and the different methods cause different amounts of bias.

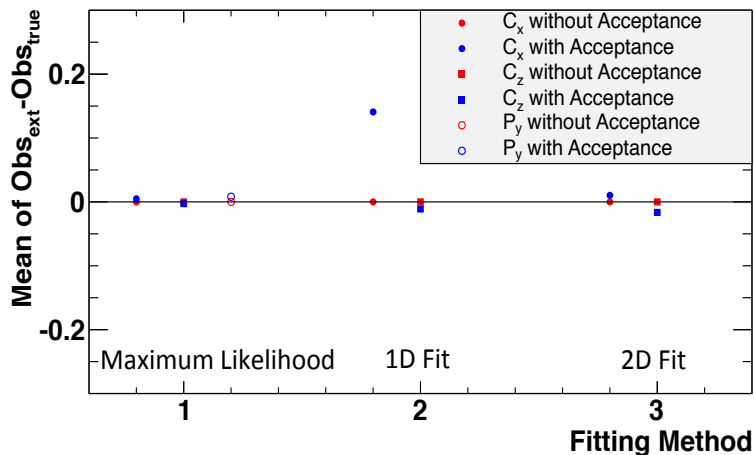


Figure 5.4: Means of differences between 6000 extracted values and true values with and without consideration of the CLAS acceptance for C_x (solid circles), C_z (solid squares), and P_y (open circles). The red color is used for estimates without consideration of the acceptance, while the blue color is used for estimates with consideration of the acceptance. The black horizontal line shows the y -value of zero.

5.2 STATISTICAL UNCERTAINTIES OF C_x , C_z , AND P_y

Our estimates of C_x , C_z , and P_y for each kinematic bin are obtained as a set of parameters that maximizes the total log-likelihood function described in Eq. (5.4). Since the function is complicated, analytical solutions of the estimates cannot be obtained. Therefore, the fit was done numerically, by the use of the software analysis package ROOT [62]. In the software, we set the log-likelihood function as

$$\begin{aligned}
 \log L = & - \sum_{i=1}^{n^+} \log[(1 + p_1 \cos \theta_x^i + p_2 \cos \theta_z^i + p_3 \cos \theta_y^i) w^i] \\
 & - \sum_{j=1}^{n^-} \log[(1 - p_1 \cos \theta_x^j - p_2 \cos \theta_z^j + p_3 \cos \theta_y^j) w^j],
 \end{aligned} \tag{5.20}$$

where p_1 represents αC_x , p_2 represents αC_z , and p_3 represents αP_y . The ROOT class “TFitterMinuit” [63] was applied to find a set of values of p_1 , p_2 , and p_3 that maximizes Eq. (5.20). From the solutions p_1 , p_2 , and p_3 , the observables are obtained as

$$\begin{cases} C_x = \frac{p_1}{\alpha} \\ C_z = \frac{p_2}{\alpha} \\ P_y = \frac{p_3}{\alpha}. \end{cases} \quad (5.21)$$

The statistical uncertainties of the observables should reflect the counting statistics in the $K^+\Lambda n$ FSI event yields. Thus, the statistical uncertainties of the observables are obtained by propagating the statistical uncertainties of p_1 , p_2 , and p_3 as follows

$$\begin{cases} \sigma_{C_x} = \frac{\sigma_{p_1}}{\alpha} \\ \sigma_{C_z} = \frac{\sigma_{p_2}}{\alpha} \\ \sigma_{P_y} = \frac{\sigma_{p_3}}{\alpha}, \end{cases} \quad (5.22)$$

where σ_{p_1} , σ_{p_2} , and σ_{p_3} are the statistical uncertainties of the fit parameters returned by “TFitterMinuit”.

To test that the statistical uncertainties of the C_x , C_z , and P_y extracted from the maximum likelihood method are reasonable, a study using simulated data was performed. The same generator used in the study described in section 5.1 was applied to generate events. Then, C_x , C_z , and P_y were extracted by the maximum likelihood method. Totally, 12 sets of experiments were implemented, and each set included 6000 experiments. The number of experimental events for each set was 40, 80, 100, 400, 700, 1K, 3K, 10K, 100K, 400K, 700K, and 1M.

For each set of experiments, a distribution of the differences between the 6000 extracted values and the true values of C_x , C_z , and P_y (see Figures 5.5, 5.6, and 5.7) was constructed and fitted to a Gaussian function. The standard deviation of each

distribution is an estimate of the statistical uncertainty of each outcome in the sample and this is the value we compared to the statistical uncertainty obtained from the ML fits. Figures 5.5, 5.6, and 5.7 show that the difference distributions were Gaussian distributions except for the first experimental set due to the low statistics in each experiment. Therefore, we excluded this set from further analysis. To determine the dependence of the statistical uncertainty of one estimate on the number of events in the experiment, we plotted the standard deviation as a function of the number of events in an experiment. This was done individually for C_x , C_z , and P_y (see Fig. 5.8). The correlations were then fitted to exponentials

$$f(x) = [0]x^{-[1]} + [2], \quad (5.23)$$

where $[0]$, $[1]$, and $[2]$ are free parameters determined from the fits.

The fit parameters of the exponentials describing the statistical uncertainties of C_x , C_z , and P_y , are shown in Fig. 5.8 top, middle, and bottom, respectively. Then, for an experiment where C_x , C_z , and P_y are determined from a sample with a number of events x , the statistical uncertainty, σ_{std} , of each observable can be obtained by using Eq. (5.23). Relative differences $(\sigma_{est} - \sigma_{std})/\sigma_{std}$ for each set of simulated experiments were calculated and are shown in Fig. 5.9. The relative differences are close to zero, especially when the number of sample events is between a hundred and a few thousand. Statistics for kinematic bins of the real data is located in this range. Thus, the statistical uncertainties for C_x , C_z , and P_y extracted by the maximum likelihood method are reliable and the data in this work are reported with these uncertainties.

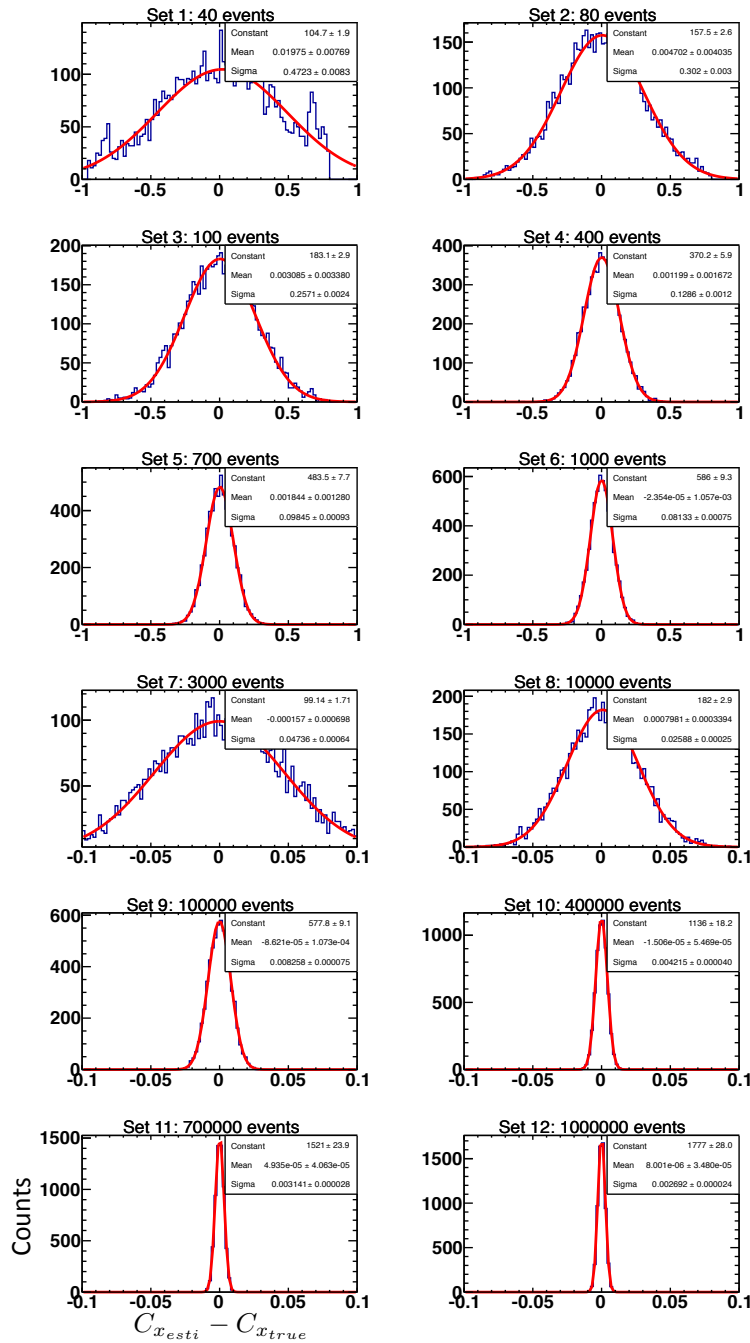


Figure 5.5: 12 difference distributions between the values extracted by the maximum likelihood method and the true values for C_x . The red lines show fits to Gaussian functions.

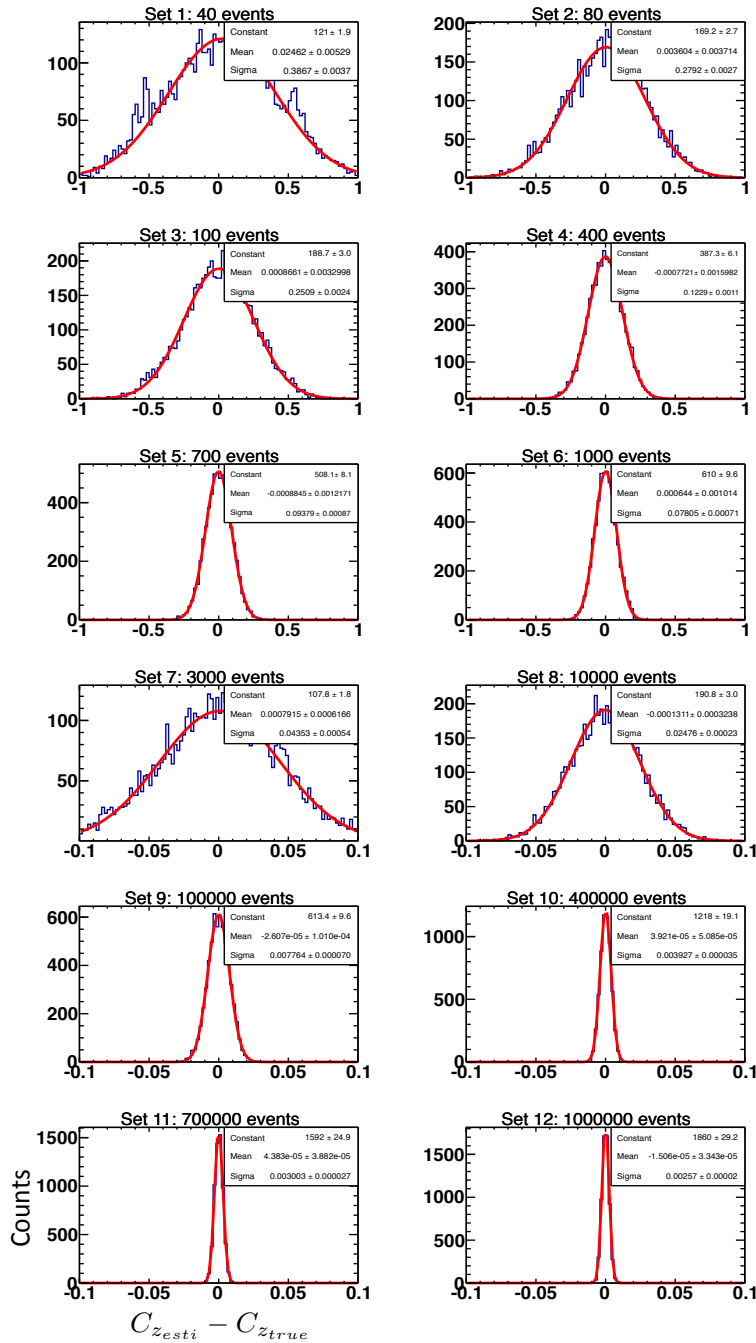


Figure 5.6: 12 difference distributions between the values extracted by the maximum likelihood method and the true values for C_z . The red lines show fits to Gaussian functions.

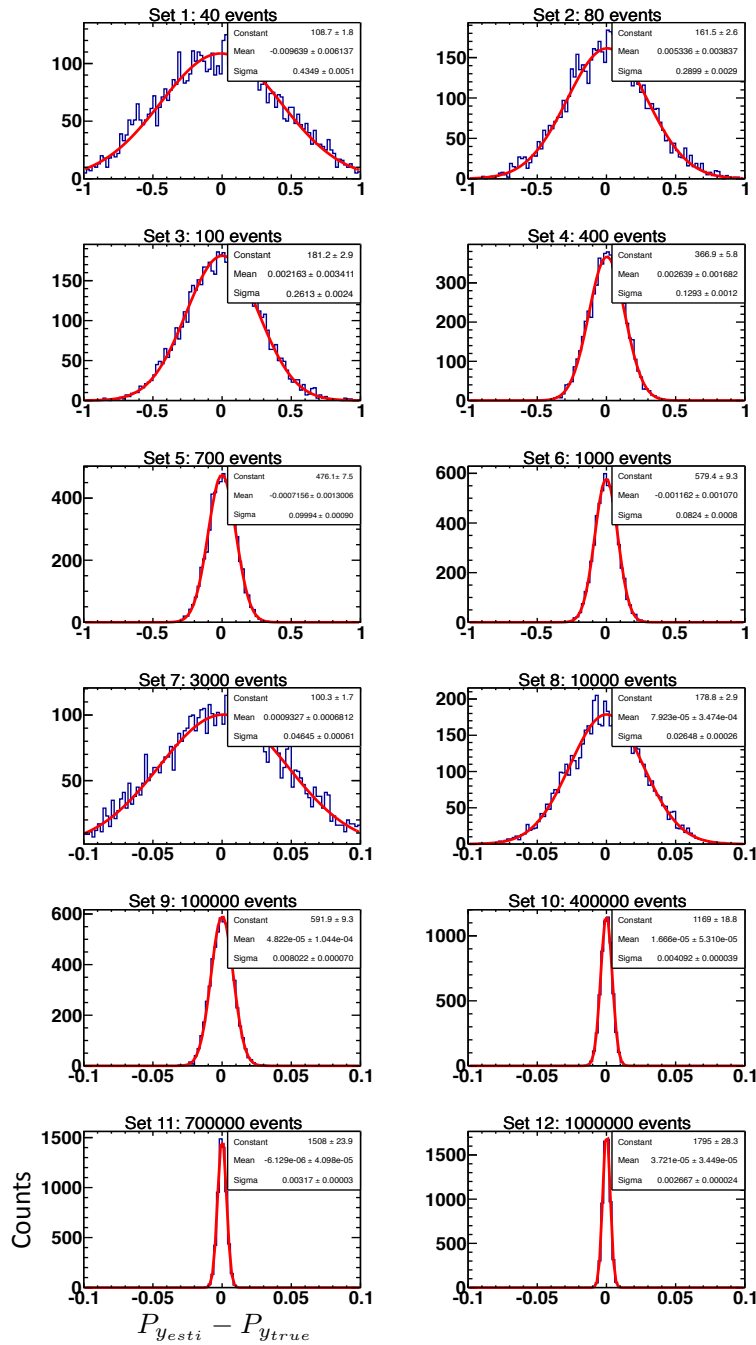


Figure 5.7: 12 difference distributions between the values extracted by the maximum likelihood method and the true values for P_y . The red lines show fits to Gaussian functions.

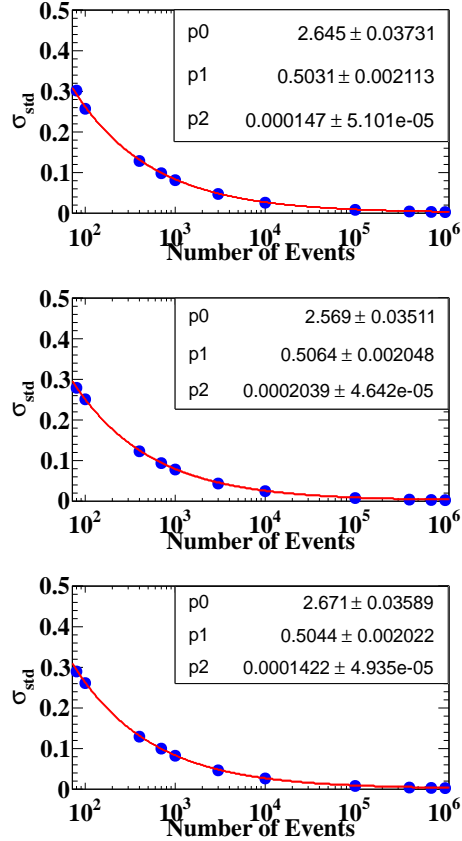


Figure 5.8: Dependence of the statistical uncertainty, σ_{std} , of C_x (top), C_z (middle), and P_y (bottom) on the number of sample events. The values of σ_{std} are the standard deviations of distributions of 6000 observable estimates, which were obtained from simulated experiments (see text). The red curves show exponential fits.

5.3 DETERMINATION OF C_x , C_z , AND P_y FOR THE QUASI-FREE MECHANISM

Axis Convention

For the QF mechanism of $\vec{\gamma}d \rightarrow K^+\vec{\Lambda}n$, the neutron bound in the deuteron is a spectator, so the reaction can be simplified into $\vec{\gamma}p \rightarrow K^+\vec{\Lambda}$. Figure 5.10 shows the axis convention of this reaction, which is defined in center-of-mass system (CMS). The reaction takes place in a single plane, also called the production plane, defined by the photon and K^+ momenta. The z -axis points in the direction of the incoming photon. The y -axis is in the direction of the vector product of the photon and the K^+

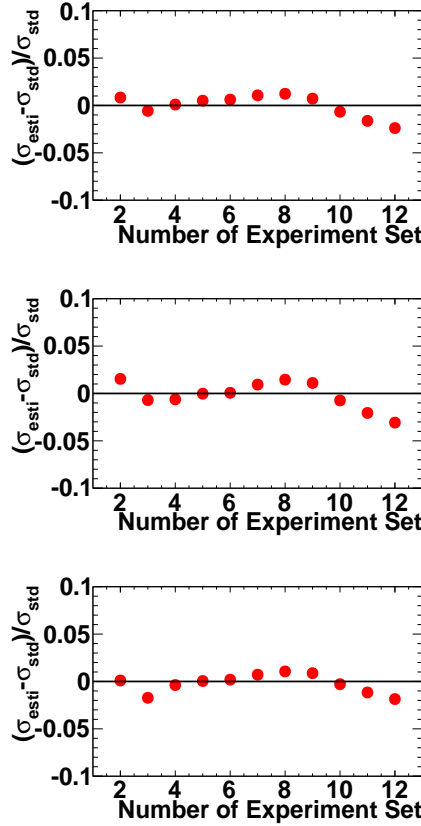


Figure 5.9: Relative differences between the statistical uncertainties of C_x (top), C_z (middle), and P_y (bottom) obtained from TFitterMinuit and from a large number of experiments (see text for more detail). The number of experiment set on the x -axis corresponds to different number of sample events as shown on Figures 5.5, 5.6, and 5.7. The black lines are drawn to show visually the y -value of zero.

CM momenta. The x -axis complements z and y to a right-handed reference frame. In Fig. 5.10, θ_{KCM} is the angle between the γ and K^+ momenta. θ_x , θ_y , and θ_z , which are defined in the Λ rest frame, denote directions of the momentum vector of the decay proton in the xyz system. Axis conventions, which are not unique, are important for the extraction of C_x , C_z , and P_y . The axis convention we adopted was suggested in [64] and is the same as the convention used for the previously published CLAS results on $\vec{\gamma}p \rightarrow K^+ \vec{\Lambda}$ from the g1c experiment [30, 35]. This will enable us to compare our results to the published results.

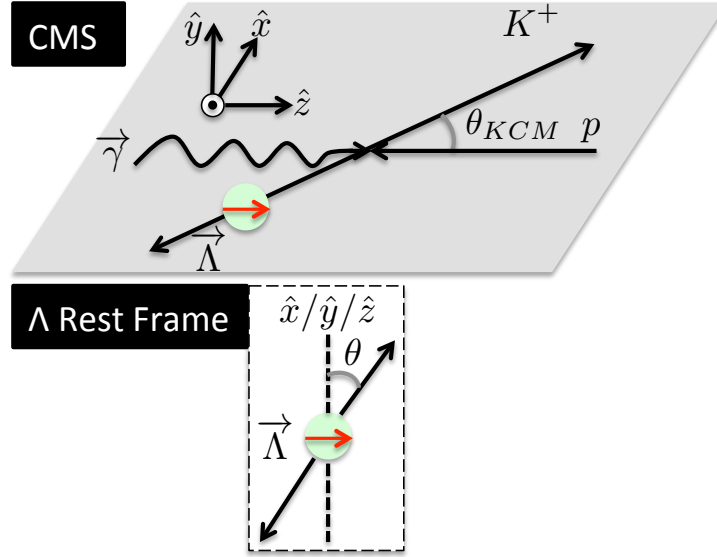


Figure 5.10: Definition of coordinate system for the determination of the observables C_x , C_z , and P_y for quasi-free $K^+\Lambda$ photoproduction off the bound proton. The observables are reported in bins of E_γ and the kaon polar angle in CM, θ_{KCM} .

Kinematic Bins

For the extraction of the polarization observables for the QF mechanism, data were binned in two layers. The first layer contains two independent kinematical variables describing the reaction $\vec{\gamma}p \rightarrow K^+\vec{\Lambda}$, E_γ and $\cos\theta_{KCM}$. The second layer contains two variables that characterize the Λ decay, $\cos\theta_x$ and $\cos\theta_z$. Additionally, the data were binned in photon helicity. For each bin in E_γ and $\cos\theta_{KCM}$, data were binned in $\cos\theta_x$, $\cos\theta_z$, and photon helicity.

During the extraction of C_x , C_z , and P_y , firstly we binned the QF data as described above, and then for each bin we performed background subtraction using the MM distribution for that bin. This procedure allowed us to determine the weight of each event in the data sample. Secondly, $\cos\theta_x$, $\cos\theta_y$, $\cos\theta_z$, and the weight of each event were input into the PDF of the maximum likelihood method (see Eq. (5.4)) according to the photon helicity for that event. After inputting all events for a given kinematic bin, C_x , C_z , and P_y were extracted. Our QF results of C_x , C_z , and P_y are then

reported in bins of E_γ and $\cos\theta_{KCM}$.

The bin width is important for the extraction of observables due to the statistical limitation of the dataset. The common idea would be to set the same width for each bin. However, that would lead to statistics in some bins that is too low to implement the background subtraction method. To avoid this situation, a technique was applied to make all E_γ and $\cos\theta_{KCM}$ bins have similar statistics. Figure 5.11 shows the setup of bins for fixed E_γ , while Fig. 5.12 shows the setup of bins for fixed $\cos\theta_{KCM}$. The data were binned in 16 bins in E_γ and in 10 bins in $\cos\theta_{KCM}$. Additionally, the ranges of $\cos\theta_x$ and $\cos\theta_z$ are both from -1 to 1 , and the bin width for these variables is 0.5 . With 2560 bins for each photon helicity, the total number of bins is thus 5120. Background subtraction using the MM distributions (see section 4.4) was applied for each of these bins.

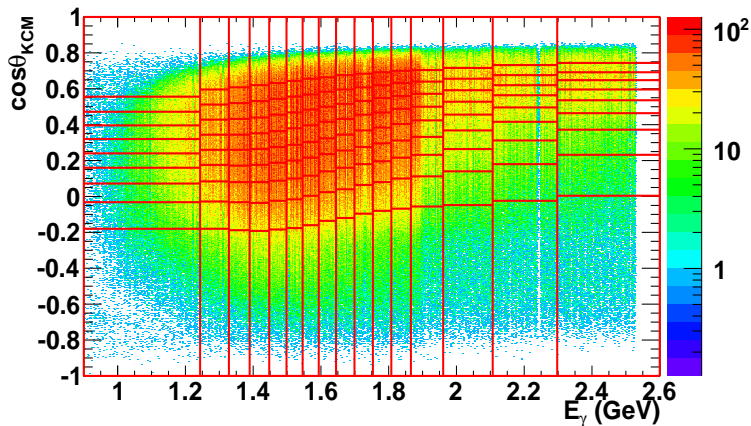


Figure 5.11: Choice of kinematic binning for the extraction of C_x , C_z , and P_y for the quasi-free mechanism of the reaction $\vec{\gamma}d \rightarrow K^+ \vec{\Lambda} n$. The bin widths are chosen so that the bins contain similar number of events. Each red box corresponds to one bin. This binning allows to obtain the observables as a function of $\cos\theta_{KCM}$ for fixed E_γ . One can also see the CLAS angular and energy coverage for that mechanism. The data cover $\cos\theta_{KCM}$ range from -0.9 to 0.8 and photon energy range from 0.9 GeV to 2.54 GeV.

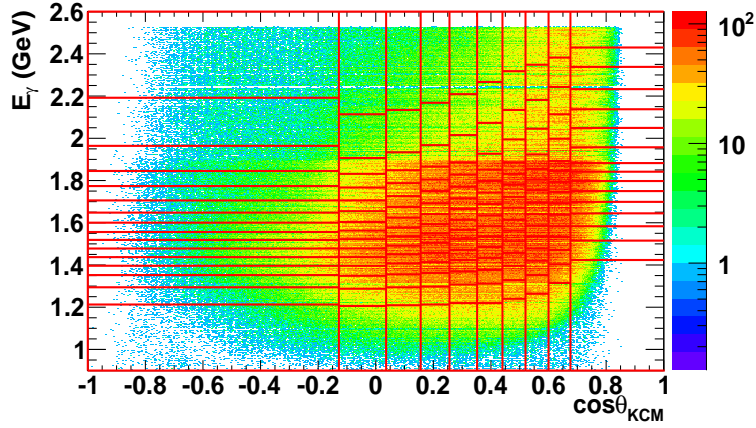


Figure 5.12: Choice of kinematic binning for the extraction of C_x , C_z , and P_y for the quasi-free mechanism of the reaction $\vec{\gamma}d \rightarrow K^+ \vec{\Lambda} n$. The bin widths are chosen so that the bins contain similar number of events. Each red box corresponds to one bin. This binning allows to obtain the observables as a function of E_γ for fixed $\cos \theta_{KCM}$.

Results

Figures 5.13, 5.14, and 5.15 show the quasi-free-mechanism C_x , C_z , and P_y as functions of $\cos \theta_{KCM}$ for fixed E_γ , respectively. The results suggest that:

- Generally, C_x is independent of $\cos \theta_{KCM}$ at low E_γ , and the variations of C_x become larger as E_γ increases.
- C_z is close to 1 and is independent of $\cos \theta_{KCM}$ at lower E_γ . However, at higher E_γ , C_z has a lower value at low $\cos \theta_{KCM}$, and it generally increases from this lower value to 1 as $\cos \theta_{KCM}$ increases.
- P_y decreases as $\cos \theta_{KCM}$ increases except for some points at high E_γ and low $\cos \theta_{KCM}$.

Figures 5.16, 5.17, and 5.18 show C_x , C_z , and P_y as a function of E_γ at fixed $\cos \theta_{KCM}$ bins. The results suggest that:

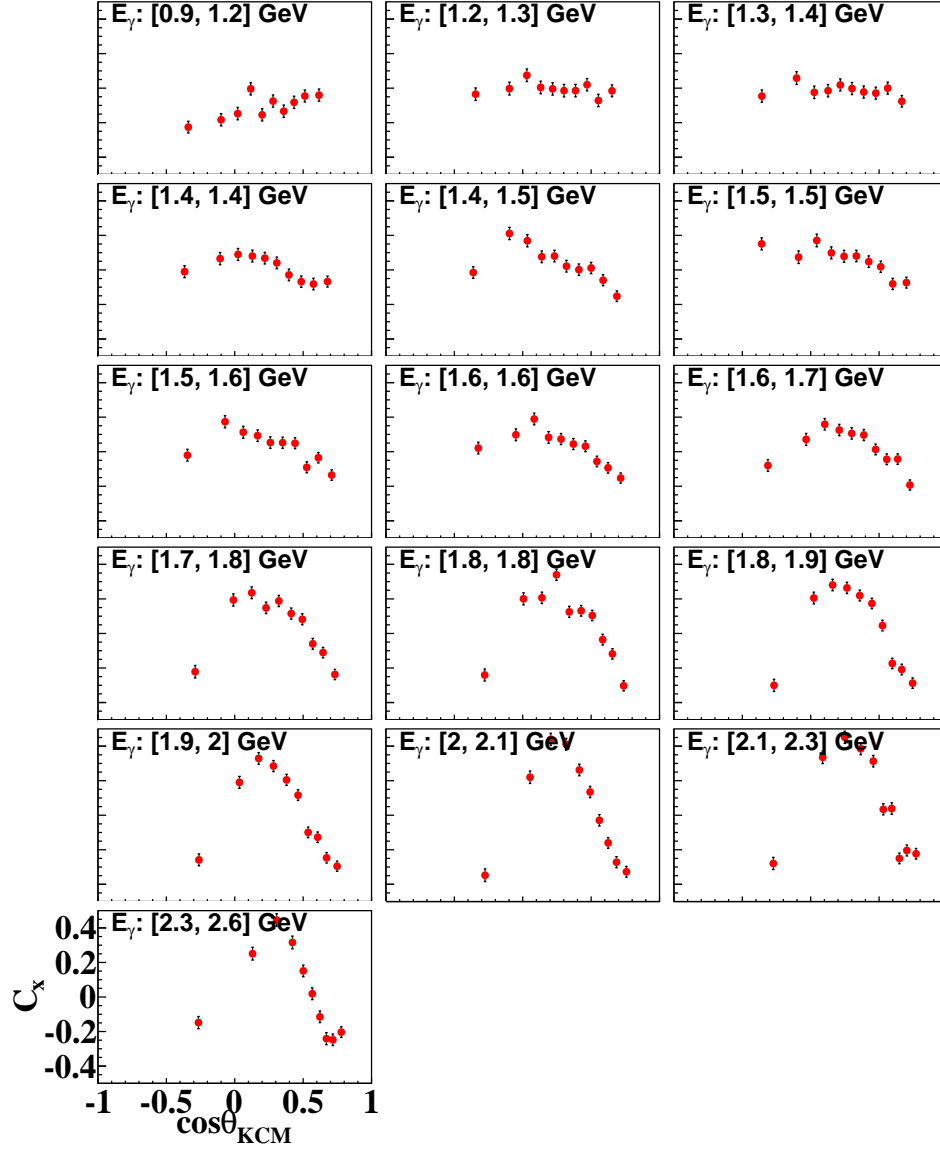


Figure 5.13: C_x as a function of $\cos\theta_{KCM}$ at fixed E_γ for the quasi-free mechanism of the reaction $\vec{\gamma}d \rightarrow K^+\vec{\Lambda}n$. The $\cos\theta_{KCM}$ values at which our results for C_x are reported, are the averages of the $\cos\theta_{KCM}$ values of all the events in the corresponding E_γ and $\cos\theta_{KCM}$ bins.

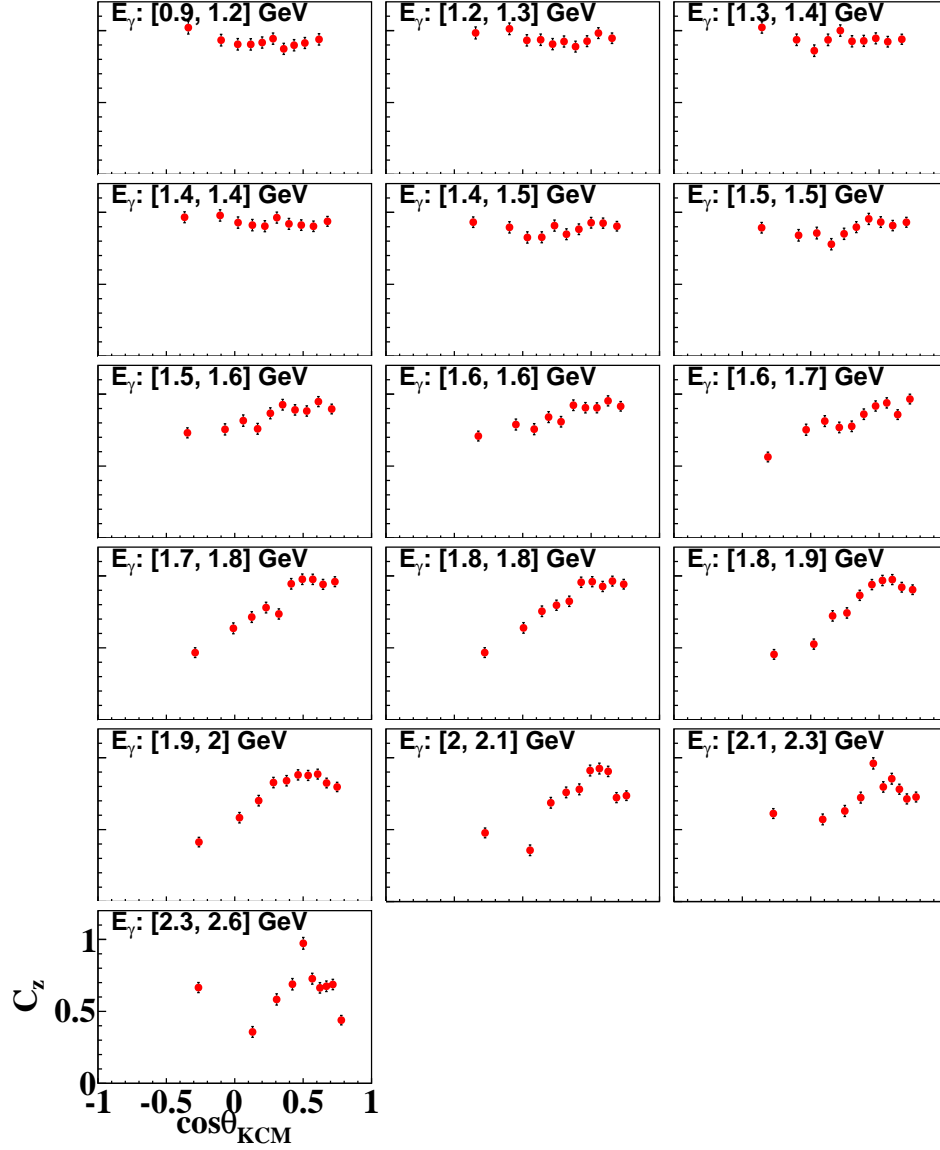


Figure 5.14: C_z as a function of $\cos\theta_{KCM}$ at fixed E_γ for the quasi-free mechanism of the reaction $\vec{\gamma}d \rightarrow K^+\vec{\Lambda}n$. The $\cos\theta_{KCM}$ values at which our results for C_z are reported, are the averages of the $\cos\theta_{KCM}$ values of all the events in the corresponding E_γ and $\cos\theta_{KCM}$ bins.

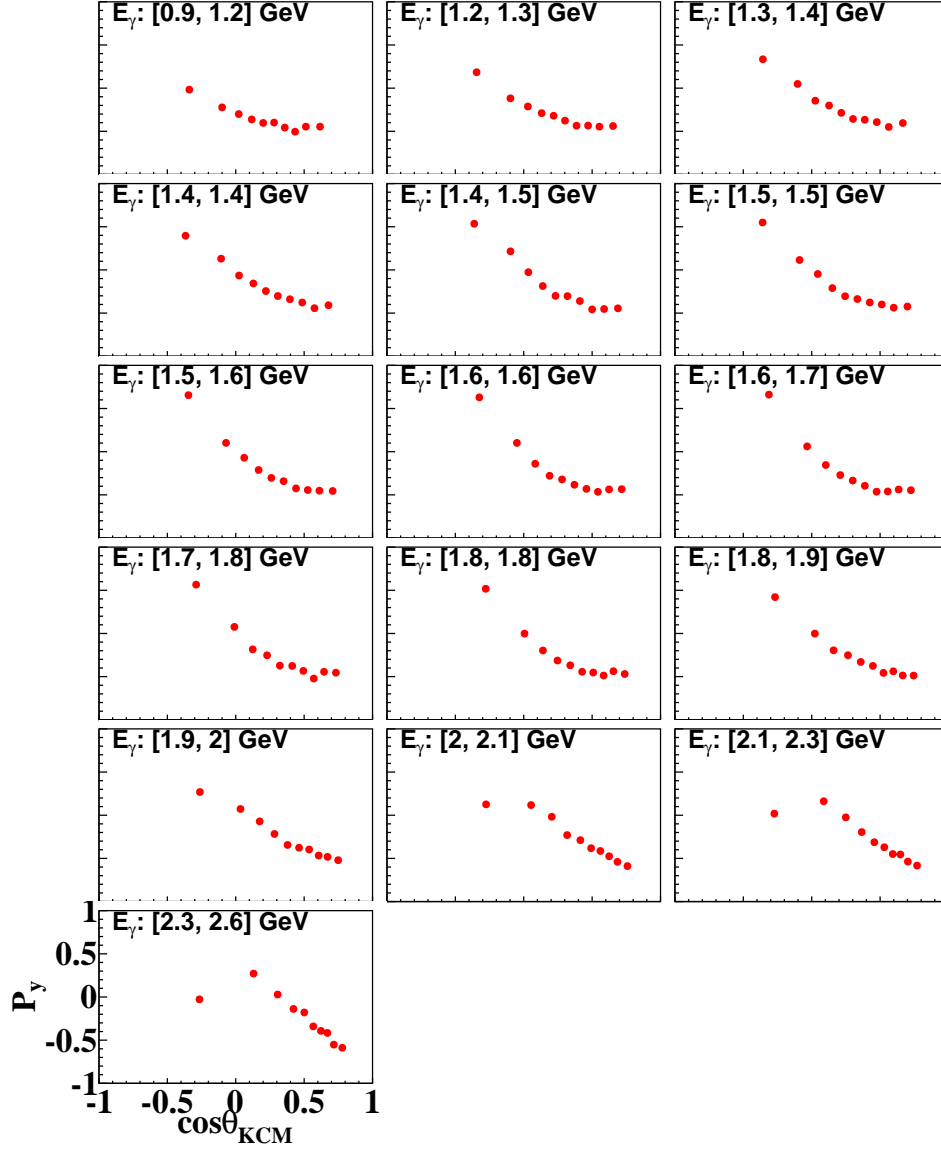


Figure 5.15: P_y as a function of $\cos\theta_{KCM}$ at fixed E_γ for the quasi-free mechanism of the reaction $\vec{\gamma}d \rightarrow K^+\vec{\Lambda}n$. The $\cos\theta_{KCM}$ values at which our results for P_y are reported, are the averages of the $\cos\theta_{KCM}$ values of all the events in the corresponding E_γ and $\cos\theta_{KCM}$ bins.

- Generally, C_x has a strong dependence on E_γ for all angular bins up to $\cos \theta_{KCM}$ of 0.5. For $\cos \theta_{KCM}$ above 0.5, C_x has a much weaker dependence on E_γ .
- C_z has a strong dependence on E_γ up to $\cos \theta_{KCM}$ of 0.35. For $\cos \theta_{KCM}$ between 0.35 and 0.52, C_z is practically constant with E_γ . For $\cos \theta_{KCM}$ above 0.52, one observes C_z to decrease as E_γ becomes larger than about 1.8 GeV. Overall C_z is large and positive for all kinematic bins.
- At the very backward $\cos \theta_{KCM}$ bin, P_y shows a peak-like E_γ dependence. Above $\cos \theta_{KCM}$ of -0.13 , P_y is a smooth function of E_γ . It increases as E_γ increases for $\cos \theta_{KCM}$ up to 0.52 and is practically constant with E_γ for $\cos \theta_{KCM}$ larger than 0.52.

The three polarization observables for $K^+\Lambda$ production off the free nucleon are related by the expression

$$R \equiv \sqrt{C_x^2 + C_z^2 + P_y^2} \leq 1 \quad (5.24)$$

as pointed out in [65]. The expression only places an upper limit on R and does not constrain R to a specific value. It is interesting to construct R from our results for C_x , C_z , and P_y for two reasons. First, R serves as a systematic check of the analysis. If the data yield R values systematically above the upper limit, it would mean that there is a source of systematic error that needs to be eliminated. Second, previously published CLAS results for C_x , C_z , and P_y for $K^+\Lambda$ photoproduction off the free proton suggested that $R = 1$ across all angles and kinematics covered in the g1c experiment [30]. It would be interesting to check if the reaction off the bound proton would yield a similar result.

Figure 5.19 shows R as a function of θ_{KCM} at fixed E_γ . Our results satisfy the relationship of Eq. (5.24). Basically, R is close to 1 at low E_γ . However, at high

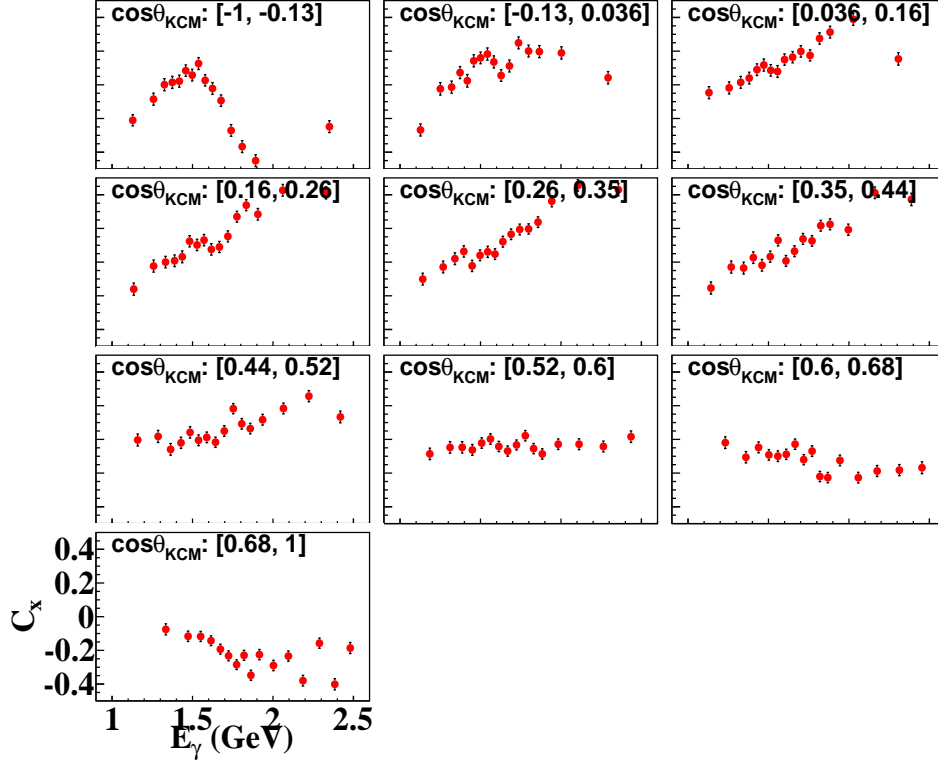


Figure 5.16: C_x as a function of E_γ at fixed $\cos\theta_{KCM}$ for the quasi-free mechanism of the reaction $\vec{\gamma}d \rightarrow K^+ \vec{\Lambda} n$. The E_γ values at which our results for C_x are reported, are the averages of the E_γ values of all the events in the corresponding E_γ and $\cos\theta_{KCM}$ bins.

E_γ , R is less than 1 at low θ_{KCM} , and it generally increases from lower value to 1 as θ_{KCM} increases.

Figure 5.20 shows our results for R as a function of E_γ in fixed θ_{KCM} bins. Our results satisfy Eq. (5.24), which means that our data pass successfully this systematic test. The kinematical dependence of R is interesting as our results are indeed consistent with 1, but only for some kinematics, mainly at lower energies. At E_γ between 1.5 GeV and 1.9 GeV, R is consistent with 1 only at forward and backward angles and is smaller than 1 at mid-angles. Above 1.9 GeV, R is consistent with 1 only at forward angles. An in-depth study of the observed discrepancies between the g1c and the g13 results is not a subject of this work, although some potential causes of systematic bias in the g1c results are discussed here.

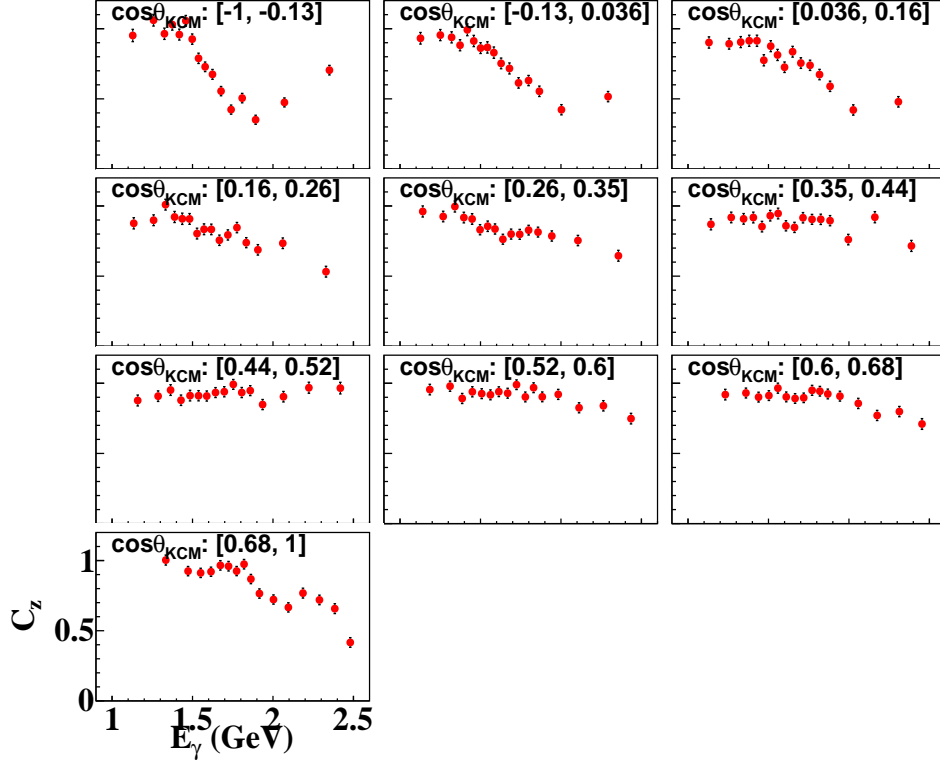


Figure 5.17: C_z as a function of E_γ at fixed $\cos\theta_{KCM}$ for the quasi-free mechanism of the reaction $\vec{\gamma}d \rightarrow K^+ \vec{\Lambda} n$. The E_γ values at which our results for C_z are reported, are the averages of the E_γ values of all the events in the corresponding E_γ and $\cos\theta_{KCM}$ bins.

5.4 DETERMINATION OF C_x , C_z , AND P_y FOR FINAL-STATE INTERACTIONS

Axis Convention

Figure 5.21 shows the axis convention we adopted for the determination of polarization observables for FSI of $\vec{\gamma}d \rightarrow K^+ \vec{\Lambda} n$. This convention is exactly the same as the one used in the theoretical calculation [6] of C_x , C_z , and P_y . The axes are defined in the lab frame. The z -axis points in the direction of the incoming photon, \vec{p}_γ . The y -axis is in the direction of the vector product $\vec{p}_\gamma \times \vec{p}_{K^+}$. The x -axis complements z and y to a right-handed reference frame. θ_K is the angle between \vec{p}_{K^+} and the z axis. θ'_Λ is the angle between the Λ momentum, \vec{p}_Λ , and the momentum transferred

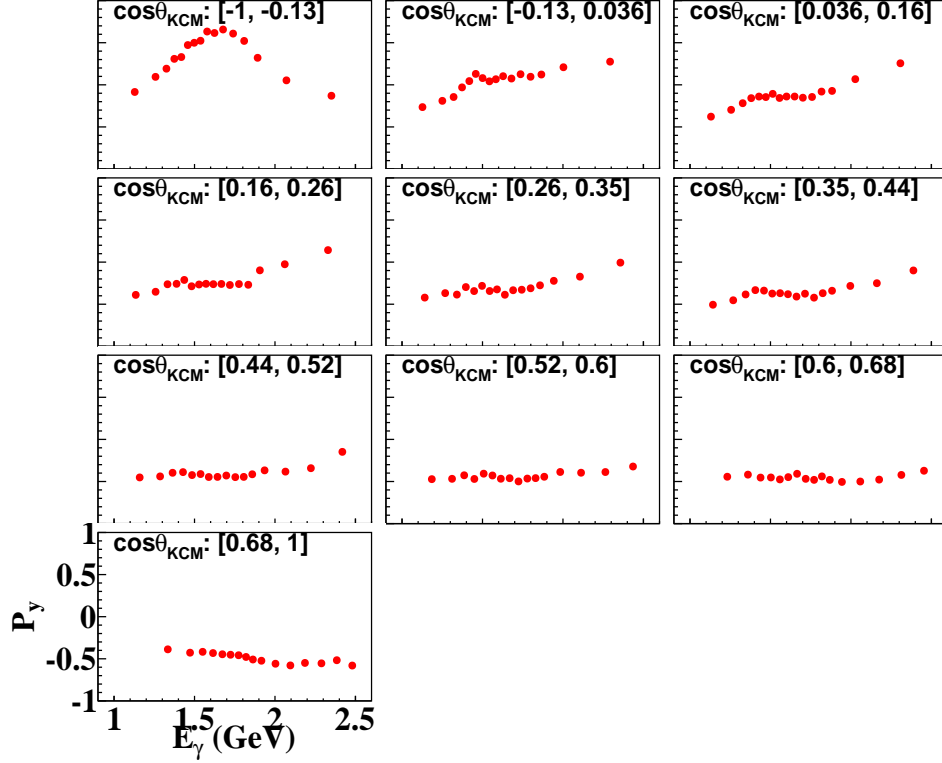


Figure 5.18: P_y as a function of E_γ at fixed $\cos\theta_{KCM}$ for the quasi-free mechanism of the reaction $\vec{\gamma}d \rightarrow K^+\vec{\Lambda}n$. The E_γ values at which our results for P_y are reported, are the averages of the E_γ values of all the events in the corresponding E_γ and $\cos\theta_{KCM}$ bins.

to the Λn system.

Kinematic Bins

Similar to the analysis of the quasi-free events, data for FSI were binned in two layers. The first layer contains kinematic variables of $\vec{\gamma}d \rightarrow K^+\vec{\Lambda}n$, such as E_γ , θ'_Λ , p_K , θ_K , and the invariant mass of Λn ($IM_{\Lambda n}$). The choice of variables is driven by the physics motivating the determination of observables in this study, access to Λn elastic scattering dynamics. The variables θ'_Λ and $IM_{\Lambda n}$ characterize the reaction $\Lambda n \rightarrow \Lambda n$, where the former is the hyperon scattering angle with respect to $\vec{p}_\Lambda + \vec{p}_n$ and the latter is the total center-of-mass energy in the Λn system. The other three variables,

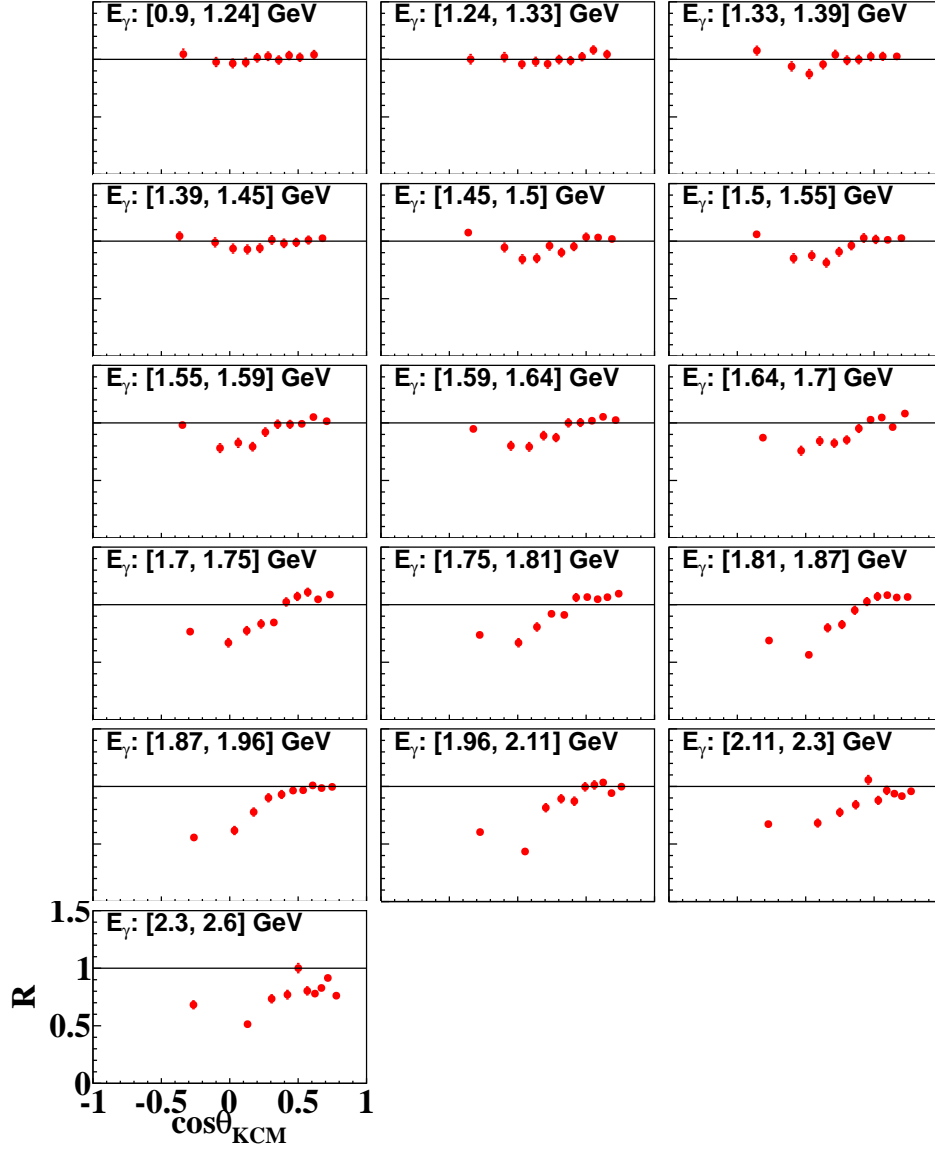


Figure 5.19: R as a function of $\cos\theta_{KCM}$ at fixed E_γ for the quasi-free mechanism of the reaction $\vec{\gamma}d \rightarrow K^+ \vec{\Lambda} n$. The $\cos\theta_{KCM}$ values at which our results for R are reported, are the averages of the $\cos\theta_{KCM}$ values of all the events in the corresponding E_γ and $\cos\theta_{KCM}$ bins. The black lines are drawn to visually show $R = 1$.

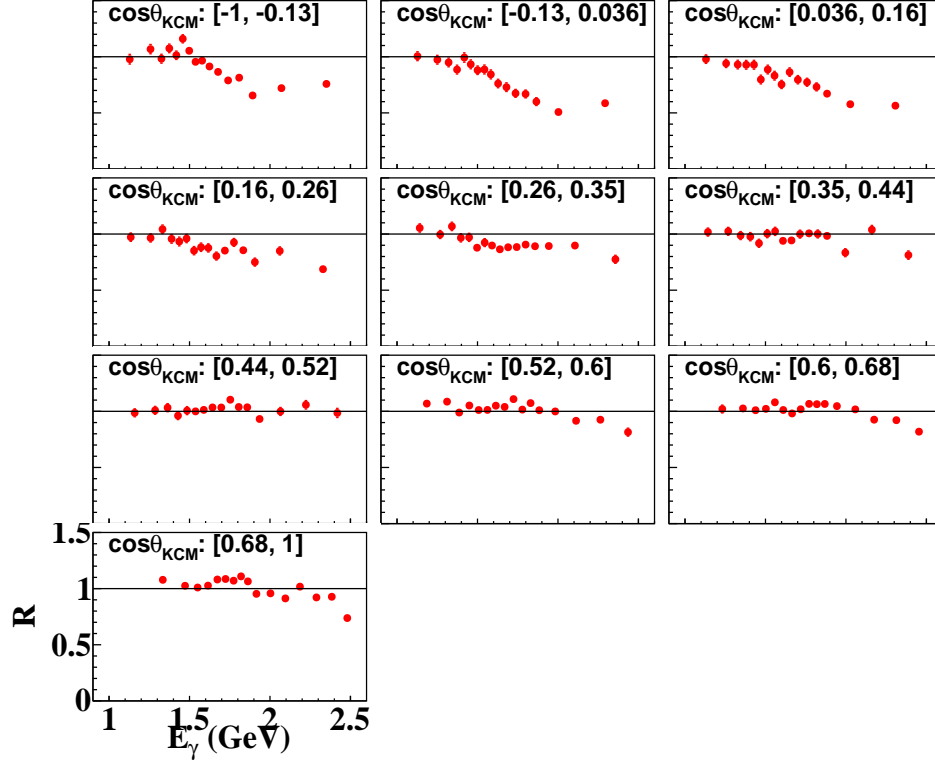


Figure 5.20: R as a function of E_γ at fixed $\cos\theta_{KCM}$ for the quasi-free mechanism of the reaction $\vec{\gamma}d \rightarrow K^+ \vec{\Lambda}n$. The E_γ values at which our results for R are reported, are the averages of the E_γ values of all the events in the corresponding E_γ and $\cos\theta_{KCM}$ bins. The black lines are drawn to visually show $R = 1$.

E_γ , θ_k , and p_k , characterize the first-step mechanism, $\gamma p \rightarrow K + \Lambda$. The second layer of variables is the same as in the QF analysis, and contains variables specific to the extraction of observables, such as photon helicity, $\cos\theta_z$, and $\cos\theta_x$.

Since the reaction of interest involves a three-body final state, it is described kinematically by five independent kinematic variables. Thus, the polarization observables are five-fold differential. Ideally, they would be extracted from data in simultaneous bins of five variables. Due to the limited statistics of the g13a sample, we could not bin the FSI data in five kinematic variables, and our results of C_x , C_z , and P_y are one-fold and two-fold differential estimates. It must be noted that the limitation to the number of variables in the first binning layer originates mostly by the statistics requirements of the background procedure combined with the fact that events in each

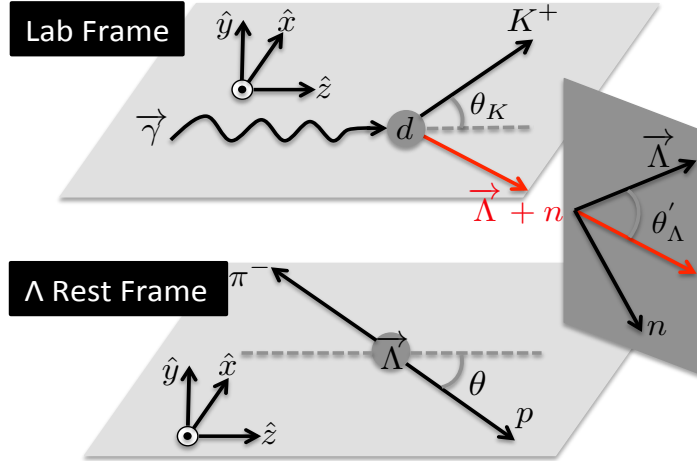


Figure 5.21: Axis convention used in the extraction of polarization observables for final-state interactions in the reaction $\vec{\gamma}d \rightarrow K^+ \vec{\Lambda} n$. Observables are reported in bins of E_γ , θ'_Λ , p_K , θ_K , and $IM_{\Lambda n}$. The cosine directions of the proton momentum in the Λ rest frame are used during the extraction of C_x , C_z , and P_y .

bin in the first layer need to be binned simultaneously in all the variables in the second layer. Background is then subtracted for any individual kinematic bin resulting from the two layers of variables. The number of variables in the first layer could be increased up to four if the background subtraction procedure is not applied or the background is determined by other means.

For one-fold differential estimates, the data were divided into 10 bins in E_γ , θ'_Λ , p_K , θ_K , and $IM_{\Lambda n}$, separately. For two-fold differential estimates, the data were divided into 5×5 bins in θ'_Λ and one of E_γ , p_K , θ_K , and $IM_{\Lambda n}$. The same technique as used in the quasi-free analysis to make all bins have similar statistics, was also applied here. In order to determine the probability of each event being a signal event, the MM background subtraction (as described in section 4.4) was performed for each bin.

Results

One-fold Differential Estimates

Figure 5.22 shows event distributions and binning over E_γ , θ'_Λ , p_K , θ_K , and $IM_{\Lambda n}$ for the extraction of one-fold differential estimates of C_x , C_z , and P_y . Figure 5.23 shows C_x , C_z , and P_y as a function of each kinematic variable. The red points are for C_x , the blue points are for C_z , and the green points are for P_y . The results suggest that:

- C_x is small and varies around 0.
- C_z varies between 0.4 and 0.8
- P_y varies between -0.4 and 0.1.
- Overall, C_x , C_z , and P_y have a weaker dependence on E_γ than on any other kinematic variable.

For the extraction of a spin-averaged Λn scattering length, estimates of observables in the range of $IM_{\Lambda n}$ from 2.05 GeV/ c^2 to 2.1 GeV/ c^2 are needed [27]. However, the statistics of our data is too low in this range to implement the background subtraction method. Figure 5.24 shows that the signal of $\vec{\gamma}d \rightarrow K^+ \vec{\Lambda} n$ is very nearly background free in the $IM_{\Lambda n}$ range of interest. Thus, the observables were extracted after a MM cut was applied. Figure 5.25 shows C_x , C_z , and P_y as a function of $IM_{\Lambda n}$. The data points have adequate statistical uncertainties for further physics analysis. The results suggest that C_x , C_z , and P_y are weakly dependent on $IM_{\Lambda n}$ in the limited $IM_{\Lambda n}$ range. We need to point out that fits to each observable, C_x , C_z , or P_y , are not expected to yield the same scattering length since the observables are different combinations of the Λn helicity amplitudes.

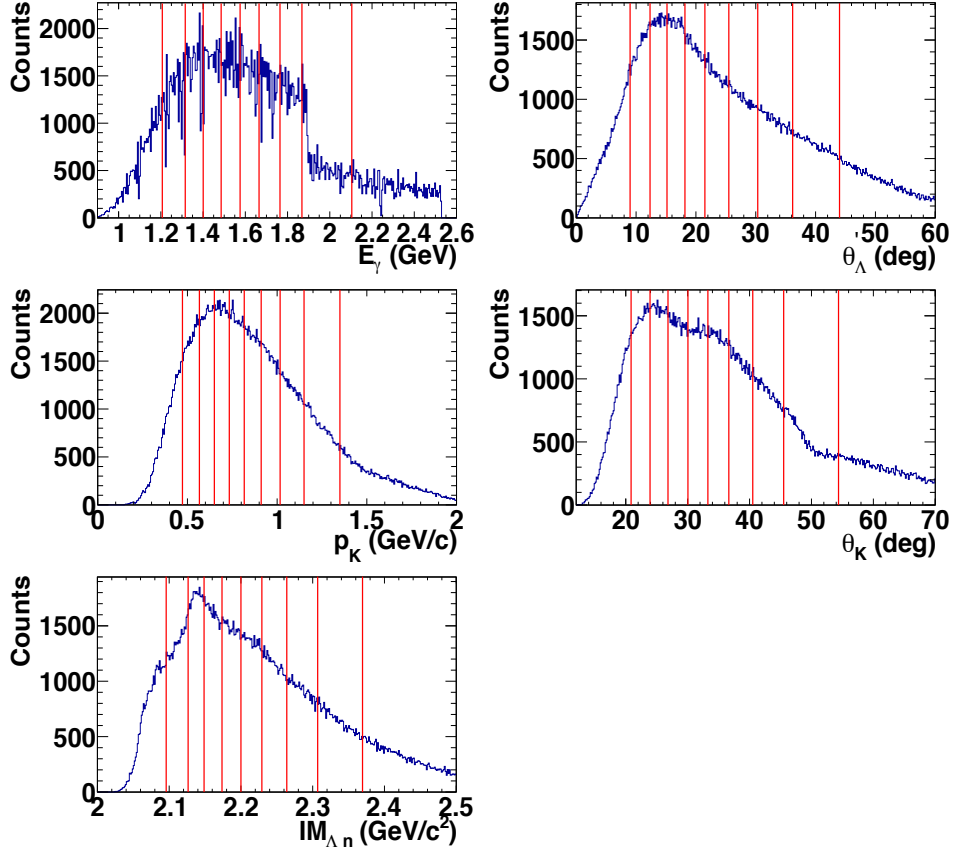


Figure 5.22: Event distributions and binning over E_γ (top left), θ'_Λ (top right), p_K (middle left), θ_K (middle right), and $IM_{\Lambda n}$ (bottom left) for the extraction of one-fold differential estimates of C_x , C_z , and P_y . The vertical red lines show the upper and the lower limits of the kinematic bins into which the data were divided. The widths of the bins were chosen such that the bins contained similar statistics.

Two-fold Differential Estimates

Figures 5.26 and 5.27 show the setup of kinematic binning in E_γ and θ'_Λ and our results for C_x , C_z , and P_y as a function of θ'_Λ at fixed E_γ , respectively. Our results show that

- Generally, C_x has a weaker dependence on θ'_Λ at low E_γ , and the variations of C_x become larger as E_γ increases.
- C_z decreases as θ'_Λ increases at lower E_γ . However, at higher E_γ , C_z has a weaker dependence on θ'_Λ .

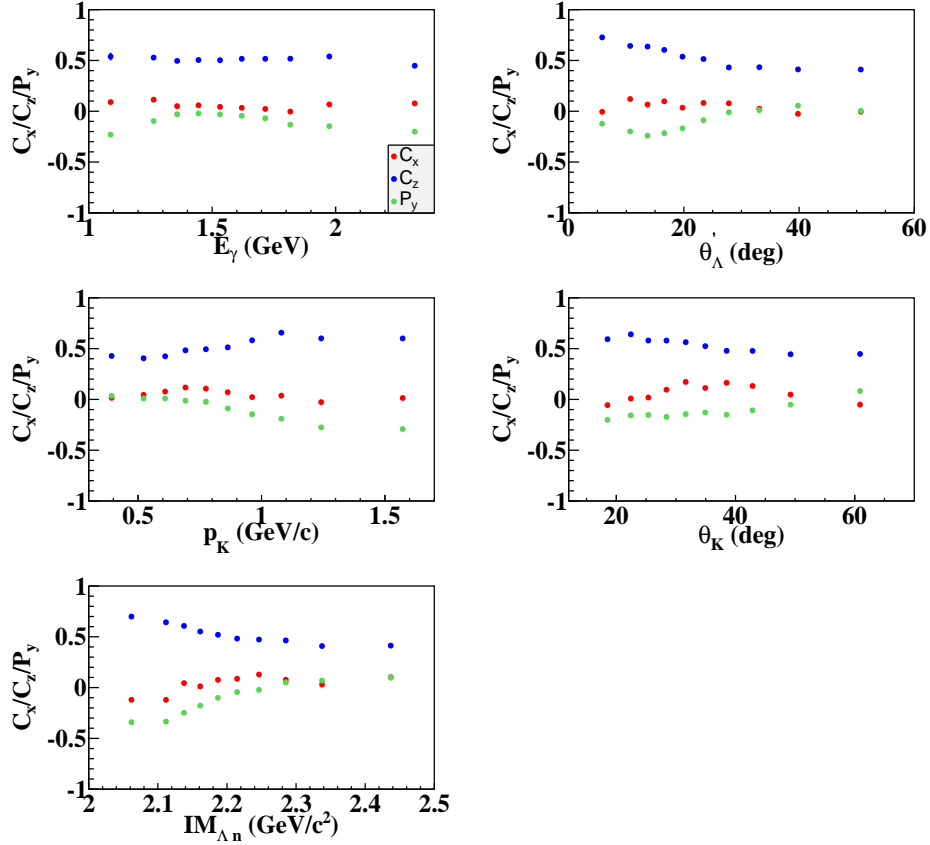


Figure 5.23: C_x , C_z , and P_y as a function of E_γ (top left), θ'_Λ (top right), p_K (middle left), θ_K (middle right), and $IM_{\Lambda n}$ (bottom left) for FSI of the reaction $\vec{\gamma}d \rightarrow K^+ \vec{\Lambda} n$. The red points show C_x , the blue points show C_z , and the green points show P_y .

- Overall, P_y decreases firstly and then increases as θ'_Λ increases for all E_γ .

Figures 5.28 and 5.29 show the setup of kinematic bins in p_K and θ'_Λ and our results for C_x , C_z , and P_y as a function of θ'_Λ for fixed p_K , respectively. Our results show that

- Overall, C_x varies around 0, and the variations on θ'_Λ become larger as p_K increases.
- Overall, C_z decreases as θ'_Λ for all p_K . However, the variation degree becomes lower as p_K increases.

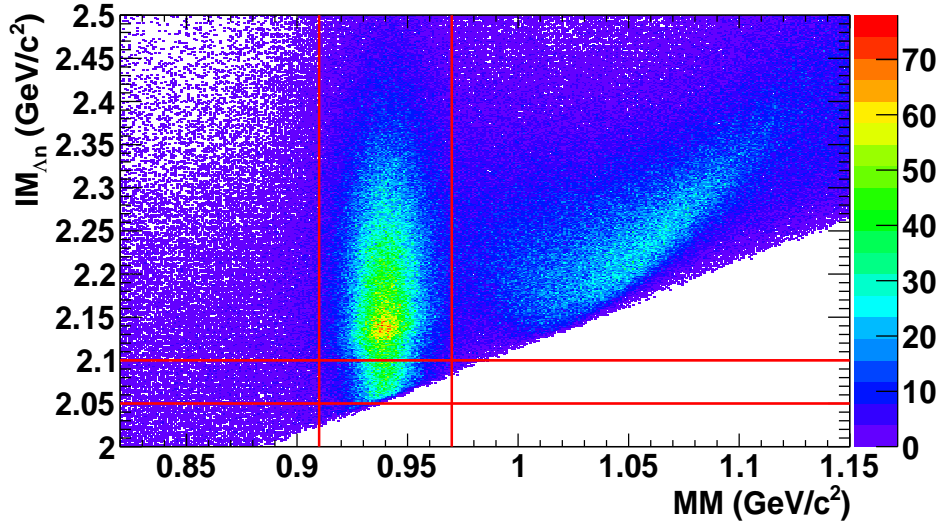


Figure 5.24: $IM_{\Lambda n}$ vs. MM for final-state interactions of the reaction $\vec{\gamma}d \rightarrow K^+ \vec{\Lambda}n$. The two horizontal red lines show the $IM_{\Lambda n}$ range of interest for the extraction of a spin-averaged Λn scattering length. The two vertical red lines show the MM cut applied to select the signal in the $IM_{\Lambda n}$ range of interest.

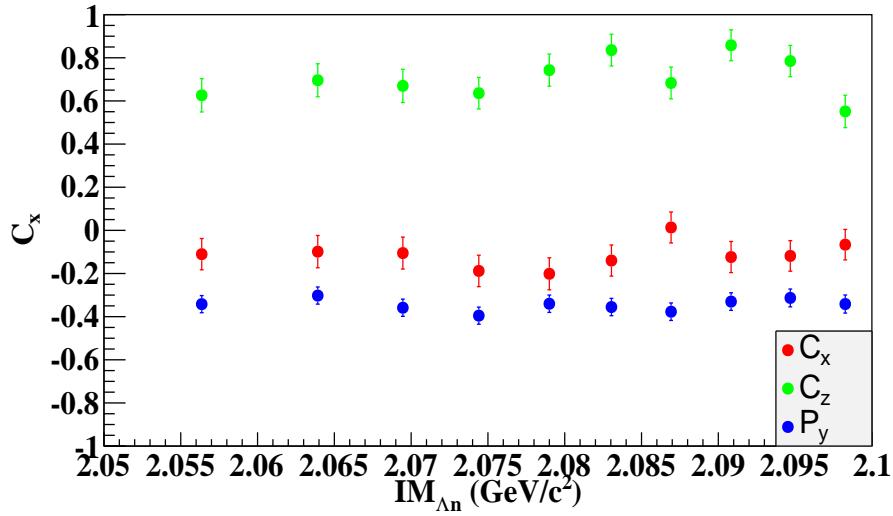


Figure 5.25: C_x , C_z , and P_y in the limited range of $IM_{\Lambda n}$ below the the Σn threshold for final-state interactions of the reaction $\vec{\gamma}d \rightarrow K^+ \vec{\Lambda}n$. The red points are for C_x . The green points are for C_z . The blue points are for P_y . The data points have adequate statistical uncertainties to be included in model fits for the determination of a spin-averaged Λn scattering length.

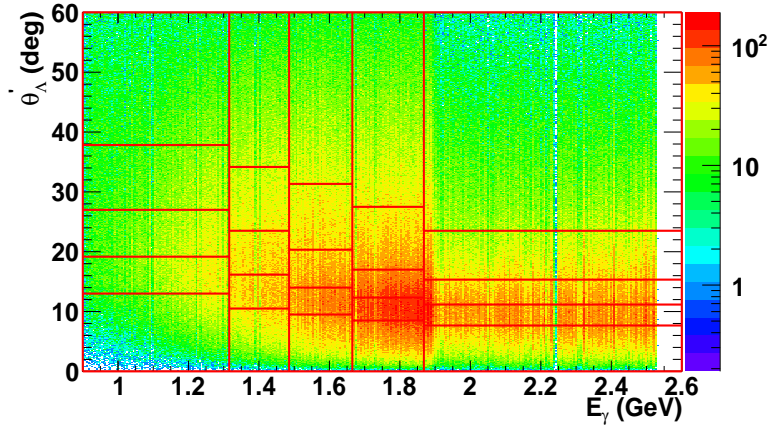


Figure 5.26: Setup of kinematic bins in E_γ and θ'_Λ for the FSI data. Each red box corresponds to one bin. Data do not seem to show any significant kinematic correlation between these two variables. For each E_γ , the data cover the full range in θ'_Λ from 0° to 60° .

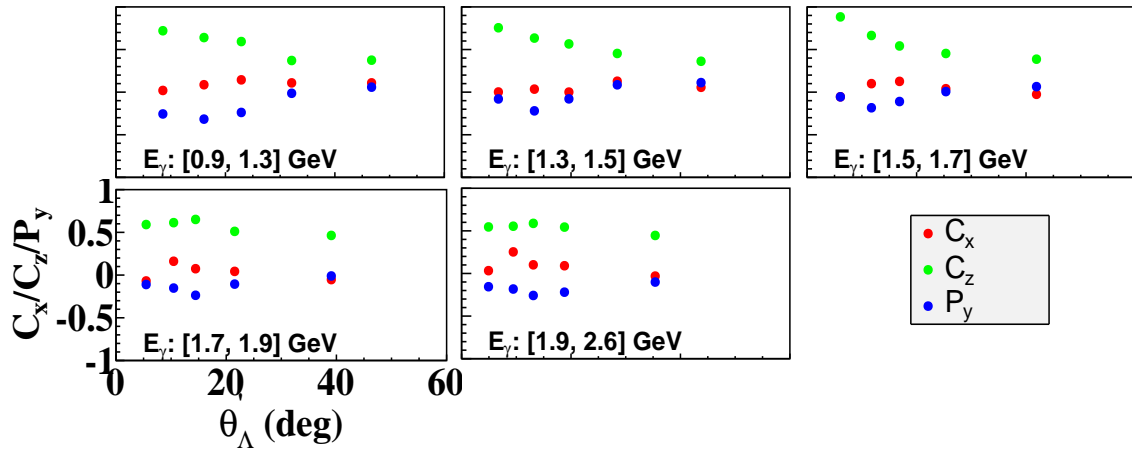


Figure 5.27: C_x , C_z , and P_y as a function of θ'_Λ for fixed E_γ . The red points are for C_x , the green points are for C_z , and the blue points are for P_y .

- Overall, P_y decreases firstly and then increases as θ'_Λ increases for all p_K .

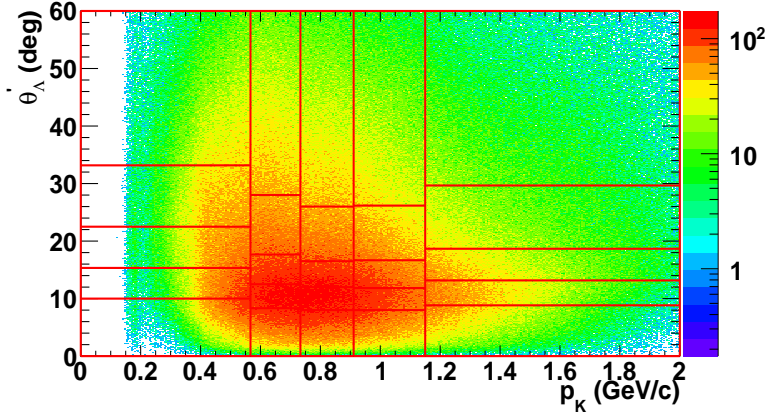


Figure 5.28: Setup of kinematic bins in p_K and θ'_Λ for the FSI data. Each red box corresponds to one bin. The upper limit of p_K increases first and then decreases as θ'_Λ increases, while the lower limit of p_K decreases first and then increases as θ'_Λ increases.

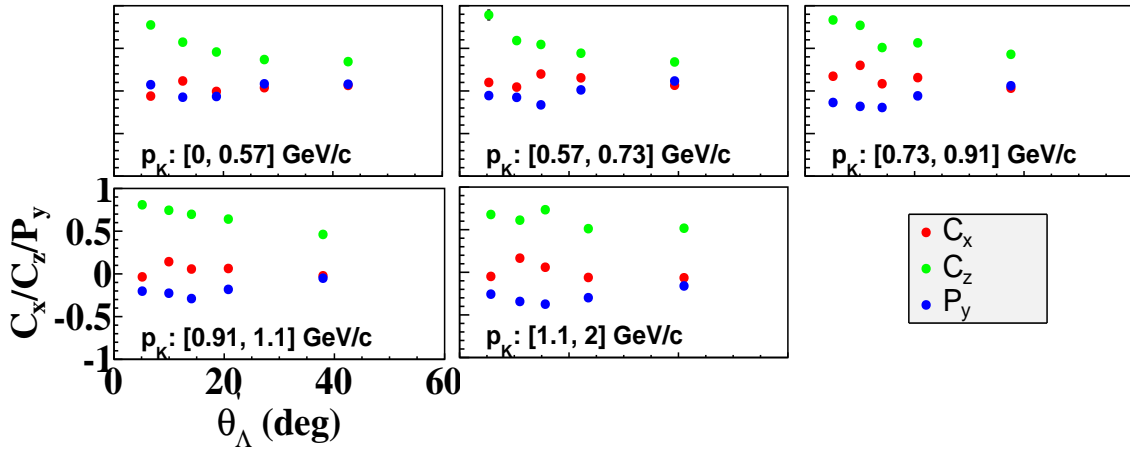


Figure 5.29: C_x , C_z , and P_y as a function of θ'_Λ for fixed p_K . The red points are for C_x , the green points are for C_z , and the blue points are for P_y .

Figures 5.30 and 5.31 show the setup of kinematic bins in θ_K and θ'_Λ and our results for C_x , C_z , and P_y as a function of θ'_Λ for fixed θ_K , respectively. Our results show that

- Generally, C_x decreases slowly as θ'_Λ increases at lower θ_K , while C_x increases slowly first and then decreases slowly as θ'_Λ increases at higher θ_K .
- Generally, C_z decreases as θ'_Λ increases for all θ_K .
- Generally, P_y increases as θ'_Λ increases at all θ_K .

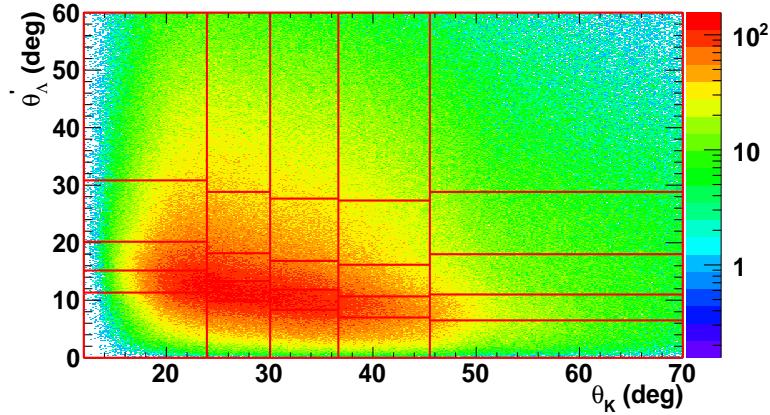


Figure 5.30: Setup of kinematic bins in θ_K and θ'_Λ for the FSI data. Each red box corresponds to one bin. The upper limit of θ_K increases first and then decreases as θ'_Λ increases, while the lower limit of θ_K decreases as θ'_Λ increases.

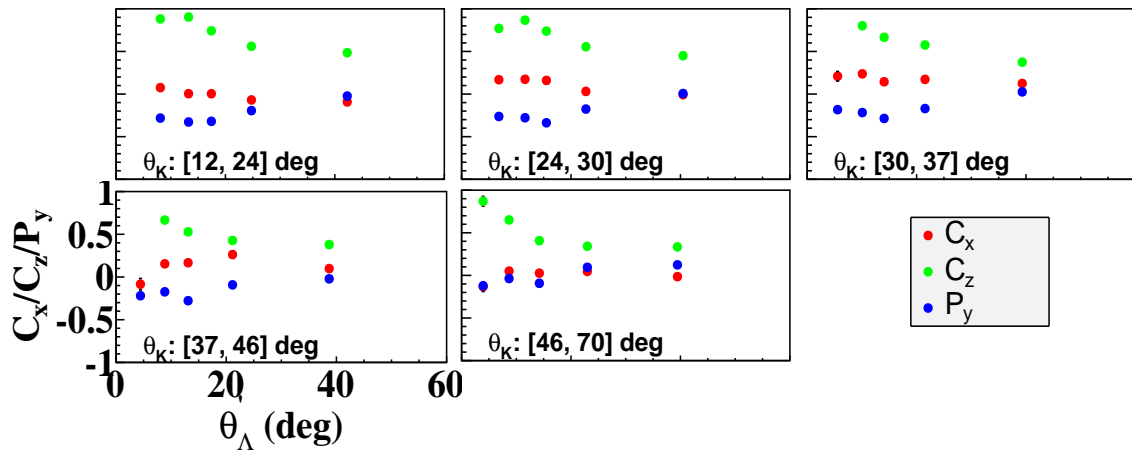


Figure 5.31: C_x , C_z , and P_y as a function of θ'_Λ for fixed θ_K . The red points are for C_x , the green points are for C_z , and the blue points are for P_y .

Figures 5.32 and 5.33 show the setup of kinematic bins in $IM_{\Lambda n}$ and θ'_Λ and our results for C_x , C_z , and P_y as a function of θ'_Λ for fixed $IM_{\Lambda n}$, respectively. Since the distribution of $IM_{\Lambda n}$ significantly depends on MM (see Fig. 5.24), the bin setup for this specific two-fold differential estimates was processed after applying a wide MM cut around the mass of neutron, otherwise the statistics of some θ'_Λ bins would be too low for the application of the background subtraction method at the next step of the analysis. This wide MM cut was applied only for the setup of kinematic bins and was removed during background subtraction and extraction of the observables. Our results show that

- Overall, C_x varies around 0 and has a weak dependence on θ'_Λ for all $IM_{\Lambda n}$.
- Overall, C_z decreases as θ'_Λ increases for all $IM_{\Lambda n}$.
- Overall, P_y decreases first and then increases as θ'_Λ increases at lower $IM_{\Lambda n}$, while P_y increases first and then decreases as θ'_Λ increases at higher $IM_{\Lambda n}$.

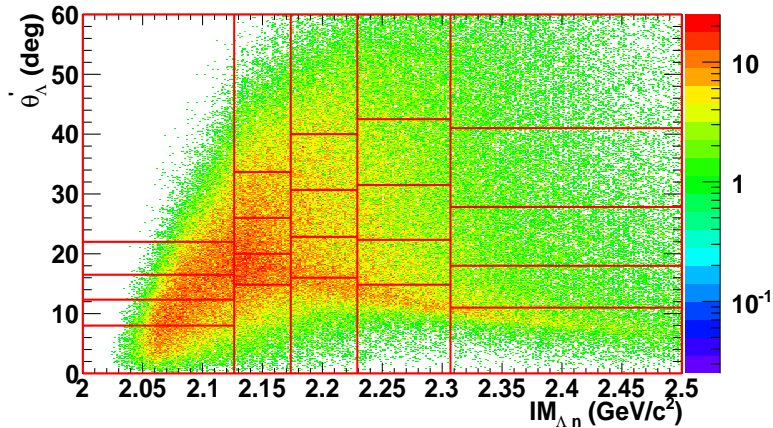


Figure 5.32: Setup of kinematic bins in $IM_{\Lambda n}$ and θ'_Λ for the FSI data. Differently from the setups of kinematic bins for other two-fold differential estimates, the data are binned over these two kinematic variables after MM cut is applied since $IM_{\Lambda n}$ has a strong dependence on MM. Each red box corresponds to one bin. The upper limit of $IM_{\Lambda n}$ increases as θ'_Λ increases, while the lower limit of $IM_{\Lambda n}$ increases first and then decreases as θ'_Λ increases.

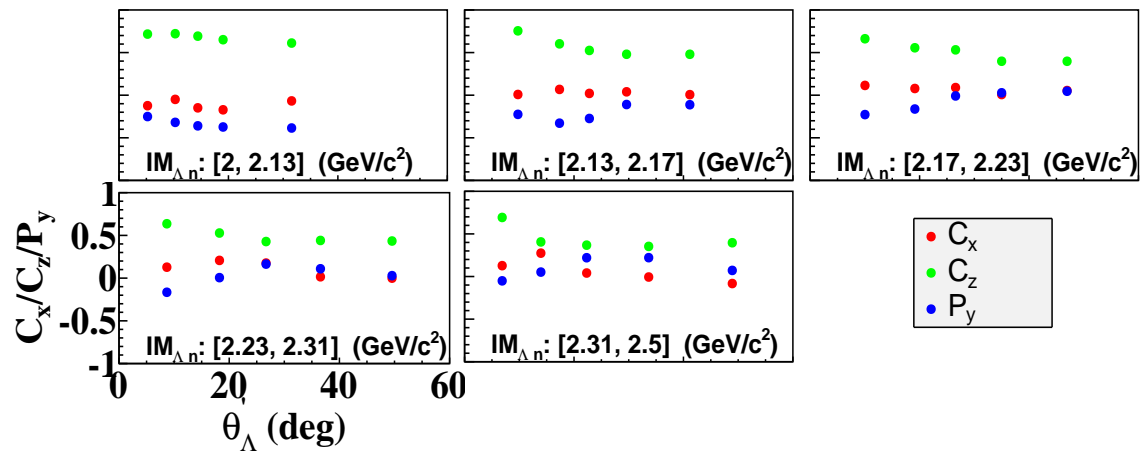


Figure 5.33: C_x , C_z , and P_y as a function of θ'_Λ for fixed $IM_{\Lambda n}$. The red points are for C_x , the green points are for C_z , and the blue points are for P_y .

CHAPTER 6

SYSTEMATIC UNCERTAINTIES

The total uncertainty of each of our estimates of C_x , C_z , and P_y has two components: a statistical uncertainty and a systematic uncertainty. The error bars of each of our estimates for C_x , C_z , and P_y shown in any figure in this document reflect the statistical uncertainty of that estimate, which is determined by the counting statistics in each bin. Systematic uncertainties are independent of the number of signal events in a bin, and are more concerned with effects that could introduce random biases in our results. This chapter describes our studies to estimate the systematic uncertainties of C_x , C_z , and P_y from various sources.

In general, to estimate the systematic uncertainty originating from our specific choice of the various cuts described in Chapter 4, we extracted the same set of observables by applying a narrower range of the cut under study. The full analysis was performed, including background subtraction. This procedure yielded a new sample of estimates for each observable. The mean value of the distribution over the relative difference between the new and the nominal estimates is then reported as the systematic uncertainty of that observable due to the cut under study. Data points over $\cos\theta_{KCM}$ for fixed E_γ for the quasi-free mechanism and data points over θ'_Λ for fixed p_K for the final-state interactions (185 data points in total) are included together in the relative-difference distributions. Further details are given in the following sections.

6.1 ACCEPTANCE

The study described in section 5.1 established that the acceptance of CLAS had different effects on observables extracted with different methods. Most importantly, it was found that the maximum likelihood method is a subject to small biases that are acceptance dependent. As shown in Table 5.1, the biases of C_x , C_z , and P_y caused by the maximum likelihood method are 0.00486, -0.00261, and 0.00803, respectively. To estimate the corresponding systematic uncertainties, we calculated the relative differences $(Obs_{ext} - Obs_{true})/Obs_{true}$, where Obs stands for C_x , C_z , or P_y . For each of the 6000 experiments, we obtained one value of the relative difference for each observable. The distribution of the 6000 relative differences for C_x , C_z , and P_y , are shown in Fig. 6.1 left, middle, and right, respectively. The mean value of each distribution is reported as a systematic uncertainty of the corresponding observable due to the CLAS acceptance. The uncertainties of C_x , C_z , and P_y are 5.5%, 0.3%, and 3.5%, respectively. Alternatively, one could use the mean values shown in Fig. 6.1 to correct our estimates of the observables and to eliminate the bias. However, one needs to remember that the simulated CLAS acceptance is not necessarily consistent with the true CLAS acceptance. Moreover, the discrepancies between the simulated and the true acceptance can vary with kinematic bins. In this situation, correcting the data for the deviations observed in Fig. 6.1 would not be a good approach. Rather, we consider the deviations to be representative of the magnitudes of the biases due to detector acceptance and, therefore, report them as systematic uncertainties. This uncertainty could eventually be reduced by using a normalized probability density function in the maximum likelihood method.

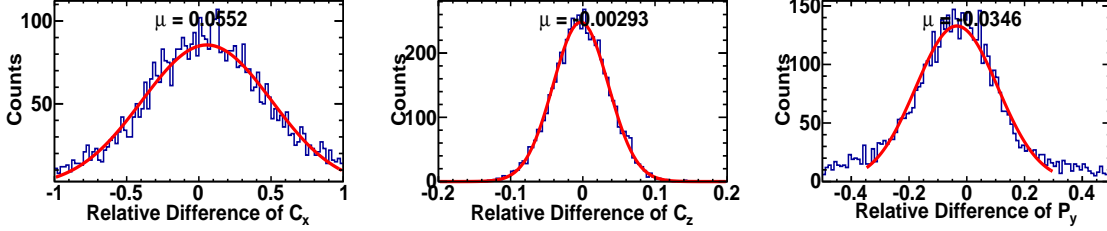


Figure 6.1: Distributions of relative difference $(Obs_{ext} - Obs_{true})/Obs_{true}$ for C_x (left), C_z (middle), and P_y (right). The values in the distributions are obtained from simulations of 6000 independent experiments as described in section 5.1. The mean value of each distribution is denoted by μ and is shown on each figure. We report each of these values as the systematic uncertainty due to detector acceptance of the corresponding observable.

6.2 FIDUCIAL CUTS

Since the efficiency of particle detection in the CLAS drift chambers decreases to zero at the detector boundaries, it is necessary to estimate the effect of varying acceptance in these regions on our results. In order to quantify the effect, observables were estimated from a data sample in which the boundaries of the CLAS detector, where the acceptance strongly varied, were removed. These results were then compared with our nominal results. Events detected at the boundary regions were removed by applying fiducial cuts [55] to our data sample. Since the fiducial area of the CLAS depends on particle charge and type, we applied different fiducial cuts for the K^+ , p , and π^- (see Fig. 6.2 for an example of fiducial cuts).

Figure 6.3 shows distributions of the relative differences between the nominal estimates of C_x , C_z , and P_y (without fiducial cuts) and the estimates obtained with fiducial cuts. The distributions are well described by Gaussian functions and the mean values are reported as systematic uncertainties due to the varying CLAS acceptance in the fiducial regions. The uncertainty is 0.1%, 0.3%, and 0.1% for C_x , C_z , and P_y respectively.

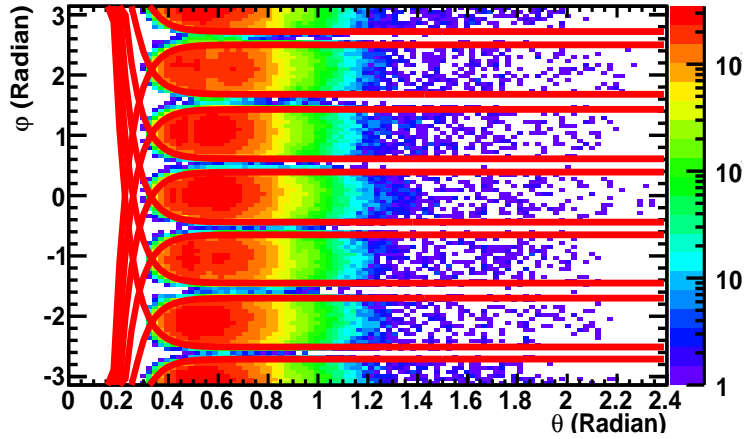


Figure 6.2: Fiducial cuts (indicated by the solid red lines) for protons with momenta between $0.4 \text{ GeV}/c$ and $0.8 \text{ GeV}/c$. Only events within the red solid lines were kept for further analysis. The fiducial cuts were determined in [55]. The red lines show the cut ranges.

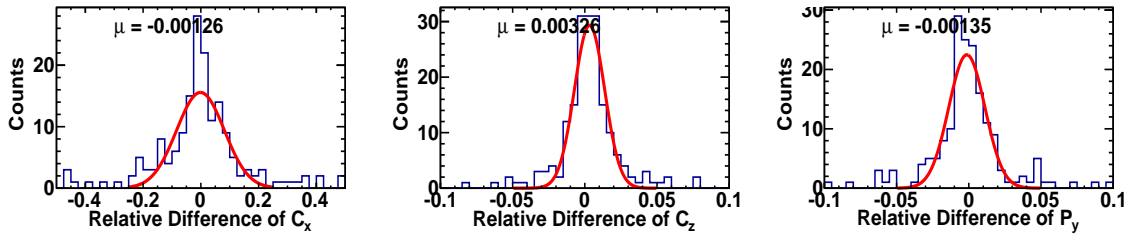


Figure 6.3: Distributions of the relative differences of observables estimated without (nominal values) and with applied fiducial cuts. The relative difference is defined as $(Obs - Obs_{FC})/Obs$, where Obs denotes our nominal estimate of C_x , C_z , or P_y , and Obs_{FC} denotes the estimate with applied fiducial cuts. The left figure is for C_x , the middle figure is for C_z , and the right figure is for P_y . The red lines show fits to Gaussian functions. The mean value of each distribution is reported as the systematic uncertainty of the corresponding observable due to varying CLAS acceptance at the fiducial boundaries.

6.3 PARTICLE IDENTIFICATION

The systematic uncertainty due to our specific choice of PID cuts is quantified by comparing our nominal estimates of C_x , C_z , and P_y (obtained with 3σ $\Delta\beta$ PID cuts for K^+ and p and ± 0.2 cut for π^-) to estimates obtained with 2σ $\Delta\beta$ PID cuts for K^+ and p and ± 0.05 cut for π^- (see section 4.1 for details on the PID method). Figure 6.4 shows $\Delta\beta$ as a function of momentum for proton candidates with the 3σ and the 2σ PID cuts shown by the solid red and black lines, respectively. A 3σ cut would allow more events from the tails of the $\Delta\beta$ vs. momentum distribution in the sample. Similarly, 2σ PID cut was applied to select K^+ tracks. The cut range of $\Delta\beta$ changed from ± 0.2 to ± 0.05 for the π^- PID. The three narrower PID cuts were applied simultaneously.

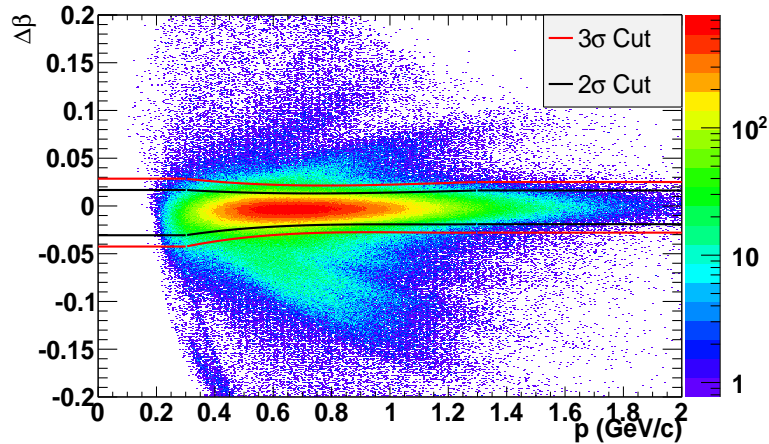


Figure 6.4: $\Delta\beta$ as a function of momentum with 3σ and 2σ cuts for proton PID. The red curves show the 3σ cut, and the black curves show the 2σ cut.

Figure 6.5 shows distributions of relative differences between our nominal estimates for C_x , C_z , and P_y and estimates obtained with narrower PID cuts. The distributions are well described by Gaussian functions. The mean value of each distribution is reported as the systematic uncertainty of the corresponding observable due to our specific choice of PID cut. The uncertainty is 2.7%, 2.7%, and 0.2% for

C_x , C_z , and P_y , respectively.

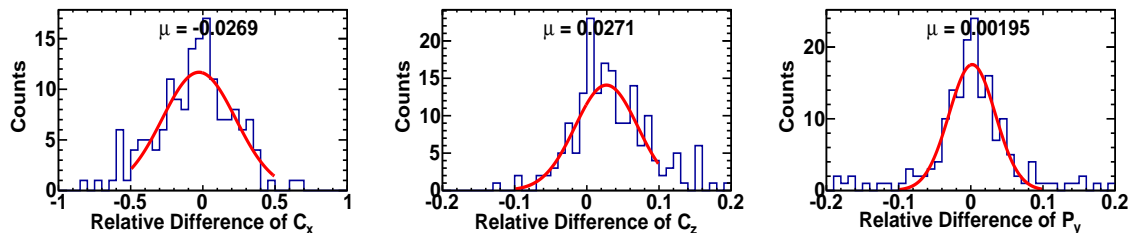


Figure 6.5: Distributions of the relative differences of observables estimated with a broader PID selection cut (nominal values) and with a narrower PID selection cut. The relative difference is defined as $(Obs - Obs_{narr})/Obs$, where Obs denotes our nominal estimate of C_x , C_z , or P_y , and Obs_{narr} denotes the estimate with a narrower PID cut. The left figure is for C_x , the middle figure is for C_z , and the right figure is for P_y . The red lines show fits to Gaussian functions. The mean value of each distribution is reported as the systematic uncertainty of the corresponding observable due to our specific choice of PID selection cuts.

6.4 VERTEX CUT

To estimate the uncertainty due to our specific choice for the range of the vertex cut, the latter was varied from $[-40, 0]$ cm (nominal range) to $[-39, 1]$ cm. Figure 6.6 shows distributions of relative differences between our nominal estimates for C_x , C_z , and P_y and estimates obtained with the narrower vertex cut. The distributions are well described by Gaussian functions. The mean value of each distribution is reported as the systematic uncertainty of the corresponding observable due to our specific choice of the vertex cut. The uncertainty is 1.4%, 0%, and 0.1% for C_x , C_z , and P_y , respectively.

6.5 PHOTON SELECTION

In order to quantify the systematic uncertainty due to our specific choice of a cut range for photon selection, the cut was varied from ± 1 ns (our nominal cut) to ± 0.6 ns. Figure 6.7 shows distributions of relative differences between our nominal estimates

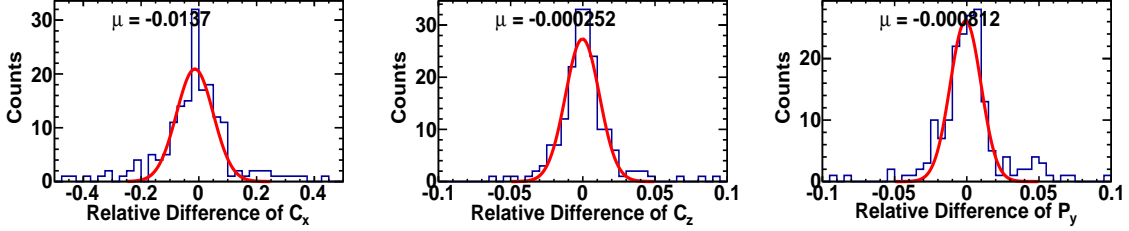


Figure 6.6: Distributions of the relative differences of observables estimated with a broader vertex cut (nominal values) and with a narrower vertex cut. The relative difference is defined as $(Obs - Obs_{narr})/Obs$, where Obs denotes our nominal estimate of C_x , C_z , or P_y , and Obs_{narr} denotes the estimate with a narrower vertex cut. The left figure is for C_x , the middle figure is for C_z , and the right figure is for P_y . The red lines show fits to Gaussian functions. The mean value of each distribution is reported as the systematic uncertainty of the corresponding observable due to our specific choice of the vertex cut.

for C_x , C_z , and P_y and estimates obtained with the narrower photon selection cut. The distributions are well described by Gaussian functions. The mean value of each distribution is reported as the systematic uncertainty of the corresponding observable due to our specific choice of the photon selection cut. The uncertainty is 0.1%, 0.3%, and 0.1% for C_x , C_z , and P_y , respectively.

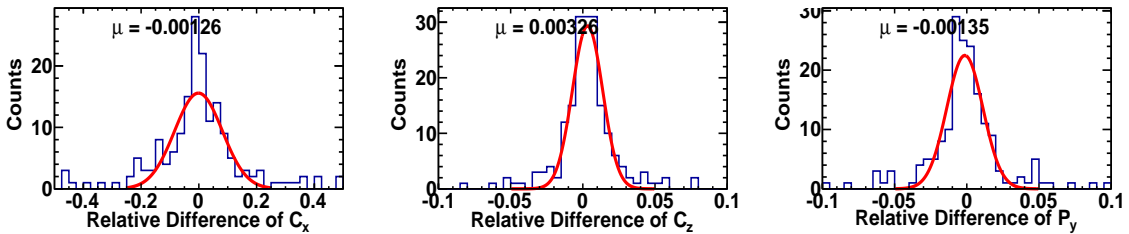


Figure 6.7: Distributions of the relative differences of observables estimated with a broader photon selection cut (nominal values) and with a narrower photon selection cut. The relative difference is defined as $(Obs - Obs_{narr})/Obs$, where Obs denotes our nominal estimate of C_x , C_z , or P_y , and Obs_{narr} denotes the estimate with a narrower photon selection cut. The left figure is for C_x , the middle figure is for C_z , and the right figure is for P_y . The red lines show fits to Gaussian functions. The mean value of each distribution is reported as the systematic uncertainty of the corresponding observable due to our specific choice of the photon selection cut.

6.6 INVARIANT MASS CUT

The systematic uncertainty due to our specific choice of IM cut is quantified by comparing our nominal estimates of C_x , C_z , and P_y (obtained with a 3σ IM cut) to estimates obtained with a 2σ IM cut. Figure 6.8 shows distributions of relative differences between our nominal estimates for C_x , C_z , and P_y and estimates obtained with the narrower IM cut. The distributions are well described by Gaussian functions. The mean value of each distribution is reported as the systematic uncertainty of the corresponding observable due to our specific choice of the IM cut. The uncertainty is 1.4%, 0.7%, and 0.3% for C_x , C_z , and P_y , respectively.

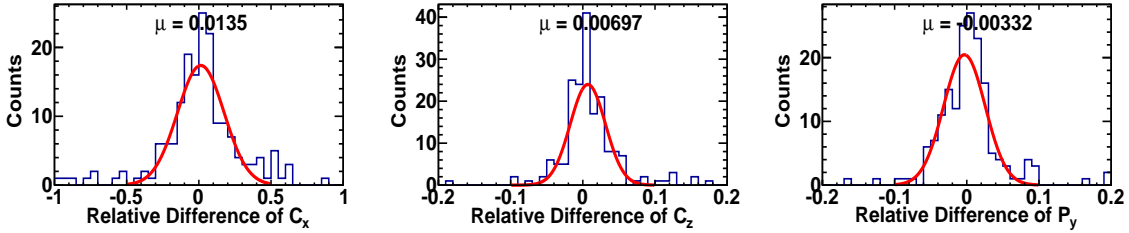


Figure 6.8: Distributions of the relative differences of observables estimated with a broader IM selection cut (nominal values) and with a narrower IM selection cut. The relative difference is defined as $(Obs - Obs_{narr})/Obs$, where Obs denotes our nominal estimate of C_x , C_z , or P_y , and Obs_{narr} denotes the estimate with a narrower IM cut. The left figure is for C_x , the middle figure is for C_z , and the right figure is for P_y . The red lines show fits to Gaussian functions. The mean value of each distribution is reported as the systematic uncertainty of the corresponding observable due to our specific choice of IM selection cuts.

6.7 MISSING MOMENTUM CUT

To estimate the uncertainty due to our specific choice of the missing-momentum value that divides our data between the quasi-free mechanism and the final-state interactions, the MP cut for QF was varied from 0.2 GeV/ c to 0.15 GeV/ c , and the MP cut for FSI was varied from 0.2 GeV/ c to 0.25 GeV/ c . Figure 6.9 shows distributions of relative differences between our nominal estimates for C_x , C_z , and

P_y and estimates obtained with the narrower MP cut. The distributions are well described by Gaussian functions. The mean value of each distribution is reported as the systematic uncertainty of the corresponding observable due to our specific choice of the MP cut. The uncertainty is 0.6%, 0.2%, and 0.1% for C_x , C_z , and P_y , respectively.

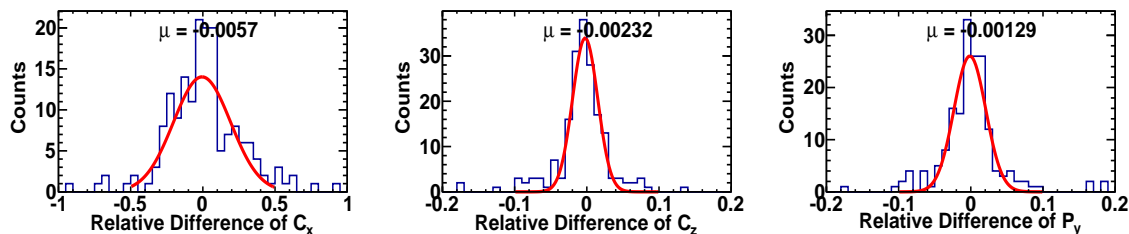


Figure 6.9: Distributions of the relative differences of observables estimated with a broader MP selection cut (nominal values) and with a narrower MP selection cut. The relative difference is defined as $(Obs - Obs_{narr})/Obs$, where Obs denotes our nominal estimate of C_x , C_z , or P_y , and Obs_{narr} denotes the estimate with a narrower MP cut. The left figure is for C_x , the middle figure is for C_z , and the right figure is for P_y . The red lines show fits to Gaussian functions. The mean value of each distribution is reported as the systematic uncertainty of the corresponding observable due to our specific choice of MP selection cuts.

6.8 MISSING MASS CUT

The systematic uncertainty due to our specific choice of a MM cut is quantified by comparing our nominal estimates of C_x , C_z , and P_y (obtained with a 3σ MM cut) to estimates obtained with a 2σ MM cuts. Figure 6.10 shows distributions of relative differences between our nominal estimates for C_x , C_z , and P_y and estimates obtained with the narrower MM cut. The distributions are well described by Gaussian functions. The mean value of each distribution is reported as the systematic uncertainty of the corresponding observable due to our specific choice of the MM cut. The uncertainty is 1.6%, 3.2%, and 2.1% for C_x , C_z , and P_y , respectively.

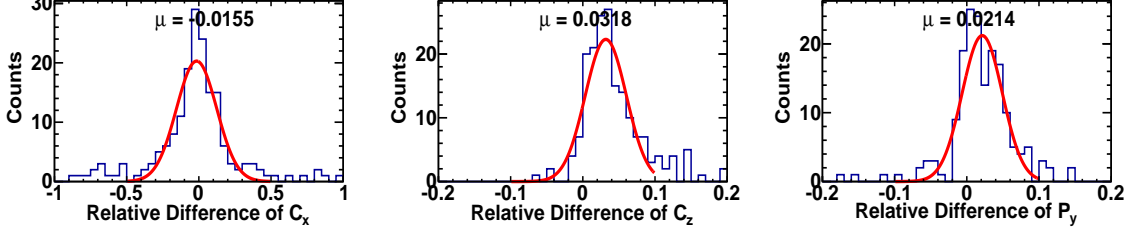


Figure 6.10: Distributions of the relative differences of observables estimated with a broader MM selection cut (nominal values) and with a narrower MM selection cut. The relative difference is defined as $(Obs - Obs_{narr})/Obs$, where Obs denotes our nominal estimate of C_x , C_z , or P_y , and Obs_{narr} denotes the estimate with a narrower MM cut. The left figure is for C_x , the middle figure is for C_z , and the right figure is for P_y . The red lines show fits to Gaussian functions. The mean value of each distribution is reported as the systematic uncertainty of the corresponding observable due to our specific choice of MM selection cuts.

Table 6.1: Summary of the systematic uncertainties for C_x , C_z , and P_y . The total uncertainty is obtained by adding all the uncertainties in quadrature and taking a square root of the sum. Overall, the total systematic uncertainty of each observable is less than 10%.

Source	C_x	C_z	P_y
CLAS Acceptance	5.5%	0.3%	3.5%
Fiducial Cut	0.1%	0.3%	0.1%
PID	2.7%	2.7%	0.2%
Vertex Cut	1.4%	0%	0.1%
Photon Selection	0.1%	0.3%	0.1%
IM Cut	1.4%	0.7%	0.3%
MP Cut	0.6%	0.2%	0.1%
MM Cut	1.6%	3.2%	2.1%
Λ Self-analyzing Power	2.0%	2.0%	2.0%
Total	7.0%	4.7%	4.6%

6.9 SUMMARY OF SYSTEMATIC UNCERTAINTIES

The systematic uncertainties due to various sources are summarized in Table 6.1. The total systematic uncertainty is obtained by adding in quadrature each of the individual uncertainties and taking a square root of the sum. The total systematic uncertainty of C_x is 7.0%, of C_z is 4.7%, and of P_y is 4.6%.

CHAPTER 7

DISCUSSION

7.1 COMPARISON TO PUBLISHED RESULTS

In section 1.4, we point out that the results for the FSI of $\vec{\gamma}d \rightarrow K^+ \vec{\Lambda} n$ are the first ever obtained, but the QF results can be compared to the published results from the reaction $\vec{\gamma}p \rightarrow K^+ \vec{\Lambda}$. To compare our results to the published CLAS results from the g1c experiment [29, 66], we rebinned data in E_γ and θ_{KCM} so that the bin setup was consistent between the g1c and the g13 results. Since statistics of our data were too low to obtain reliable results in bins of low E_γ and low θ_{KCM} , we compared our results of bins with high statistics to the published results. Figures 7.1, 7.2, and 7.3 show comparisons between the g1c and g13 experiments for C_x , C_z , and P_y , respectively. In general, C_z and P_y are consistent with each other, while there are systematic differences for C_x . The g1c results were extracted by the 1D fit method. In section 5.1, we established that the 1D fit method causes biases of the polarization observables due to the effect of detector acceptance, especially for C_x . We also determined that the biases can be significantly reduced if the observables were extracted by the maximum likelihood method. Thus, we attribute the discrepancies between ours and the g1c results for C_x to bias in the 1D fit method used in the g1c analysis. The agreement of C_z with the g1c results suggests that there are no big systematic problems in the determination of the photon polarization and helicity in the g13a data and analysis.

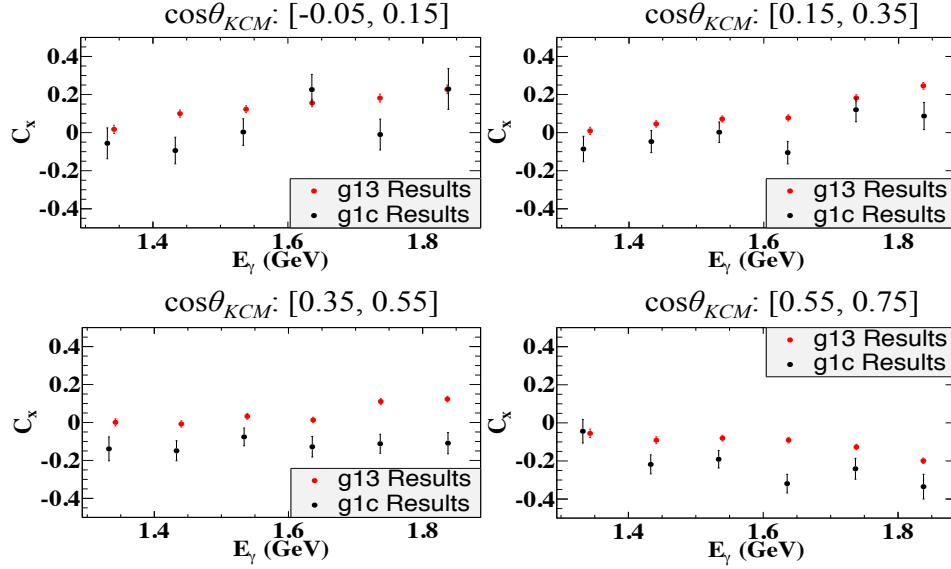


Figure 7.1: Comparison of C_x between the g1c and g13 experiments. Overall, the g13 results are systematically larger than the g1c results. This is attributed to the bias in the 1D fit method used in the g1c analysis. The g13a data points have significantly smaller statistical uncertainties due to the larger number of events collected in g13 than in g1c.

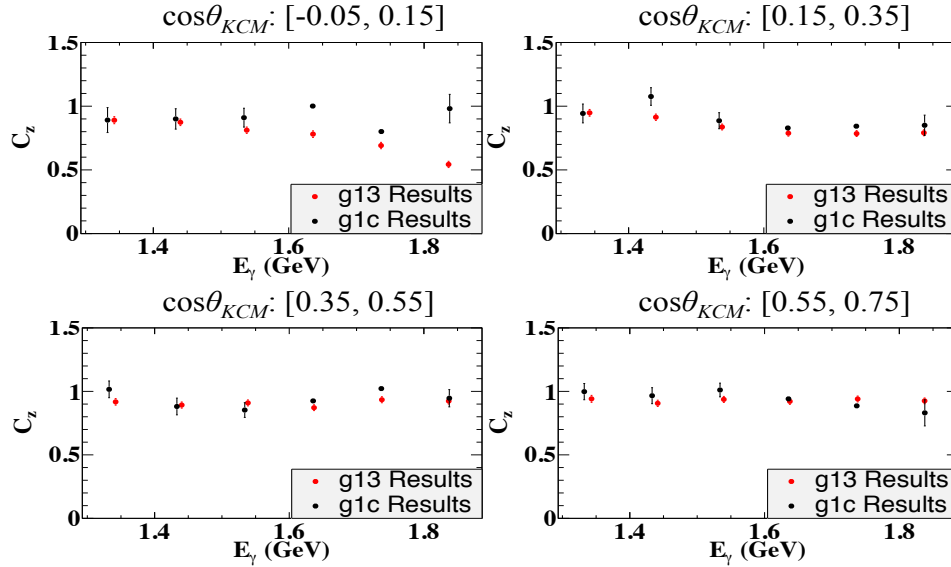


Figure 7.2: Comparison of C_z between the g1c and g13 experiments. Overall, the agreement between the two sets of results is reasonable. This suggests that there are no big systematic problems in the determination of the photon polarization and helicity in the g13a data and analysis.

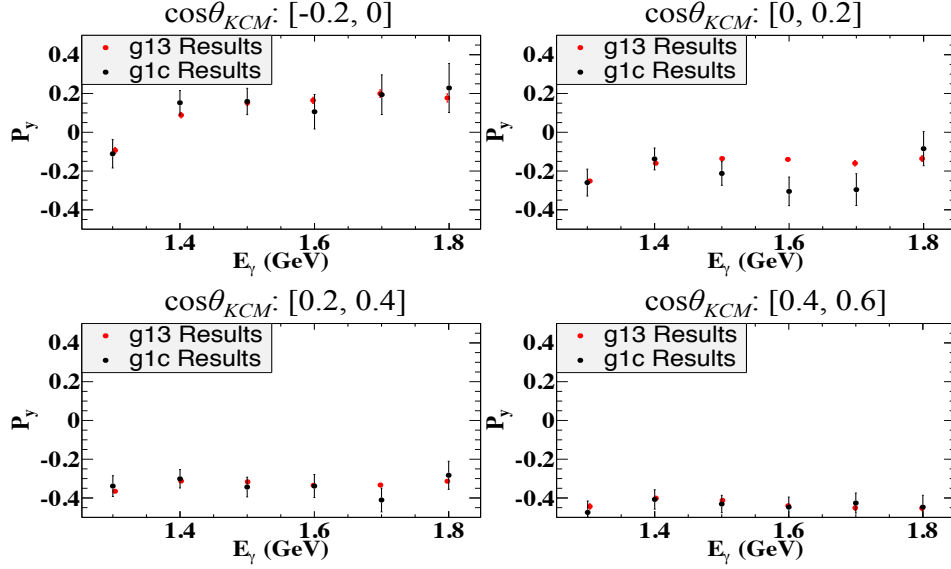


Figure 7.3: Comparison of P_y between the g1c and g13 experiments. The two sets of results are consistent with each other within their statistical uncertainties.

7.2 COMPARISON BETWEEN FSI AND QF OBSERVABLES

Figures 7.4, 7.5, and 7.6 show comparisons of C_x , C_z , and P_y over E_γ , θ'_Λ , p_K , θ_K , and $IM_{\Lambda n}$ between FSI and QF, respectively. The results suggest that:

- C_x varies around 0 for both FSI and QF.
- C_z for QF is close to 1, and is systematically larger than C_z for FSI for all kinematic variables.
- P_y for FSI is generally larger than QF except at large values of θ_K and large values of $IM_{\Lambda n}$.
- C_x , C_z , and P_y have a weaker dependence on E_γ than on other kinematic variables.
- The QF observables cover a much more limited θ'_Λ range than the FSI observables.

- The differences between the FSI and the QF observables are significant, which suggests that the FSI data sample is not dominant by QF events.

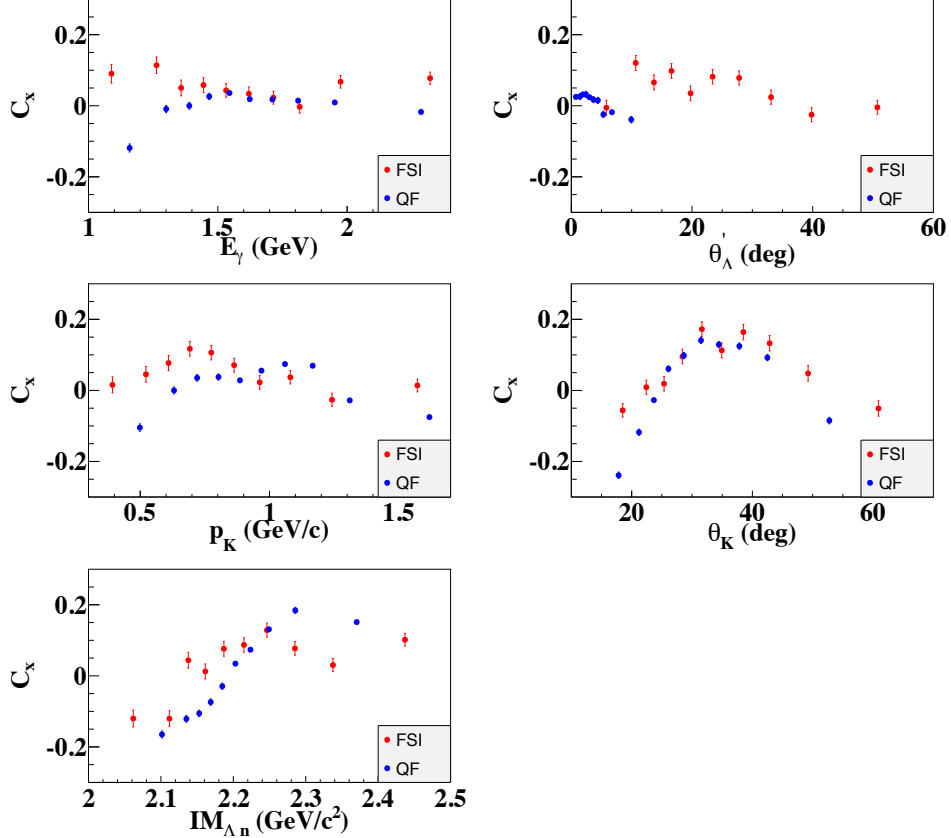


Figure 7.4: C_x comparison between FSI and QF for one-fold differential estimates. The top left figure is for E_γ , the top right figure is for θ'_Λ , the middle left figure is for p_K , the middle right figure is for θ_K , and the bottom figure is for $IM_{\Lambda n}$. The comparison shows significant differences between the QF and the FSI observable in some kinematic ranges.

7.3 DEPENDENCE OF QF OBSERVABLES ON MISSING MOMENTUM

During this study, we could not find a way to completely separate the quasi-free events from the final-state-interactions events. In section 4.3, the missing momentum cut was applied to obtain a sample dominated by QF events and a sample dominated by FSI events. The choice of the cut value of 0.2 GeV/ c is based on some considerations.

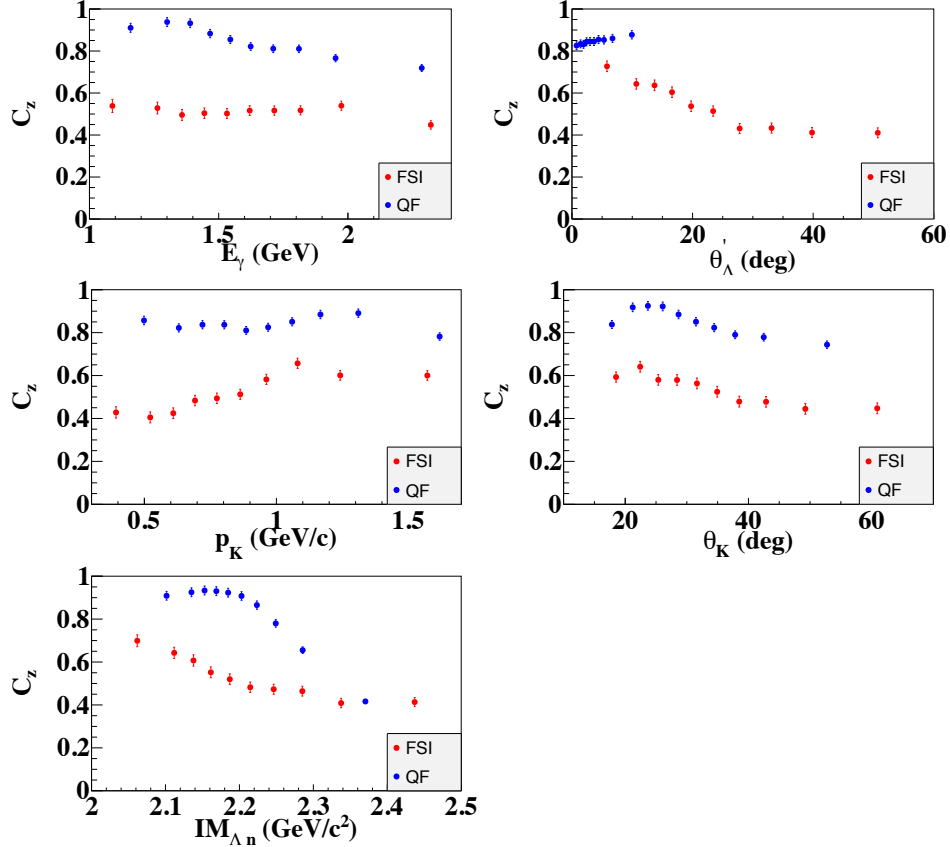


Figure 7.5: C_z comparison between FSI and QF for one-fold differential estimates. The top left figure is for E_γ , the top right figure is for θ'_Λ , the middle left figure is for p_K , the middle right figure is for θ_K , and the bottom figure is for IM_{Λ_n} . The QF observable is systematically larger than the FSI observable for all kinematic variables.

Firstly, both QF and FSI data should have enough statistics for further analysis. Secondly, the effect of one on the other needs to be reduced to a low level. To test the effect of FSI on the QF results, the QF data were divided into three data groups called D1, D2, and D3. Their corresponding missing momentum cut ranges are 0.1 – 0.2 GeV/c, 0.05 – 0.1 GeV/c, and 0 – 0.05 GeV/c. Figure 7.7 shows comparison of C_x , C_z , and P_y extracted from the different data groups. The QF data in D3 should be cleaner than the data in D1 and D2. The results for the D1 and D2 were subtracted from the values for D3. Figure 7.8 shows the differences. The figures show that the results for the different cut ranges are close, which suggests that the effect of FSI on

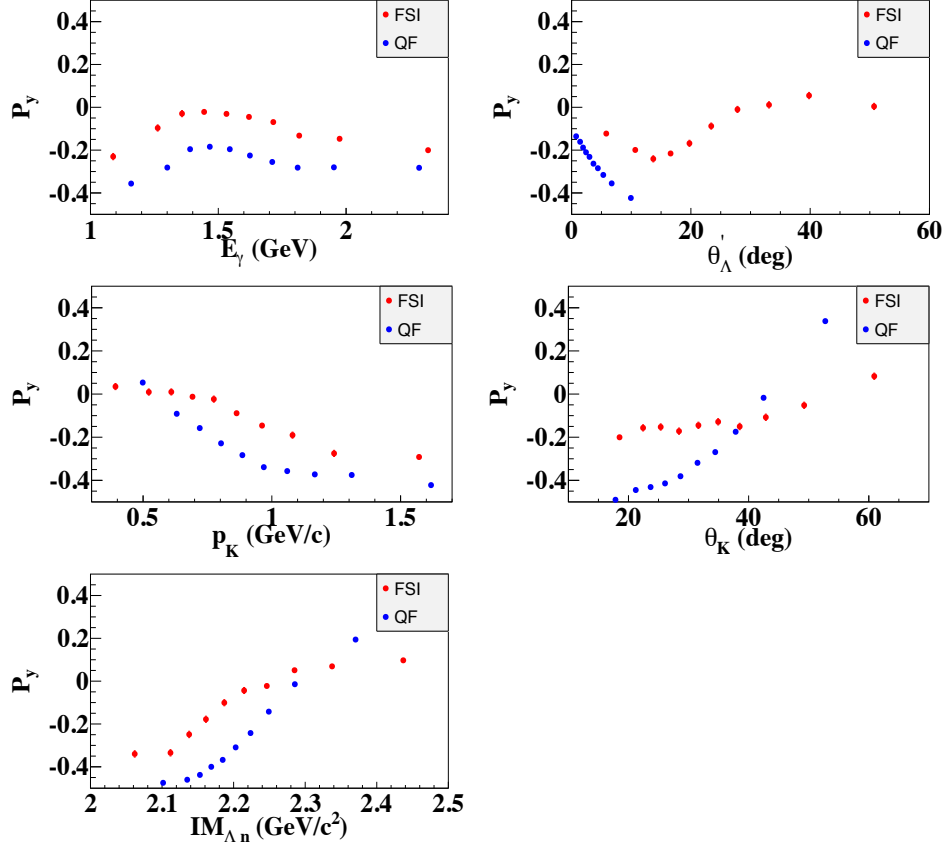


Figure 7.6: P_y comparison between FSI and QF for one-fold differential estimates. The top left figure is for E_γ , the top right figure is for θ'_Λ , the middle left figure is for p_K , the middle right figure is for θ_K , and the bottom figure is for $IM_{\Lambda n}$. The FSI observable is systematically larger than the QF observable for all kinematic variables, except at large values of θ_K and large values of $IM_{\Lambda n}$.

the QF results is small. The small differences are reported as systematic uncertainties in section 6.7.

7.4 COMPARISON OF FSI OBSERVABLES TO THEORETICAL CALCULATIONS

Figure 7.9 shows comparisons of C_x , C_z , and P_y between our four-fold differential estimates and the Miyagawa's model. Since the CLAS acceptance constrained the kinematics of our data, especially θ_K , the direct comparison cannot be done. The data and the model predictions are plotted in the same figure only to demonstrate

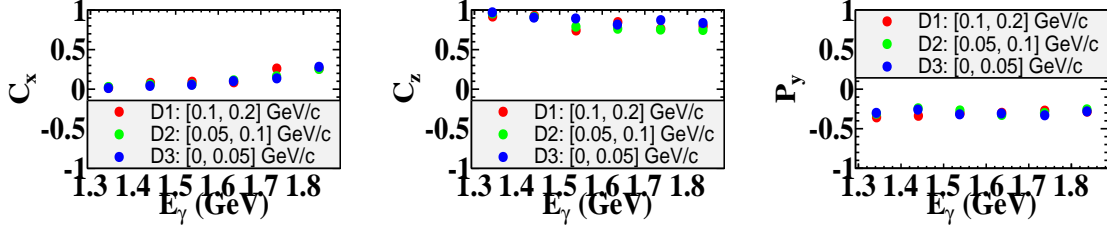


Figure 7.7: Comparison of C_x , C_z , and P_y for various missing momentum cut ranges at $0.15 \leq \cos \theta_{KCM} \leq 0.35$. The left figure is for C_x , the middle figure is for C_z , and the right figure is for P_y . The red points are for the cut range between 0.1 and 0.2 GeV/c, the green points are for the cut range between 0.05 and 0.1 GeV/c, and the blue points are for the cut range between 0 and 0.05 GeV/c.

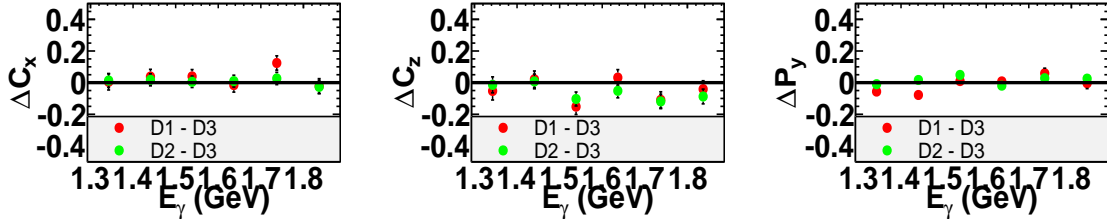


Figure 7.8: Difference of C_x , C_z , and P_y between different missing momentum cut ranges at $0.15 \leq \cos \theta_{KCM} \leq 0.35$. The left figure is for ΔC_x , the middle figure is for ΔC_z , and the right figure is for ΔP_y . The red points represent differences of results between 0.1 – 0.2 GeV/c and 0 – 0.05 GeV/c, and the green points represent differences of results between 0.05 – 0.1 GeV/c and 0 – 0.05 GeV/c. The black lines are drawn to show visually the y -value of zero.

the statistical uncertainties of the data and the predicted sensitivity to different YN potentials. In the figure, data error bars include only statistical uncertainties. Our results indicate that the expected statistical uncertainties of four-fold differential estimates are reasonable for the YN study, especially in view of the fact that the full set of observables will be simultaneously fitted.

7.5 PHYSICS STUDIES OF THE REACTION $\vec{\gamma}d \rightarrow K^+ \vec{\Lambda}n$

Some physics studies of the reaction $\vec{\gamma}d \rightarrow K^+ \vec{\Lambda}n$ were done by simulations. The QF results for C_x , C_z , and P_y from the g13 data were input into the polarized differ-

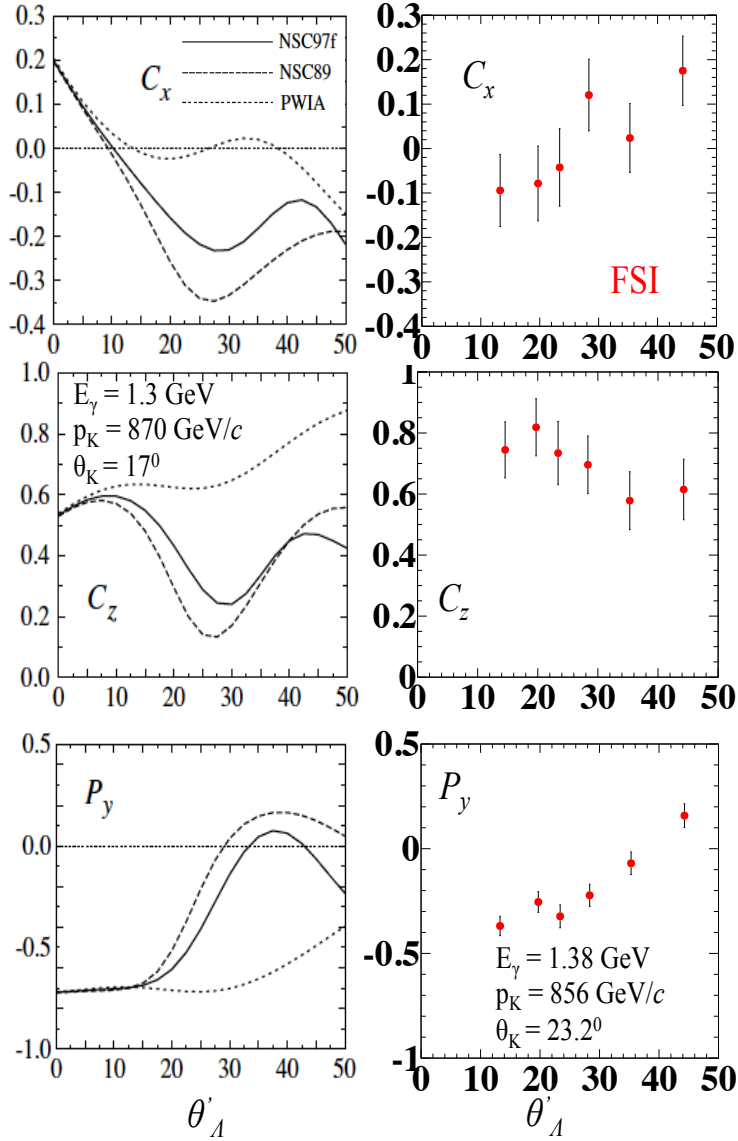


Figure 7.9: Comparison to the Miyagawa's model. Right column: C_x , C_z , and P_y as a function of θ'_Λ for FSI in the bin ($E_\gamma = 1.38$ GeV, $p_K = 856$ GeV/ c , and $\theta_K = 23.2^\circ$). Left column: Model predictions [6] for C_x , C_z , and P_y in a similar kinematic bin. Dotted curves are for QF only, while the solid and dashed-dotted curves are for QF and FSI with two different hyperon-nucleon potentials, respectively.

ential cross section of the QF mechanism in our generator (details are given in the section 4.4). Two channels were then generated, the QF mechanism (according to the polarized differential cross section) and the K^+n re-scattering (according to phase space distribution). The generator produced equal number of events for each of the two channels. This means that each kaon produced in the QF mechanism scattered then off the spectator neutron. Simulated data were obtained after the generated data passed through the detector simulation and were analyzed the same way as were the real data.

To study the mutual effects between QF and FSI, the simulated data were separated into two data samples by the MP cut at the same point of $0.2 \text{ GeV}/c$ as the experimental data. The QF sample (events with missing momentum lower than $0.2 \text{ GeV}/c$) was smeared with 3% of the Kn re-scattering events, while the Kn re-scattering sample (events with missing momentum above $0.2 \text{ GeV}/c$) was smeared with 12% of the QF events. Figure 7.10 shows comparison of C_x , C_z , and P_y extracted from the clean and the smeared (quasi-clean) samples. The observables on the left part of the figure were extracted from the clean and the smeared QF samples, and the observables on the right part of the figure were extracted from the clean and the smeared Kn re-scattering samples. The comparison between the two QF results show that 3% FSI events in the QF sample, do not lead to significant bias in the extracted observables, which is expected. The comparison between the two FSI results show that 12% QF events in the FSI sample could lead to a small bias in the extracted observables. This work indicates that even if the FSI events are significantly smeared by the QF events (up to 12%), the observables extracted from the experimental data are reliable, and the small bias can be absorbed into systematic uncertainties.

In the generator, the only difference between the QF and Kn re-scattering channels is that the former does not have Kn scattering. Thus, the 3-momenta of the final-state kaon and neutron were different for the two channels. In order to esti-

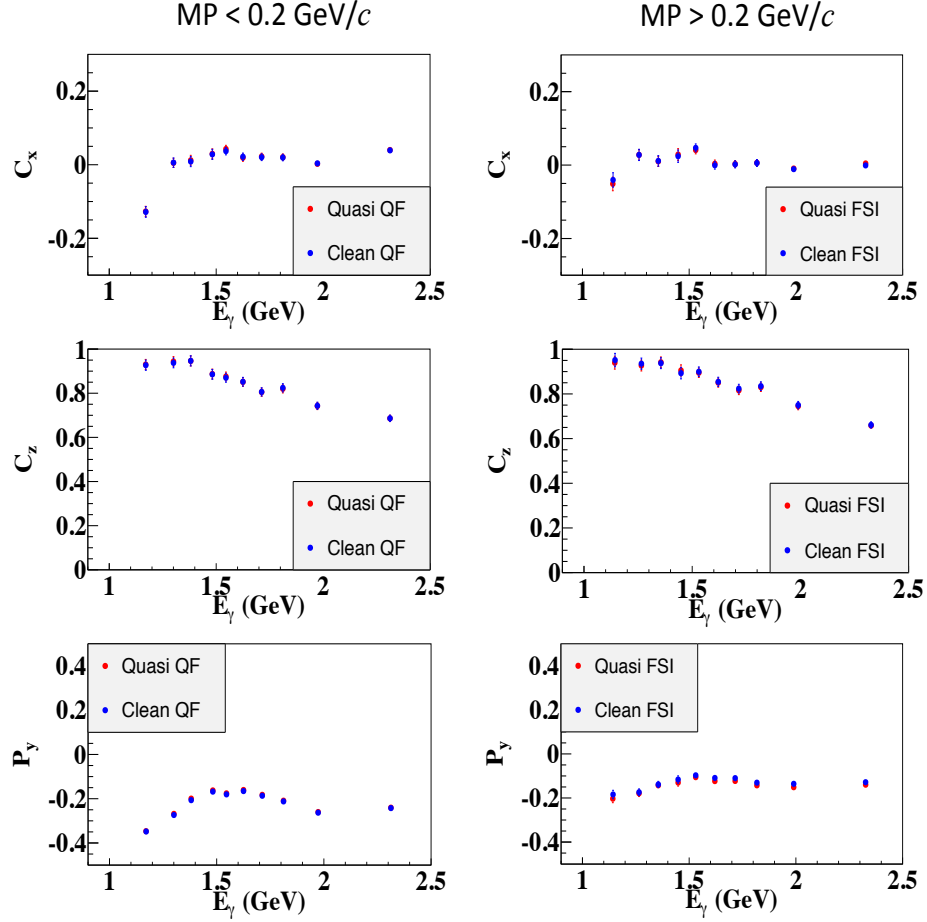


Figure 7.10: Comparison of C_x , C_z , and P_y between clean and quasi-clean channels. The left figure shows E_γ -dependent observables extracted from a data sample with MP lower than $0.2 \text{ GeV}/c$, and the right figure shows E_γ -dependent observables extracted from a data sample with MP higher than $0.2 \text{ GeV}/c$. The observables in the left part of the figure were extracted from the clean and smeared QF samples, and the observables in the right part of the figure were extracted from the clean and smeared Kn re-scattering samples. One could see a small difference between P_y from the clean and the quasi-clean FSI samples. The difference is due to the effect of 12% QF events in the FSI sample. In real data such a difference can be absorbed into a systematic uncertainty.

mate the effects of Kn scattering on the QF C_x , C_z , and P_y the observables were separately extracted from the QF and the Kn re-scattering events and compared. Figures 7.11, 7.12, and 7.13 show these comparisons. In this study, the axis convention and the bin setup were the same as in section 5.4. The results suggest that:

- The E_γ -dependent C_z is consistent between QF and FSI, because the Kn re-scattering does not change the kinematic variables E_γ and $\cos\theta_z$.
- Other kinematic-variable-dependent observables are significantly different, because p_K , θ_K , θ'_Λ , $IM_{\Lambda n}$, $\cos\theta_x$, and $\cos\theta_y$ are changed by the Kn re-scattering.
- The observable distributions for FSI become smoother, because the kinematic-variable-dependent observables for QF are redistributed after Kn scattering.

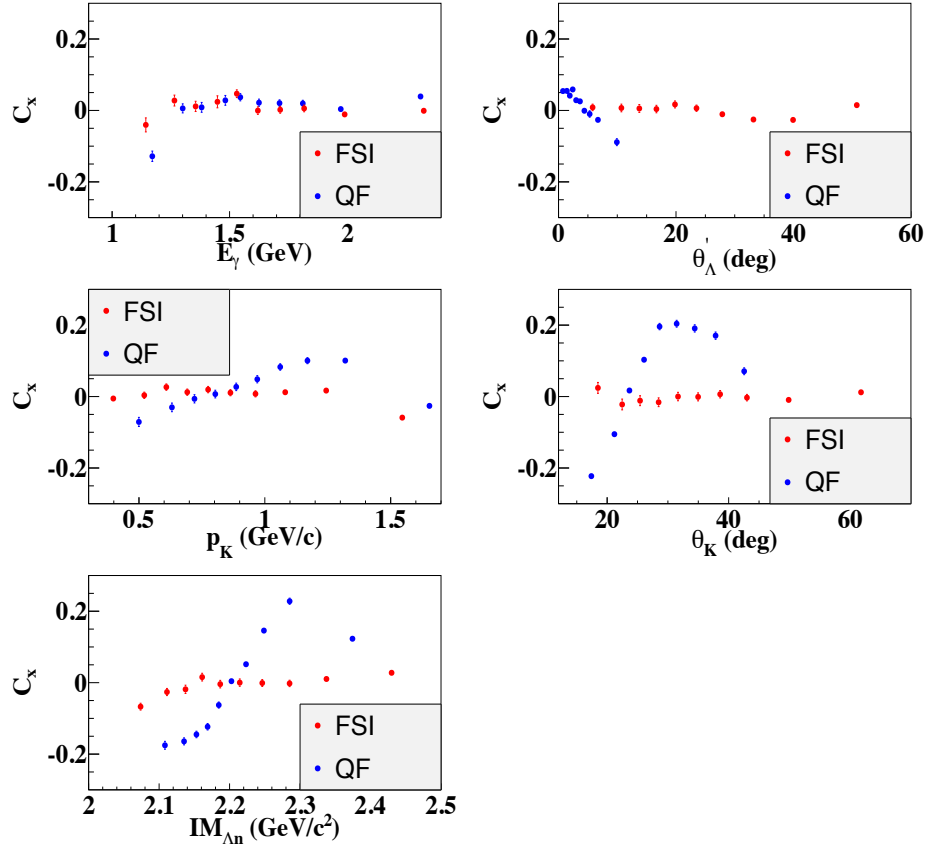


Figure 7.11: C_x comparison between FSI and QF for simulated data. The top left figure is for E_γ , the top right figure is for θ'_Λ , the middle left figure is for p_K , the middle right figure is for θ_K , and the bottom figure is for $IM_{\Lambda n}$. While Kn re-scattering changes very slightly the E_γ dependence of C_x , the other dependences are significantly affected by the Kn FSI.

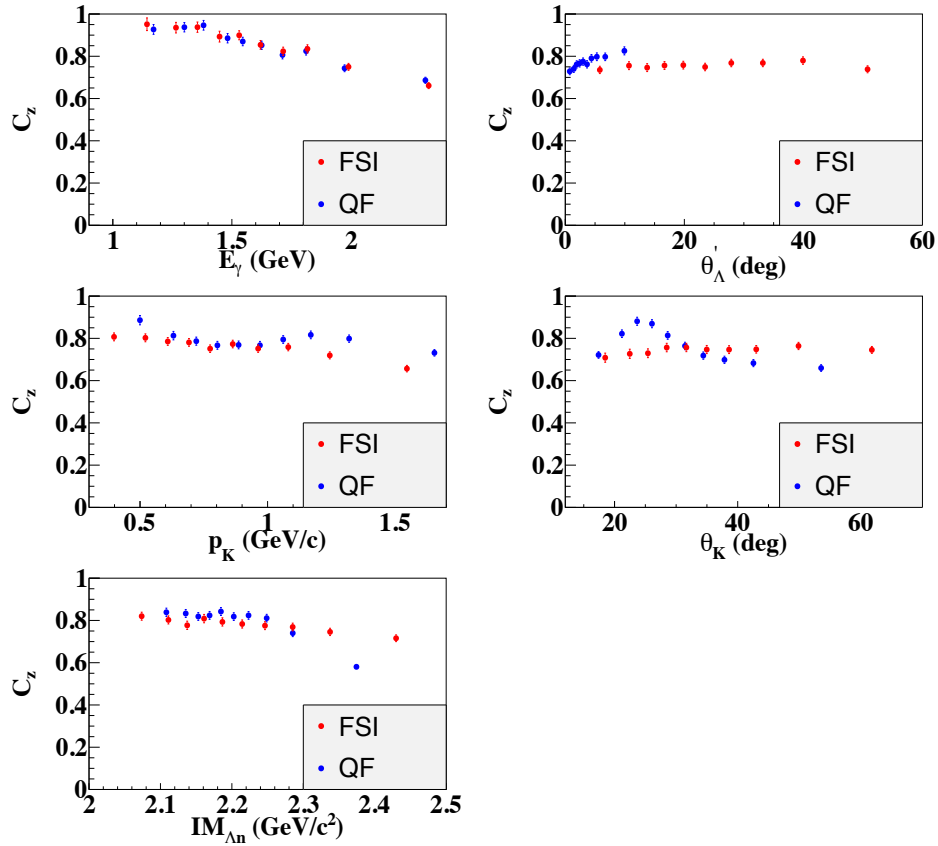


Figure 7.12: C_z comparison between FSI and QF for simulated data. The top left figure is for E_γ , the top right figure is for θ'_Λ , the middle left figure is for p_K , the middle right figure is for θ_K , and the bottom figure is for $IM_{\Lambda n}$. The E_γ dependence of C_z is not changed by the Kn re-scattering. The other kinematic dependences are affected by the Kn FSI.

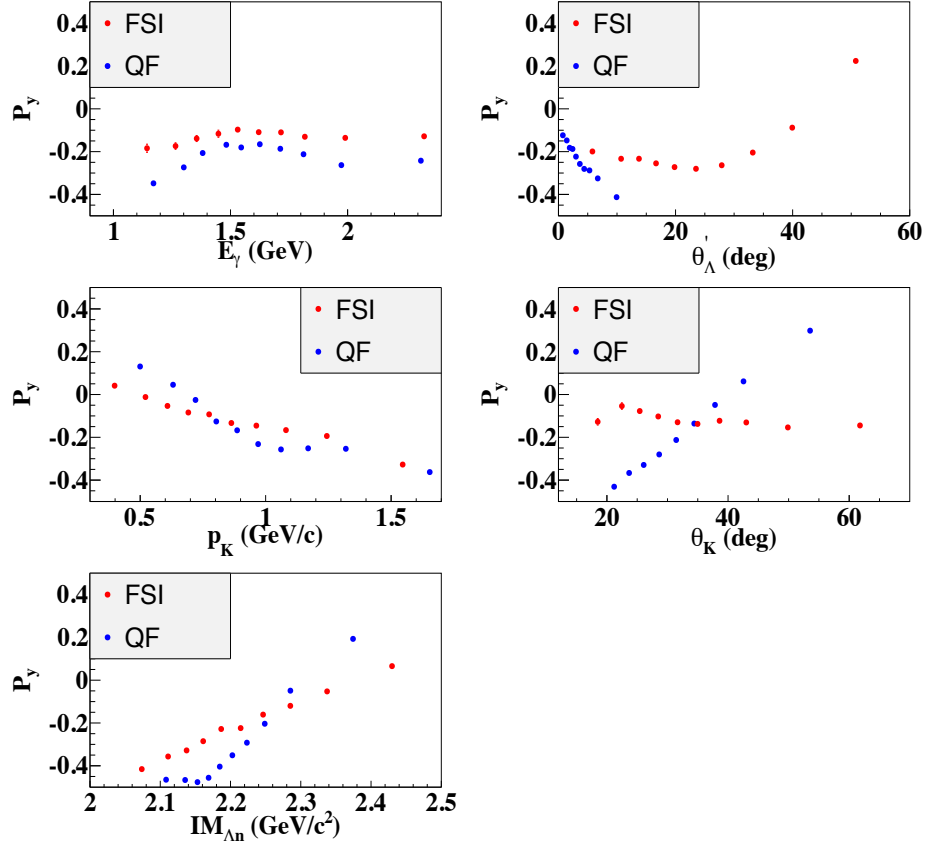


Figure 7.13: P_y comparison between FSI and QF for simulated data. The top left figure is for E_γ , the top right figure is for θ'_Λ , the middle left figure is for p_K , the middle right figure is for θ_K , and the bottom figure is for $IM_{\Lambda n}$. All kinematic dependences of the recoil polarization are strongly affected by the Kn FSI.

CHAPTER 8

SUMMARY

In this work we report experimental estimates of the polarization observables, C_x , C_z , and P_y , for both the quasi-free mechanism and the final-state interactions of the reaction $\vec{\gamma}d \rightarrow K^+ \vec{\Lambda}n$ in the energy region $E_\gamma = 0.9 - 2.5$ GeV. These results are obtained by analysing data collected during the CLAS g13 experiment in which a circularly-polarized tagged photon beam produced via the bremsstrahlung technique was incident on an unpolarized liquid-deuterium target. The FSI results have been the primary objective of this project, while the QF results are an extra outcome. Both sets of results are new (there are no previously published data) and carry interesting physics insights. This document contains details of the analysis procedure and the statistical methods applied to extract the observables and to estimate their uncertainties.

In Chapter 3, the helicity and polarization of the photon beam are extracted event by event. In Chapter 4, the reaction is reconstructed by applying particle identification, photon selection, and invariant-mass cuts. A missing-momentum cut is used to obtain two data samples, one dominated by QF events and another dominated by FSI events, respectively. A custom background subtraction method is applied to each kinematic bin to determine the probability of each event in that bin to be a signal event and to obtain event yields. In Chapter 5, three different observable-extraction methods, the 1-dimensional fit method, the 2-dimensional fit method, and the maximum likelihood method, are studied in detail. The conclusion of the study is that the CLAS acceptance cannot be cancelled out in the extraction of the observables

and causes significant biases in the results of the 1D method. The maximum likelihood method is the most robust to effects due to detector acceptance and the results reported here are obtained with this method. Various axis conventions and kinematic-variable binnings are used in the determination of observables, depending on the physics objective driving their extraction. To make full use of the data, a method is applied to let all kinematic bins have similar statistics, which causes different bins to have different widths. The QF observables are extracted in bins of E_γ and $\cos\theta_{KCM}$. One-fold differential FSI observables are extracted as functions of E_γ , θ'_Λ , p_K , θ_K , or $IM_{\Lambda n}$, and two-fold differential FSI estimates are extracted in bins of different combinations of the above kinematic variables. Four-fold differential estimates are also obtained for a very restricted kinematics. In Chapter 6, systematic uncertainties of the observables due to various sources are estimated and the total systematic uncertainty of each observable is reported.

The comparison of our QF observables to published results for kaon photoproduction off the free proton suggests that nuclear effects such as nucleon binding, off-shellness and Fermi motion do not seem to significantly influence the quasi-free polarization observables C_x , C_z , and P_y when the spectator nucleon has a small momentum. The observed C_x discrepancy can be explained qualitatively by our findings about the acceptance-related biases in the 1D observable-extraction method that was used in the published analyses. A more detailed study of the dependence of QF observables on the spectator-nucleon momentum, discussed in Chapter 7, paves the way to explore new methods of extracting free-nucleon observables from bound-nucleon data, which is extremely relevant for analyses of scattering data off neutrons bound in deuteron or other light nuclei. A comparison between our QF and FSI results shows that the effect of FSI on the observables is significant and that the FSI sample is not dominated by QF events. More detailed studies of the effect of FSI on the QF observables using comprehensive simulated data can help to explore model-independent

methods to identify kinematics where Λn FSI dominate over other FSI.

A comprehensive Monte Carlo generator, including the main mechanisms of the reaction $\vec{\gamma}d \rightarrow K^+ \vec{\Lambda} n$ and the largest background channels, was developed and used extensively in this work. Firstly, simulated missing-mass distributions of background channels were used to do background subtraction in the analysis of real data. Then, a simulated study explored inherent biases in three observable-extraction methods and was used to identify the best method to use in this work. Additionally, mutual effects between QF and Kn FSI on C_x , C_z , and P_y were investigated. The event generator is a significant product of this work and it will continue to be used extensively in further physics studies of C_x , C_z , and P_y .

Our estimates for FSI observables are the first to be obtained. They are expected to significantly contribute to the effort to understand the dynamics of Λn scattering in the low-energy region of QCD. The observables extracted from our data will be fitted to theoretical calculations to constrain the free parameters of YN potentials. Ultimately, the data should be included in the global fit of YN scattering data. Our results for C_x , C_z , and P_y as functions of $IM_{\Lambda n}$ below the Σn threshold offer an opportunity to extract a spin-averaged Λn scattering length.

BIBLIOGRAPHY

- [1] David Griffiths, *Introduction to Elementary Particles*, 2 ed., Wiley-VCH, 2008.
- [2] David J. Gross, *Asymptotic Freedom*, *Physics Today* **40** (1987), 39.
- [3] N. Zachariou, *Determination of the Azimuthal Asymmetry of Deuteron Photodisintegration in the Energy Region $E_\gamma = 1.1 - 2.3$ GeV*, Ph.D. thesis, The George Washington University, 2011.
- [4] A. Deur, V. Burkert, J.P. Chen, and W. Korsch, *Determination of the effective strong coupling constant $\alpha_{s,g_1}(Q^2)$* , *Physics Letters B* **665** (2008), 349.
- [5] M. Gell-Mann and Y. Ne'eman, *The Eightfold Way*, 1964, unpublished.
- [6] K. Miyagawa *et al.*, *Polarization observables in exclusive kaon photoproduction on the deuteron*, *Phys. Rev. C* **74** (2006), 034002.
- [7] J. Haidenbauer, *Meson exchange hyperon-nucleon interaction based on correlated $\pi\pi/K^-$ exchange*, *Eur. Phys. J. A* **33** (2007), 287.
- [8] R. Machleidt, K. Holinde, and C. Elster, *The Bonn meson-exchange model for the nucleon-nucleon interaction*, *Phys. Rep.* **149** (1987), 1.
- [9] R. Machleidt and I. Slaus, *The nucleon-nucleon interaction*, *J. Phys. G* **27** (2001), R69.
- [10] P. M. M. Maessen, Th. A. Rijken, and J. J. de Swart, *Soft-core baryon-baryon one-boson-exchange models. II. Hyperon-nucleon potential*, *Phys. Rev. C* **40** (1989), 2226.
- [11] Th. A. Rijken, V. G. J. Stoks, and Y. Yamamoto, *Soft-core hyperon-nucleon potentials*, *Phys. Rev. C* **59** (1999), 21.
- [12] Th. A. Rijken and Y. Yamamoto, *Extended-soft-core baryon-baryon model. II. Hyperon-nucleon interaction*, *Phys. Rev. C* **73** (2006), 044008.

- [13] H. Polinder, J. Haidenbauer, and Ulf-G. Meissner, *Hyperon-nucleon interactions - a chiral effective field theory approach*, Nucl. Phys. A **244** (2006), 779.
- [14] S. R. Beane *et al.*, *Hyperon-Nucleon Scattering from Fully-Dynamical Lattice QCD*, Nucl. Phys. A **794** (2007), 62.
- [15] T. Regge, *Introduction to complex angular momentum*, Il Nuovo Cimento Series 10 **14** (1959), 951.
- [16] S. Weinberg, *Nuclear forces from chiral lagrangians*, Phys. Lett. B **251** (1990), 288.
- [17] S. Weinberg, *Effective chiral lagrangians for nucleon-pion interactions and nuclear forces*, Nucl. Phys. B **363** (1991), 3.
- [18] E. Epelbaum *et al.*, *Modern Theory of Nuclear Forces*, Rev. Mod. Phys. **81** (2009), 1773.
- [19] L. Tang *et al.*, *The HKS experiment on Λ -hypernuclear spectroscopy via electro-production at JLab*, Rev. Mod. Phys. **790** (2007), 679c.
- [20] B. O. Kerbikov *et al.*, *Hyperon-nucleon interaction and the 2.13 GeV strange dibaryonic system in the P-matrix approach*, Nucl. Phys. A **480** (1988), 585.
- [21] R. A. Adelseck and L. E. Wright, *Lambda-neutron interaction in kaon photoproduction from the deuteron*, Phys. Rev. C **39** (1989), 580.
- [22] H. Yamamura *et al.*, *Inclusive K^+ and exclusive K^+Y photoproduction on the deuteron: L- and S-threshold phenomena*, Phys. Rev. C **61** ((1999)), 014001.
- [23] O. V. Maxwell, *Rescattering contributions to the photoproduction of kaons from the deuteron*, Phys. Rev. C **69** (2004), 034605.
- [24] A. Salam and H. Arenhövel, *Interaction effects in K^+ photoproduction on the deuteron*, Phys. Rev. C **70** (2004), 044008.
- [25] J. M. Laget, *Pentaquark, cusp, and rescattering in single kaon photoproduction off deuterium*, Phys. Rev. C **75** (2007), 014002.
- [26] A. Gasparyan, J. Haidenbauer, C. Hanhart, and K. Miyagawa, *ΛN scattering length from the reaction $\gamma d \rightarrow K^+ \Lambda n$* , Eur. Phys. J. A **32** (2007), 61.

- [27] A. Gasparyan *et al.*, *How to extract the ΛN scattering length from production reactions*, Phys. Rev. C **69** (2004), 034006.
- [28] P. N-Turonski *et al.*, *Kaon Production on the Deuteron Using Polarized Photons*, Jefferson Lab PAC30 Proposal: PR-06-103 (2006), https://www.jlab.org/exp_prog/proposals/06/PR-06-103.pdf.
- [29] R. K. Bradford, *Measurement of differential cross section and C_x and C_z for $\gamma p \rightarrow K^+\Lambda$ and $\gamma p \rightarrow K^+\Sigma$ using CLAS at Jefferson Lab*, Ph.D. thesis, Carnegie Mellon University, 2005.
- [30] R. K. Bradford *et al.*, *First measurement of beam-recoil observables C_x and C_z in hyperon photoproduction*, Phys. Rev. **75** (2007), 035205.
- [31] G. Knöchlein *et al.*, *Photo- and Electroproduction of Eta Mesons*, Z. Phys A **352** (1995), 327.
- [32] R. A. Adelseck and B. Saghai, *Kaon photoproduction: Data consistency, coupling constants, and polarization observables*, Phys. Rev. C **42** (1990), 108.
- [33] D. E. Groom *et al.*, *Review of particle physics. particle data group*, Eur. Phys. J. C **15** (2000), 1.
- [34] X. Li and L. E. Wright, *Final-state Lambda-neutron interaction in kaon photoproduction from the deuteron*, Nucl. Part. Phys. **17** (1991), 1127.
- [35] J. W. C. McNabb *et al.*, *Hyperon photoproduction in the nucleon resonance region*, Phys. Rev. C **69** (2004), 042201.
- [36] M. E. McCracken *et al.*, *Differential cross section and recoil polarization measurements for the $\gamma p \rightarrow K^+\Lambda$ reaction using CLAS at Jefferson lab*, Phys. Rev. C **81** (2010), 025201.
- [37] K. H. Glander *et al.*, *Measurement of $\gamma p \rightarrow K^+\Lambda$ and $\gamma p \rightarrow K^+\Sigma$ at photon energies up to 2.6 GeV*, Eur. Phys. J. A **19** (2004), 251.
- [38] A. Lleres *et al.*, *Polarization observable measurements for $\gamma p \rightarrow K^+\Lambda$ and $\gamma p \rightarrow K^+\Sigma$ for energies up to 1.5 GeV*, Eur. Phys. J. A **31** (2007), 79.
- [39] T. Corthals, J. Ryckebusch, and T. Van Cauteren, *Forward-angle $K^+\Lambda$ photoproduction in a regge-plus-resonance approach*, Phys. Rev. C **73** (2006), 045207.

- [40] S. Janssen, J. Ryckebusch, D. Debruyne, and T. Van Cauteren, *Kaon photoproduction: Background contributions, form factors, and missing resonances*, Phys. Rev. C **65** (2001), 015201.
- [41] T. Mart, C. Bennhold, H. Haberzettl, and L. Tiator, <http://www.kph.uni-mainz.de/MAID/kaon/kaonmaid.html> (2000).
- [42] A. V. Sarantsev and V. Nikonov, based on the published model [67, 68], “3pol-05” model.
- [43] Christoph W. Leemann *et al.*, *The continuous electron beam accelerator facility: CEBAF at the Jefferson Laboratory*, Ann. Rev. Nucl. Part. Sci. **51** (2001), 413.
- [44] D. I. Sober *et al.*, *The bremsstrahlung tagged photon beam in Hall B at JLab*, Nucl. Instr. Meth. A **440** (2000), 263.
- [45] B. Mecking *et al.*, *The CEBAF large acceptance spectrometer (CLAS)*, Nucl. Instr. Meth. A **503** (2003), 513.
- [46] P. Adderley *et al.*, https://www.jlab.org/accel/inj_group/docs/2002/ori.pdf (2002).
- [47] A. V. Glamazdin *et al.*, *Electron beam Moller polarimeter at JLab Hall A*, Fizika B **8** (1999), 91.
- [48] J. M. Grames, *Measurement of a weak polarization sensitivity to the beam orbit of the CEBAF accelerator*, Ph.D. thesis, University of Illinois at Urbana-Champaign, 2000.
- [49] M. D. Mestayer *et al.*, *The CLAS drift chamber system*, Nucl. Instr. Meth. A **449** (2000), 81.
- [50] E. Smith *et al.*, *The time-of-light system for CLAS*, Nucl. Instr. Meth. A **432** (1999), 265.
- [51] M. Amarian *et al.*, *The CLAS Forward Electromagnetic Calorimeter*, Nucl. Instr. Meth. A **460** (2001), 239.
- [52] Y. G. Sharabian *et al.*, *A new highly segmented start counter for the CLAS detector*, Nucl. Instr. Meth. A **556** (2006), 246.

- [53] S. Christo, <http://www.jlab.org/~christo/g11a%20target.html> (2004).
- [54] P. Nadel-Turonski *et al.*, *Photoproduction and rescattering of polarized hyperons in deuterium*, *Few Body Syst.* **43** (2008), 227.
- [55] Charles Taylor (private communication).
- [56] H. Olsen and L. C. Maximon, *Photon and electron polarization in high-energy bremsstrahlung and pair production with screening*, *Phys. Rev.* **114** (1959), 887.
- [57] E. Pasyuk, *Energy loss corrections for charged particles in CLAS*, CLAS Note 2007–016, Jefferson Laboratory.
- [58] Paul Mattione, *Kinematic Fitting of Detached Vertices*, Master’s thesis, Rice University, 2007.
- [59] M. Williams, D. Applegate, and C. Meyer, *Determining Momentum and Energy Corrections for $g1c$ Using Kinematic Fitting*, CLAS Note 2004–017, Jefferson Laboratory.
- [60] Paul Mattione, *$K^*(892)^0\Lambda$ and $K^+\Sigma^*(1385)^-$ Photoproduction on the Deuteron*, Ph.D. thesis, Carnegie Mellon University, 2011.
- [61] E. Wolin, *GSIM*, <https://www.jlab.org/Hall-B/document/gsim/userguide.html> (1996).
- [62] R. Brun, *Root*, <https://root.cern.ch> (2014).
- [63] L. Moneta, <https://root.cern.ch/root/html530/TFitterMinuit.html> (2005).
- [64] D. S. Carman *et al.*, *First measurement of transferred polarization in the exclusive $\vec{e}p \rightarrow e'K^+\vec{\Lambda}$ reaction*, *Phys. Rev. L* **90** (2003), 131804.
- [65] X. Artru *et al.*, *Positivity constraints on spin observables in exclusive pseudoscalar meson photoproduction*, *Phys. Rev. C* **75** (2007), 024002.
- [66] John W. C. McNabb, *Photoproduction of Λ and Σ^0 Hyperons off Protons in the nucleon resonance region using CLAS at Jefferson Lab*, Ph.D. thesis, Carnegie Mellon University, 2002.

- [67] A. V. Sarantsev *et al.*, *Decays of baryon resonances into ΛK^+ , ΣK^+ and $\Sigma^+ K^0$* , Eur. Phys. J. A **25** (2005), 441.
- [68] L. Corradi *et al.*, *Multinucleon transfer reactions studied with the heavy-ion magnetic spectrometer prisma*, Eur. Phys. J. A **25** (2005), 427.